Design of a 405/430 kHz, 100 kW Transformer with Medium Voltage Insulation Sheets

Sharifa Sharfeldden

Thesis submitted to the faculty of the Virginia Polytechnic Institute and State University
in partial fulfillment of the requirements for the degree of

Master of Science
In
Electrical Engineering

Christina DiMarino
Dushan Boroyevich
Igor Cvetkovic

June 16th, 2023
Blacksburg, VA

Keywords: High Frequency Transformer, Planar Windings, Medium Voltage Insulation, Electric Field Analysis, Electric Field Mitigation, Resonant Converter, Litz Wire

Copyright 2023, Sharifa Sharfeldden

Design of a 405/430 kHz, 100 kW Transformer with Medium Voltage Insulation Sheets

Sharifa Sharfeldden

ABSTRACT

To achieve higher power density, converters and components must be able to handle higher voltage and current ratings at higher percentages of efficiency while also maintaining low cost and a compact footprint. To meet such demands, medium-voltage resonant converters have been favored by researchers for their ability to operate at higher switching frequencies. High frequency (HF) operation enables soft switching which, when achieved, reduces switching losses via either zero voltage switching (ZVS) or zero current switching (ZCS) depending on the converter topology. In addition to lower switching losses, the converter operates with low harmonic waveforms which produce less EMI compared to their hard switching counterparts. Finally, these resonant converters can be more compact because higher switching frequencies imply decreased volume of passive components. The passive component which benefits the most from this increased switching frequency is the transformer. The objective of this work is to design a >400 kHz, 100 kW transformer which will provide galvanic isolation in a Solid-State Transformer (SST) based PEBBs while maintaining high efficiency, high power density, and reduced size. This work aims to present a simplified design process for high frequency transformers, highlighting the trade-offs between co-dependent resonant converter and transformer parameters and how to balance them during the design process. This work will also demonstrate a novel high frequency transformer insulation design to achieve a partial discharge inception voltage (PDIV) of >10 kV.

Design of a 405/430 kHz, 100 kW Transformer with Medium Voltage Insulation Sheets

Sharifa Sharfeldden

GENERAL AUDIENCE ABSTRACT

As the world's population expands and countries progress, the demand for electricity that is high-powered, highly efficient, and dependable has increased exponentially. Further, it is integral to the longevity of global life that this development occurs in a fashion that mitigates environmental consequences. The power and technology sectors have been challenged to address the state of global environmental affairs, specifically regarding climate change, carbon dioxide emissions, and resource depletion. To move away from carbon emitting, non-renewable energy sources and processes, renewable energy sources and electric power systems must be integrated into the power grid. However, the challenge lies in the fact that there is not an easy way to interface between these renewable sources and the existing power grid. Such challenges have undermined the widespread adoption of renewable energy systems that are needed to address environmental issues in a timely manner. Recent developments in power electronics have enabled the practical application of the solid-state transformer (SST). The SST aims to replace the current, widespread form of power transformation: the line frequency transformer (50/60 Hz). This transformer is bulky, expensive, and requires a significant amount of additional circuitry to interface with renewable energy sources and electric power systems. The SST overcomes these drawbacks through high frequency operation (>200 kHz) which enables higher power at a reduced size by capitalizing on the indirect proportionality between the two parameters. The realization of the SST and its implementation has the ability to greatly advance the electrification of the transportation

industry which is a top contributor to carbon emissions. This work aims to demonstrate a >400 kHz, 100 kW SST with a novel magnetic design and insulation structure suited for electric ship applications.

ACKNOWLEDGMENTS

Firstly, I would like to thank the faculty and project collaborators whose leadership and expertise were integral to the success of this work: Dr. Christina DiMarino, Dr. Dushan Boroyevich, Dr. Igor Cvetkovic, and Dr. Ravisekhar N. Raju.

I would like to thank my fellow students and colleagues on the iPEBB project, especially: Narayanan Rajagopal, for his help with electrical and thermal simulations as well as 3D modeling; Taha Moaz, Marie Lawson, and Vladimir Mitrovic for their help with the converter and transformer testing. I would also like to thank my fellow CPES students and colleagues whose graciously allocated time to assist with a project outside of the scope of their responsibilities, especially: Mark Cairnie, Yu Chen, and Zichen Zhang for their assistance with electric field simulations and partial discharge testing; Jack Knoll and Benjamin Lyon for their assistance with thermal simulations; Minh Ngo for his invaluable guidance and assistance in the transformer design and assembly process.

I would like to thank the friends who have supported me throughout the years. From BTHS, I would like to thank Hillary Li, Kristal Drakes, Bo Li, Lucy Xu. From UR, I would like to thank Erin Jin Mei O'Malley, Jingxuan Wang, Brooke Smith, Danny Hyungjoon Kim and Willian Leyman. From VT, I would like to thank Kelly Graff and Sriya Chakravarthy for their invaluable friendships and never-ending support.

I would also like to thank the faculty and advisors whose recommendations and mentorships were pivotal to my professional and academic journey: Dr. Elias Mandala, Dr. Daniel Costinett, Dr. Ming Lun Lee, Dr. Selcuk Kose, Suzanne Conner, Sofia Pavan Macias, and Debora Chan.

I am thankful to the Department of Defense (DoD)'s Science, Mathematics, and Research for Transformation (SMART) program which financially supported me throughout this degree and to the Office of Naval Research (ONR) for sponsoring this project. This work was supported by the Office of Naval Research (ONR) with the grant number N00014-16-1-2956, DCN# 543-720-23. DISTRIBUTION STATEMENT A. Approved for public release; distribution unlimited (20230718).

Finally, I would like to express my deepest gratitude to my mother, Jillian Awong, whose unwavering, immense support for me could never be put into words. Thank you for your dedication and sacrifices throughout the years.

Contents

Chapter 1: Introduction 1
Application Background and Motivation 1
Solid State Transformers 3
iPEBB Background and Motivation 4
Research Objectives 9
Thesis Overview 9
Chapter 2: Background 10
High Frequency Transformer State-of-the-Art 10
Overview of Previous Work 13
SST Converter Operation and Design Space Overview 17
Chapter 3: Magnetic Design and Analysis of a 405/430 kHz, 100 kW Transformer 20
Design Process Challenges 20
Magnetizing Inductance Overview 21
Magnetic Transformer Operation Overview 22
Magnetic Cores in Transformers 25
Laminated Iron Cores 26
Powdered Cores 27
Amorphous Cores 27
Nanocrystalline Cores 28
Ferrite Cores 28
HFT Material Selection 29
Core Dimensions Considerations and Analysis 32
Magnetic Simulation of Transformer 37
High Frequency Winding Considerations 39
Overview of Transformer Windings 40
Litz Wire Selection for HFTs 41
Transformer Winding Loss Calculation and Simulation 42
Chapter 4: Insulation Design, Simulation, and Experimental Verification 46
History of Transformer Insulation 46
State of the Art Transformer Insulation 47
Insulation Theory for MV/HV Applications 52
Initial Prototype Insulation Evaluation 57
Electric Field Study of Insulation Sheets 63

Creation of New Sheets and PD Testing 79
Chapter 5: Transformer Assembly Process 85
Core Assembly Process 85
Winding Assembly Process 86
Transformer Build 87
Chapter 6: Experimental Verification of Magnetic Design of Transformer 88
Thermal Evaluation for Testing 88
Magnetizing Inductance and Leakage Inductance Measurements 92
Core Loss Testing 93
Winding Loss Testing 97
Chapter 7: Conclusion 99
Design Summary 99
Future Work 99
References 101

Chapter 1: Introduction

Application Background and Motivation

As the global population continues to climb rapidly, there is a growing demand for increased magnitude of power transformation, transmission, and distribution technologies [1]. In parallel, there is a desire for these demands to be met without continuing to negatively impact critical environmental concerns like climate change and global warming. As we continue to work towards a low-carbon or zero-carbon future, great attention has been placed on the industries and technologies which have been historically reliant on non-renewable energy sources. Specifically, transportation generates a significant amount of carbon emissions and has consistently been identified as a top contributor to global warming (Figure 1)[2].

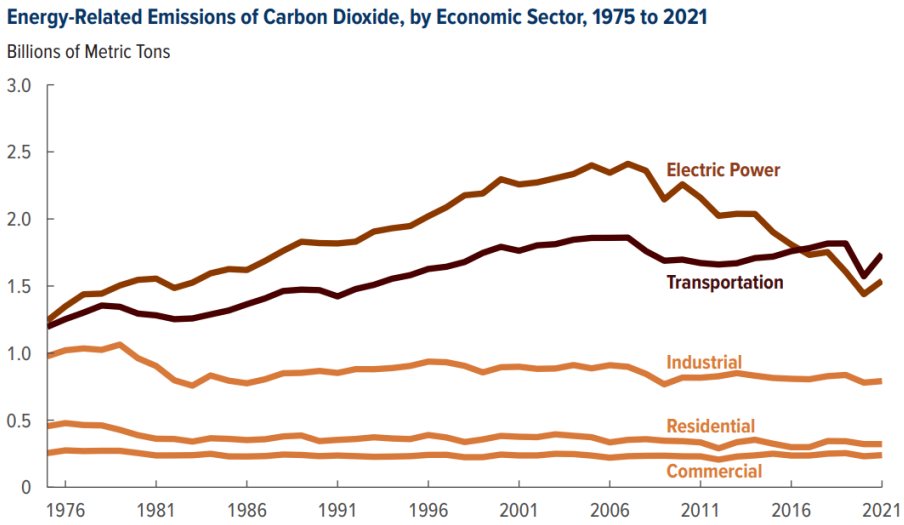


Figure 1: Carbon Dioxide Emissions due to Energy Sector from 1975 to 2021[2]**.**

One of the key initiatives towards reducing the footprint of the transportation sector is the electrification of transportation vehicles and power systems. Examples of such

initiatives include but are not limited to consumer and commercial electric vehicles, charging stations, electric trains, and electric ship power systems[3]. Power electronics converters and components have been identified as key technology which can enable the development and realization of these solutions[4].

Solid State Transformers

Historically, the component responsible for the transformation of electrical power has been the conventional or traditional transformer which typically operates at line frequency (50/60 Hz). These low frequency transformers are typically the largest part of any converter or power system due to their large iron cores and significant amount of copper windings. As power electronics trend towards higher frequency operation, the solid-state transformer (SST), first realized as the electronic transformer in 1968, may now be implemented [5]. SSTs are medium to high frequency transformers which provide voltage transformation and isolation at a comparatively smaller size and volume to line frequency transformers. The SST meets the functionality of the line frequency transformer despite its smaller size because the SST utilizes the increased switching frequency to maintain its power density rather than relying on increasing its core area or number of turns for the windings. As a result, the smaller SST can replace the bulky line frequency transformer and increase the power density and compactness of the overall power system. Additionally, depending on the application, the SST can also perform additional functionalities in the system. Aside from the HF transformer, the SST also comprises of two converters. At the input of the HF transformer, there is a converter which provides the HF ac input source. At the output of the high frequency transformer, there is a converter which transforms the output to a form that the rest of the system can use [5]. These converters are made up of widebandgap (WBG) semiconductor devices like silicon carbide (SiC) metal-oxide-semiconductor field-effect transistors (MOSFET). The development of these devices has given rise to higher frequency, medium and higher voltage applications because of their high temperature capabilities, high voltage, current and ability to handle higher switching frequencies. They are also able to achieve and exceed the previous

generation of devices at a smaller size, contributing further to the reduced footprint of these converters [6]. As a result of these advancements in power electronics, the SST is able to provide power factor correction, control, voltage and current regulation, fault isolation and supreme flexibility regarding different operational frequencies and voltages. These are qualities that the line frequency transformer would need significantly more circuitry to achieve. The SST is not without its shortcomings. Compared to the line frequency transformer, the SST can be significantly more expensive depending on the material and device requirements. The small core size of the SST coupling with higher operation points leaves the SST requiring advanced thermal and insulation systems. The high frequency transformer typically relies on heatsinks with forced or liquid cooling to maintain operation and encapsulation for its core or windings. Therefore, while the increased functionality of the SST can be expected, its size and weight benefits are not guaranteed [6]. This can only be achieved through careful designing of the high frequency transformer and surrounding converters. When realized, the SST finds usage in renewable energy applications, traction systems, electric vehicles and charging stations, and technologies where power control and quality are key [5]. In addition to providing the described functionalities, the SST also allows for bulky systems to be replaced, supporting compact and highly integrated systems.

iPEBB Background and Motivation

To achieve high power density and efficiency while maintaining low cost and size, researchers have leaned towards more modular and flexible converters and systems. One initiative to realize such systems in power electronics are power electronic building blocks (PEBBs). The PEBB was first introduced by the Office of Naval Research (ONR) in 1997 with the understanding that as naval ships lean towards electric power, special attention must be given to scalability and integration to realize higher power and efficiency [7]. Naval electric ships consist of several

different electric systems which would all require their own power supplies and circuitry. These electric ships would be difficult to realize if their size and cost fell outside of the capabilities of their application. To combat these concerns, PEBBs are designed to integrate essential power electronic components and devices into a designated block where they share power and cooling systems. The blocks are designed to be stacked in series or in parallel to achieve the overall system's power rating requirements. By utilizing medium voltage resonant converters with SSTs made of SiC MOSFETs and high frequency transformers, the power density and efficiency of the PEBBs can be maximized while minimizing their cost and footprint. The turning of the electric power system into a chain of blocks also gives way to ease of manufacturability, installation, and maintenance of electric ships. Because several PEBBs are meant to be used per power system, the mass production of the blocks will lead to lower overall manufacturing cost. The ease of installation and usage of the PEBBs reduces the need for significant construction and manipulation aboard the ships as well as reduce the need for specialized personnel to perform said tasks. The usage of flexible medium voltage converters and SSTs allow for PEBBs to support all forms of power conversion[8]. As the power and energy industry moves towards modularity and higher voltage, the PEBB concept also finds use in applications where scalable, compact power systems are needed like other transportation and power systems working towards electrification.

A recent realization of an SST based PEBB is presented in [9] where a 50-kVA SiC SST module is demonstrated at >98% efficiency (Figure 2).

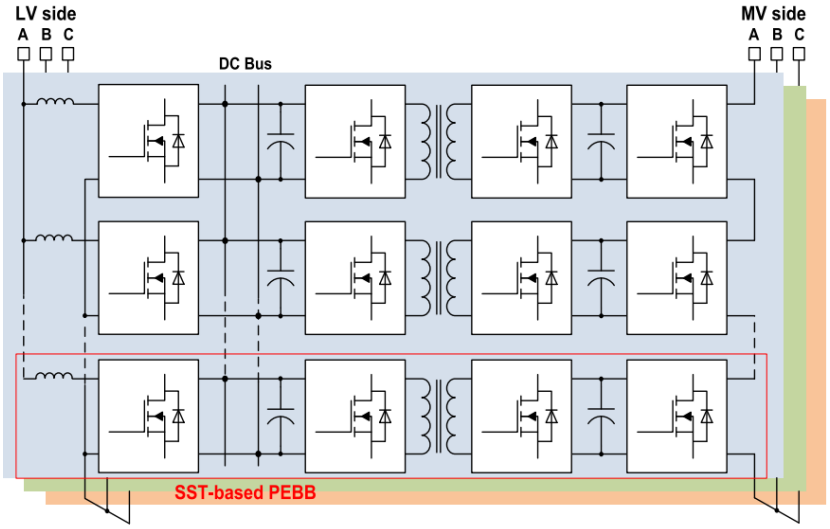


Figure 2: SST-based PEBB configuration for grid applications[9].

A comparison between two popular converter topologies, the CLLC and dual active bridge (DAB), is presented. The CLLC resonant converter is selected for its lower loss capabilities compared to the DAB which experiences losses during the turn off state of the converter as well as not guaranteeing ZVS at turn on, light load conditions. With a smaller transformer core, special attention was given to the insulation, thermal, and winding structure configuration to carefully balance these common SST design trade-offs. This balance is achieved through the design of an insulation system which provide both a high thermal conductivity, >0.8W-m/K, while achieving a breakdown strength of approximately 60 kV/mm. The successful development of the SST is further supported by comparison to a standard line frequency transformer which the proposed transformer meets and exceeds in terms of reduced footprint with high power density and efficiency. The symmetry of the high frequency transformer and resonant converter H-bridges also highlights increased manufacturability which is key to the adaptation of the PEBB and SSTs in general. While this thesis does not focus on power grid integration, organization, or control of

PEBBs, the significance of the development of SSTs and high frequency transformers lies in the realization of PEBBs into power systems.

This thesis supports the development of the integrated power electronic build block (iPEBB), a 250 kW, 500 kHz power block [10]. It features eight half-bridges, a high frequency transformer, DC-link, and resonant capacitors (Figure 3). The CLLC converter topology features 500 kHz, soft-switching inner bridges and hard switching outer bridges at the applicable line frequency. These bridges are created using 1.7 kV SiC MOSFET devices.

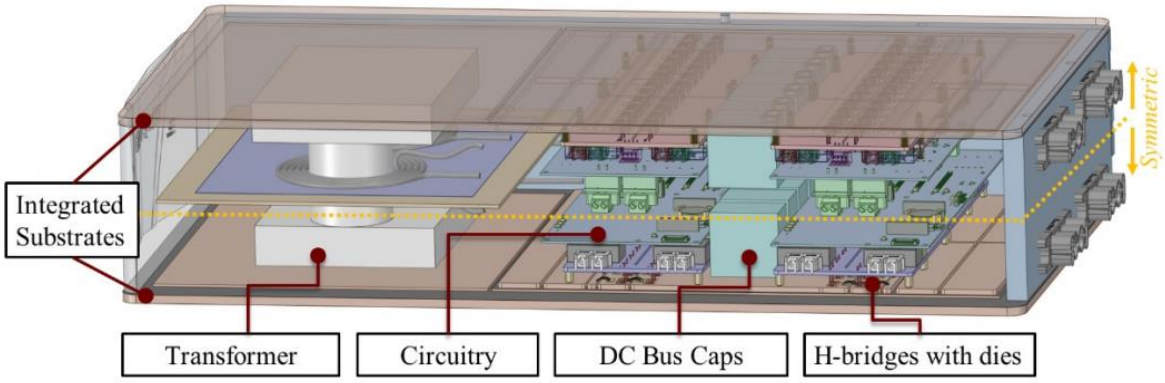


Figure 3: iPEBB overview with main components highlighted (2021 version with Fastwatt Transformer)[10].

The iPEBB was conceptualized after the PEBB 1000 which was a previously realized PEBB for naval ship applications. The PEBB 1000 achieved 100 kW at a switching frequency of 100 kHz using 1.7 kV SiC MOSFETs and a 1kV dc bus (Figure 4)[11].

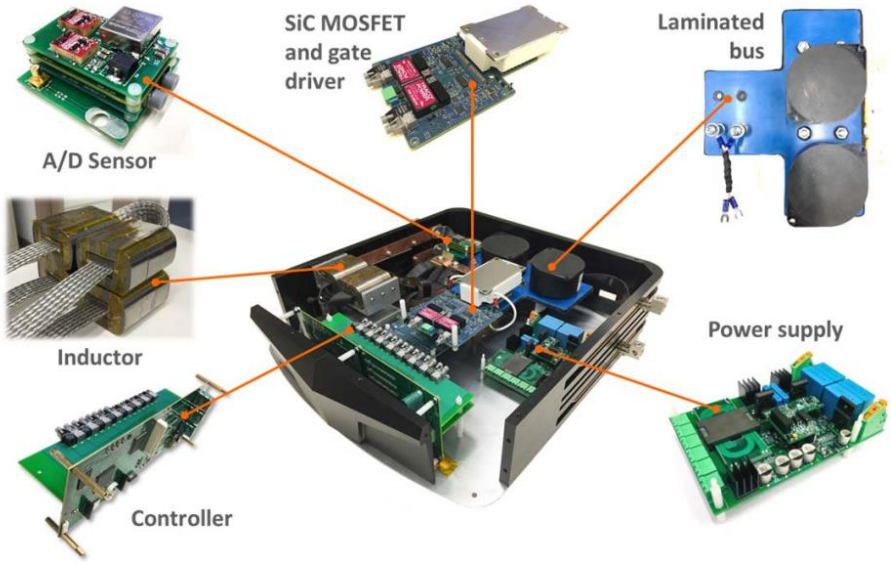


Figure 4: Power Electronic Building Block (PEBB) 1000[11].

While this PEBB was able to achieve a compact and scalable power system block with key power electronic devices and circuitry contained within a designated unit, upon further analysis and implementation, it left much to be desired regarding integration and manufacturability. The iPEBB aims to build upon the insight gained from the PEBB 1000 by addressing its shortcomings regarding complex manufacturability and scalability. The iPEBB intends to achieve this through use of a common substrate where all magnetic, switching, and control circuitry and components are directly mounted onto a common substrate. The iPEBB enclosure is designed to facilitate double-sided cooling via rack-cooling. To support integration efforts, the design of the individual components that make up the SST, H-bridges, auxiliary circuitry, control devices is supported by the use of Multiphysics, finite element analysis (FEA) tools to understand the electromagnetic and thermal trade-offs in the system. The common substrate is key to achieving automated manufacturing and simplified packaging of the iPEBB while reaching high power density and efficiency. It allows for easier integration of multiple essential components and shared cooling which keeps the overall weight of the power block under 16 kg (35 lbs.)[10]. The focus of this

work lies with the high frequency transformer tasked with providing galvanic isolation to the iPEBB.

Research Objectives

The objective of this work is to design a >400 kHz, high frequency transformer which will provide galvanic isolation in an SST-based PEBB, the iPEBB, while maintaining high efficiency, high power density, and reduced size which align with the current project needs. This work aims to present a simplified design process for high frequency transformers, highlighting the trade-offs between co-dependent resonant converter and transformer parameters and demonstrating how to balance them during the design process. This work will present developments and analysis for a novel high frequency transformer insulation design which can achieve a PDIV of >10 kV.

Thesis Overview

The thesis is organized into seven chapters which will discuss the theory, simulation, validation, and analysis required to demonstrate a >400 kHz, 100 kW transformer. Chapter two will go into further detail regarding the previously completed work for the project and describe the problem statements and challenges which motivated this thesis. It will present the design space for the SST and provide an overview of the state-of-the-art high frequency transformers and the transformer design process. Chapter three will discuss the magnetics design and analysis of the transformer including but not limited to the core and winding selection and simulation. Chapter four will detail the transformer insulation design and development as well as completed insulation testing. Chapter five will describe the transformer building process and test bay set-up. Chapter six will discuss the transformer performance verification via core and winding losses as well as approximate thermal

measurements of key components. Chapter seven will serve as the conclusion of this work where tasks accomplished, and future work will be described.

Chapter 2: Background

High Frequency Transformer State-of-the-Art

High frequency transformers (HFT) have been discussed in literature since the 1960s [5]. Emerging from a desire for a compact, high-power density yet functionally comparable replacement for the bulky line frequency transformer, HFTs have been the focus of transformer design for the past 20 years. Because line frequency transformers conventionally operate at a low frequency of 50/60 Hz, transformers which comparatively exceeded this frequency to reduce their size are labeled as HFTs in literature. Transformers within the range of 3 kHz to 200 kHz which deliver >10 kW have been vastly demonstrated in literature. [12] demonstrates a 20 kHz, 100 kW SST with peak insulation voltage of 20 kV while achieving an efficiency of >99%. A novel insulation design is achieved using 3D-printed bobbins and encapsulated windings to optimize heat spreading and air cooling (Figure 5).

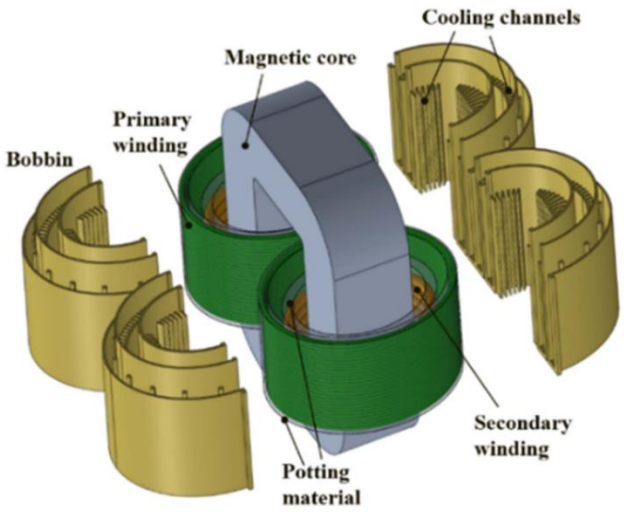


Figure 5: 100 kW, 20 kHz Transformer with 20 kV Isolation [12].

Based on the provided power density of 10.6 kW/L, the medium frequency transformer (MFT) itself is at least 9 L, not including the additional power electronics components and circuitry to complete the SST. [13] introduces a 200 kHz, 15 kW HFT for a CLLC-based SST, achieving a peak efficiency >98 % for data center and EV applications (Figure 6).

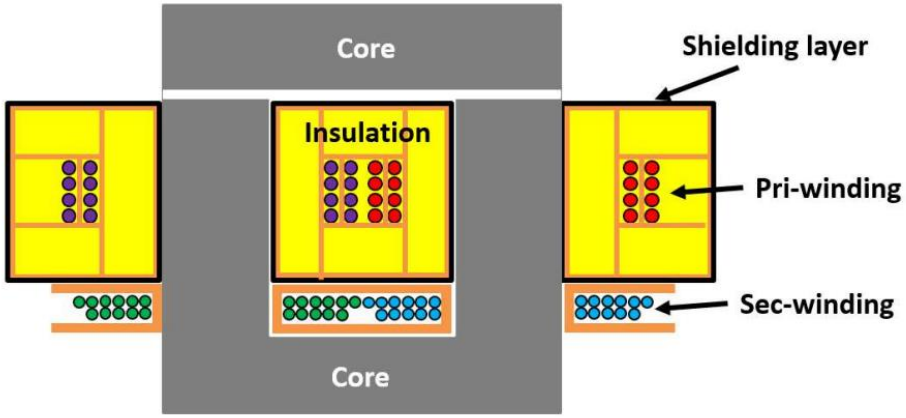


Figure 6: 15 kW, 200 kHz CLLC-based SST for data center and EV [13]**s.**

The transformer prototype is 190 mm by 170 mm with a transformer volume of 1.4 L. When compared to the previous MFT, through the increased frequency HFTs are able to achieve a higher efficiency at a smaller size and footprint. However, HFTs with a frequency >200 kHz has rarely

been demonstrated at >15 kW. HFT are now significantly limited by their thermal performance. Through comparison of these transformers, a common trade-off between MFT and HFT is size to power density is realized. Even though the 200-kW transformer is significantly smaller, its output power is smaller as well compared to the 20 kHz MFT which achieved 100 kW. A >200 kHz, HFT may be designed for higher power, but would lose its compact, light-weight characteristics to necessary cooling systems to support its operation. Further, as demonstrated in [13], it is also desirable to achieve higher voltage insulation at these higher powers. Transformer insulation systems, if not optimized, pose as a challenge for thermal performance.

Today, with the availability of magnetic materials like soft ferrite, it is possible to realize transformers exceeding 200 kHz, reaching as far as 1 MHz. Careful consideration must be given to insulation and thermal designs to maintain the small size and footprint of the HFT and overall SST. [14] demonstrates a 500 kHz, 15 kW transformer with a peak insulation of 30 kV and 98% efficiency (Figure 7).

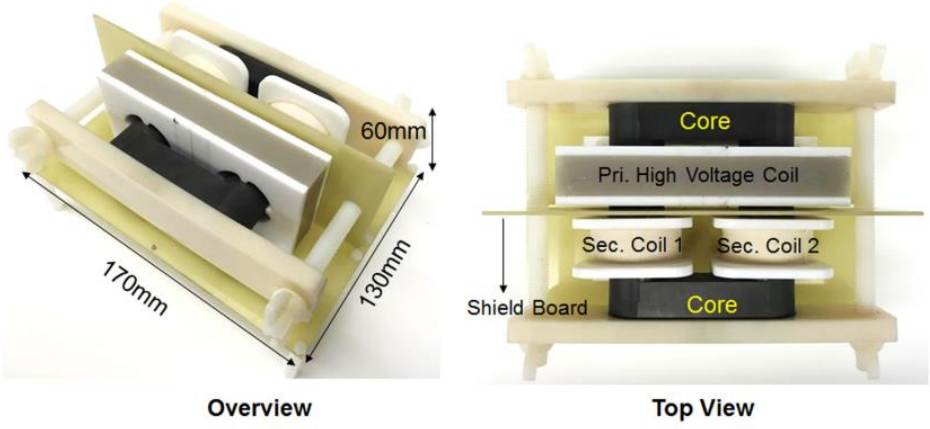


Figure 7: 15 kW, 500 kHz with 30 kV isolation [14].

The HV insulation is achieved by encapsulating the HV windings and controlling the electric field in the space between the bobbin and the grounded core using insulating tape, achieving an overall volume of approximately 0.37 L and power density of 2.9 kW/L. However, thermal performance

or measurements are not presented outside of selecting insulating materials with appropriate thermal conductivity. [15] demonstrates a 500 kHz, 18 kW transformer, the highest of published 500 kHz transformers to date, which achieved an efficiency of 99.6%. Analysis of the thermal performance of the core and windings was conducted using FEA simulations to identify restrictions in heat spreading between the windings and any hot spots which may exceed the thermal limit of the materials. A peak winding temperature of 126 C and peak core temperature of 96 C were achieved through implementation of winding and core potting as well as heat sink to improve heat spreading and air cooling (Figure 8).

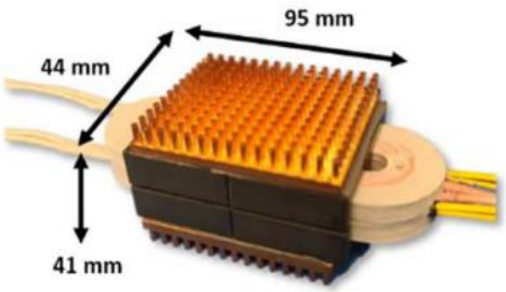


Figure 8: 18 kW, 500 kHz for DC Transformer (DCX) in EVs [15]**.**

Through implementation of these cooling solutions, the HFT in [15] was able to meet its applications size and footprint requirements while also achieving high power density for its frequency.

Overview of Previous Work

This work builds upon a 500 kHz, 250 kW transformer prototype intended for iPEBB nominal module operation at 1000 VAC/DC as well as previous HFT transformers addressing thermal concerns at higher power [8]. Created by Fastwatt, this transformer was designed to provide 15 kVAC / 20 kVDC galvanic isolation to the SST while achieving a high efficiency of >99% (Figure 9).

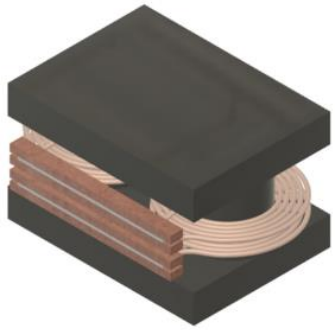


Figure 9: 250 kW, 500 kHz for CLLC-based SST.

Table I details the transformer parameter targets and final parameters. To meet the size and weight requirements of the application, special attention was given to transformer parameters which contribute to system footprint. The switching frequency of the transformer and core area are both directly related to power density. An increase in switching frequency may be implemented to offset the negative effect that decreasing core area would have on the power density. To maintain the reduction in size, the thermal and insulation system design must be carefully considered. A common challenge for the realization of SSTs for high power density, compact designs is voiding the small size benefit with bulky cooling systems or insulation layer thickness. This transformer planned to address these concerns with a novel, transformer insulation design which utilized minimal bulky insulation to provide both isolation and ease of cooling.

Table I: iPEBB Fastwatt Transformer Prototype Targets

iPEBB Fastwatt Transformer Prototype	
Switching Frequency	500 kHz
Power	250 kVA
Isolation Voltage	13.8 kVAC/20 kVDC
Efficiency	>99%
Turns Ratio	1:1
Dimensions (Volume, Weight)	<8 L and < 7 kg

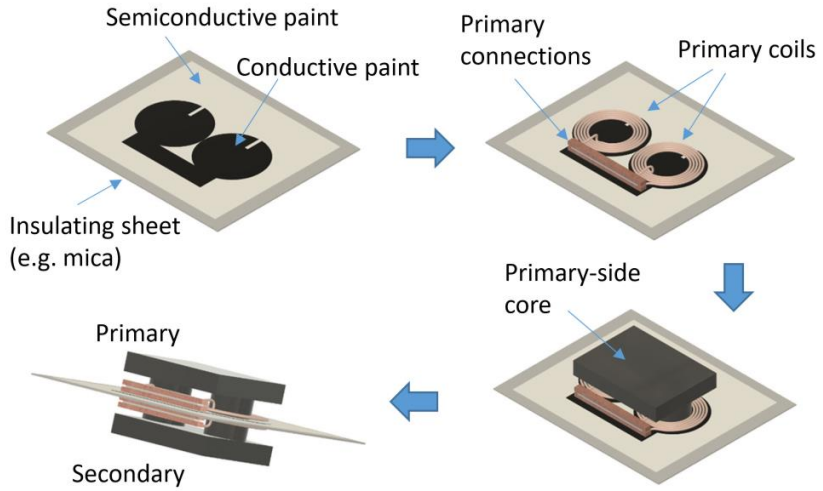


Figure 10: Fastwatt transformer build sequence with a focus on the primary side [8]**.**

Figure 10 shows a simplified insulation and transformer building sequence. This transformer features a split-core design meaning that the primary, high voltage and secondary, low voltage sides of the transformer are isolated via a 3 mm mica sheet [8]. This mica sheet is rated for an electric field strength of 25 kV/mm which makes it appropriate for a system which should provide 15 kVAC/ 20 kVDC isolation. Further, the mica material is mechanically strong enough to withstand the weight of the transformer core and windings. The build shown in Figure 10 shows the mica sheet in the middle of the transformer with symmetric layers of magnetics and insulation on each side. Detailing the primary side, first a conductive paint is placed in the shape of the coils to electrically tie the coils to the core. The conductive paint fills any airgaps which may exist

between the mica sheet, coils, and core [8]. Avoiding small air voids is important for HV applications because the electric breakdown of air is 3 MV/m and if exceeded, insulation degradation and system failure is very likely. A semiconductive paint is layered around the conductive paint and the coils are placed on top of the paints. The semiconductive paint used in the final prototype has nonlinear resistive properties due to its mix of epoxy and SiC filler, allowing for nonlinear resistive electric field grading. The transformer legs are placed in the space created by the coils and the core block is placed on top of the legs, completing the transformer build. The paints aid the mica insulation sheet in achieving high galvanic isolation by combating potential enhancements in the electric field across the transformer. Because the insulation design has been simplified down to a thin sheet and paints, the core and windings are left exposed aside from a standard, nylon litz wire high temperature insulation coating [8]. By avoiding heavy duty encapsulation or potting of the windings and/or core, the transformer can ideally be easily cooled using forced-air convection. Open circuit and short circuit tests were performed using a simplified SiC bridge to generate a comparable input ac voltage for the transformer to estimate core and copper losses as well as the transformer impedances. Table II details the experimental magnetic validation of the Fastwatt transformer prototype detailing the final measured losses and inductances.

Table II: iPEBB Fastwatt Transformer Experimental Validation Results

Transformer Parameter	Test Result
Magnetizing Inductance	11 uH
Leakage Inductance	900 nH
Core Loss	300 W
Winding Loss	850 W
HiPot Test (Insulation)	12 hours @ 12 kV_{rms}

SST Converter Operation and Design Space Overview

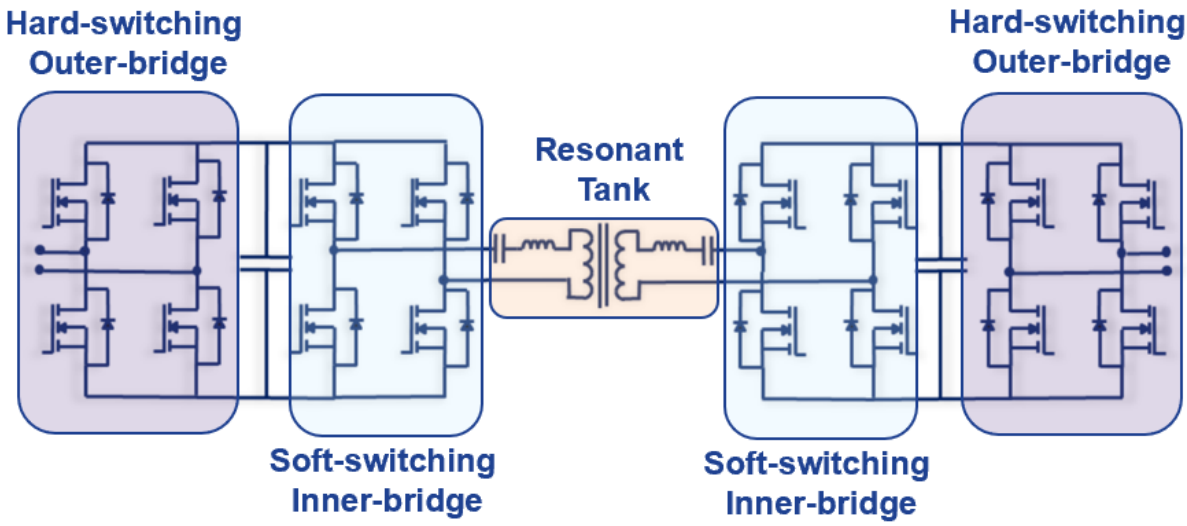


Figure 11: CLLC-based topology of the iPEBB Converter featuring four h-bridges, HFT, with inner soft-switching and outer hard-switching 1.7 kV SiC MOSFETs [10]**.**

The iPEBB features a CLLC resonant converter topology, shown in Figure 11.The CLLC topology is favored for compact, high-power systems like the PEBBs because its qualities improve power density, quality, and converter efficiency. Resonant converters like the CLLC utilize soft-switching techniques like Zero-Voltage Switching (ZVS) and Zero-Current Switching (ZCS) to reduce loss producing overlap between current and voltage waveforms. ZVS is achieved when the switch is turned on while the voltage is near zero, resulting in low turn-on losses and component stress. Similarly, ZCS is achieved when the current during turn off is near zero which reduces the turn-off losses and stress [16]. It is important to note that both of these techniques cannot be implemented together as their realizations counter each other i.e., ZVS requires the circulation of current which disqualifies ZCS operation. The reduction of switching losses in the converter improves overall converter efficiency and stress reduction improves the longevity of the components. Further, reduction in losses may be linked to reduced heat generation meaning that

soft switching can give way for reductions in thermal and insulation layers for power electronic devices [16]. The structure and resonant operation of the CLLC allow for the reduction of change in current over time (di/dt). This is because di/dt is directly proportional to the voltage across the inductor and indirectly proportional to the inductance itself. Inductors are put in series to achieve the CLLC topology which results in less current through the voltage sharing inductors or a smaller di/dt. Reductions in di/dt are desirable because they negatively contribute to electromagnetic interference (EMI) and harmonic distortion. The structure of the CLLC also acts as a low pass filter which reduces the presence of high frequency harmonics which contribute to EMI. By reducing EMI and distortion in the voltage and current waveforms, power quality and control of the converter is improved[16]. Lastly, the symmetric structure of the CLLC is beneficial for the manufacturability and simplicity of the PEBBs [10].

Upon the delivery of the Fastwatt transformer, the CLLC resonant converter operation was simulated using MATLAB PLECS to create a detailed design space for the SST. To do this, it was necessary to understand how all parts of the CLLC resonant converter and the HFT, which make up the SST-based PEBB, impact each other. From the perspective of the HFT, the purpose of the CLLC resonant converter is to provide a high frequency, ac input voltage to the transformer. From the perspective of the resonant converter, the purpose of the HFT is to provide galvanic isolation between the inner converter bridges and a magnetizing current which discharges the resonant capacitors during operation. The purpose of using a resonant converter like the CLLC is to achieve ZVS through soft switching the inner bridges of the SST [16]. Therefore, the creation of the design space for the transformer is centered around the parameters that are most critical for achieving ZVS. [17] identifies the resonance frequency (f_r), switching frequency (f_s), magnetizing inductance (Lm), transformer winding leakage inductance (Lr or Lk), and resonant capacitance (Cr) as key

design space parameters. [18] presents several equations which describe the relationship between these parameters in CLLC resonant converters. The resonant capacitor values are indirectly proportional to the transformer winding leakage inductances and the resonant frequency as shown in Equation (1)[19]. The magnetizing current is directly proportional to the voltage across the windings, and more importantly, inversely proportional to the magnetizing inductance and switching frequency of the transformer as shown in Equation (2) [18]. The magnetizing inductance is directly proportional to the deadtime, and indirectly proportional to the switching frequency and device output capacitances as shown in Equation (3)[18].

$$C_r = \frac{1}{4\pi^2 L_r f_r^2} \tag{1}$$

$$I_m = \frac{V_{windings}}{4 L_m f_s} \tag{2}$$

$$L_m = \frac{t_d}{8 f_s * \left(C_{oss,primary} + C_{oss,secondary}\right)} \tag{3}$$

Ideally, the resonant frequency will be set from the beginning of the SST design process and would not be considered for variation. From an efficiency perspective, setting the switching frequency equal to the resonant frequency would be ideal, however this is difficult to realize during operation because of resonant component tolerances, parasitics and concerns regarding stability and control [20]. To maximize efficiency, the switching frequency should be set just below the resonant frequency and all later components should be selected and designed around these frequencies. Initial converter simulation with the Fastwatt transformer found that ZVS was only achievable at light load without adjustment when parasitics were not introduced to the simulation circuit. With

the inclusion of parasitics, the switching frequency would need to be lowered and the deadtime would need to be adjusted to achieve ZVS. The more critical result was that ZVS could not be achieved at full load, especially with the inclusion of component parasitics. The understand what adjustments would need to be made to achieve ZVS, Equation 3 was used to calculate a range of deadtimes by varying the magnetic inductance of the transformer. It was found that the magnetic inductance would have to be less than half of its measured value, ~10 uH, to achieve ZVS under ideal conditions i.e., without parasitics. These simulations were completed without consideration of the impact that decreasing switching frequency and decreasing magnetizing inductance can have on the HFT, which when realized, clearly indicated that a new transformer prototype would need to be developed to better fit the iPEBB's SST.

Chapter 3: Magnetic Design and Analysis of a 405/430 kHz, 100 kW Transformer

Design Process Challenges

In addition to presenting a HFT with higher power density for the iPEBB's SST, this work also aims to present a novel, compact, and medium voltage insulation design. Therefore, the Fastwatt transformers application-driven features were maintained in the re-design such as its ungrounded, split-core and parallel, planar windings separated by a medium voltage insulation sheet (development detailed in Chapter 4) [10]. Typically, during HFT design for SSTs, the parameters which are most important to converter operation are already identified and estimated so the transformer parameters may be designed around those values from the beginning. Fundamental transformer equations and FEA simulation results can only provide ideal estimates during the

transformer design process. Despite targeting a specific magnetizing inductance, upon the building of the actual transformer, it is likely that this value shifts. This shifting is due to the assumptions that these equations and FEA tools make in their calculations like uniform magnetic fields in windings, uniform flux distributions, and many more. Further, during the actual transformer building process, it is unlikely that the winding lengths, thicknesses, and other dimensions will be realized exactly as modeled. Seasoned transformer designers expect this and tune their magnetizing inductances by adding or adjusting an air gap, literal or artificial, to their transformers to achieve and maintain ZVS in the SST. This transformer, however, has already been designed to have a 3 mm gap via the insulating mica sheet which limits its ability to be tuned after assembly. This is due to both electrical isolation requirements as well as overall iPEBB height restrictions. As a result, magnetizing inductance was at the forefront of the transformer design process.

Magnetizing Inductance Overview

At the time of the design of this transformer, key converter parameters like deadtime and device output capacitance (C_{oss}) were still being analyzed. The typical HFT design process had to be adjusted to assist that on-going effort. After identifying magnetizing inductance as the key transformer parameter affecting the ZVS operation of the resonant converter, the next step was to understand how magnetizing inductance is determine for HFTs and what it's affect is on the transformer operation. The magnetizing inductance of a transformer is not a physical, distinguishable inductor. It refers to the ability of the primary side winding to induce a magnetic flux in the core, link to the secondary winding, and induce a voltage on the secondary side. The magnetizing inductance of an air gapped transformer, a transformer with physically separated primary and secondary windings for electrical isolation, is directly proportional to the permeability

of free space (μ_0), number of turns (N), and area of core (A) as well as indirectly proportional to the length of the core gap (l_g) as shown in Equation (4)[19].

$$L_m = \frac{\mu_0 N^2 A}{l_g} \tag{4}$$

Equation (4) assumes that the reluctance of the core is significantly smaller than the reluctance of the air gapped region so the sum of the reluctances in a magnetic circuit representation of the transformer would be dominated by the reluctance of the gap. As previously described, the 3 mm gap is fixed so only the number of turns and the area of the core are available for variation to control the magnetizing inductance of the transformer.

Magnetic Transformer Operation Overview

The number of turns and core area are not only significant to the magnetizing inductance of the transformer but greatly impact the magnetic operation of the transformer. Magnetic flux density (B) is a key parameter in transformer design and operation analysis. To begin with, magnetic flux (φ) is an indication of the amount of magnetic field lines through a surface. Magnetic flux is related to magnetic flux density through Faraday's law of induction and Ampere's law [19]. Faraday's law describes that when a closed loop wire experiences a changing magnetic field, a voltage is induced in said wire. This induced voltage is directly proportional to the rate at which the magnetic flux passing through the loop changes. In circuits or devices with coiled wires like transformers and inductors, this voltage is also amplified by the number of turns in the wire due to the magnetic flux linkage that occurs between each turn. Ampere's law describes the proportionality between the magnetic field around a closed loop and the total current through said loop [19]. If a surface is

considered a closed loop, then Faraday's law may be related to Ampere's law through the flux-circulation theorem. Magnetic flux can then be described as the product of the magnetic flux density across the area of the surface, assuming uniformity. Therefore, magnetic flux density can be used to describe the strength and direction of the magnetic field at a point of interest. In transformers, this point or surface of interest is the area of the core as this is where the magnetic flux is contained. The magnetic core facilitates a magnetic path for the flux to traverse so that when an ac source is applied to the primary windings, coiled around one side of the core, a voltage may be induced in the secondary windings, separately coiled around the core. Overall, the magnetic flux density of a transformer directly impacts the magnetic capabilities of the transformer core and therefore dictates transformer operation. This application of Faraday's law is typically described as the transformer equation, shown in Equation (5) where the number of turns in the primary winding induces a voltage in the secondary winding due to the changing flux in the primary winding [19].

$$V_s = -N_p * \frac{\Delta\varphi}{\Delta t} \tag{5}$$

Depending on the waveform of the ac input voltage, Equation (5) may be detailed further to describe transformer operation. Considering an ac sinusoidal waveform which would result in a sinusoidal magnetic flux waveform, Equation (6) may be presented.

$$V_s = -N_p * \frac{\Delta(\varphi_m * \sin(\omega t))}{\Delta t} \tag{6}$$

We are most interested in calculating the peak or maximum flux density because this will indicate the worst-case operation of the transformer. This is because magnetic flux is directly proportional to transformer core losses and operational temperature. After computing the derivative for the maximum of a sinusoidal, simplifying angular frequency, and simplifying magnetic flux by assuming uniformity, Equation (7) is presented in a generalized form[21].

$$V_{peak} = N * B_{max} * 2\pi f * A_{core} \tag{7}$$

The rms voltage is then computed and simplified for the purpose of making meaningful comparisons to dc voltage operation, shown in Equation (8)[21].

$$V_{rms} = 4.44 * N * B_{max} * f * A_{core} \tag{8}$$

The constant in Equation (8) is typically referred to as the waveform factor and may be altered depending on the type of waveform of the ac input source. For the analysis of this transformer, a square waveform factor was used to present a worst-case scenario for flux density to account for the resonant converters inability to provide a perfect sinusoidal input ac source for the transformer. When Equation (8) is rearranged to solve for flux density, it is understood that all factors besides input voltage are indirectly proportional to flux density. Since a square waveform factor is smaller than the sinusoidal waveform factor, it presents a worst-care scenario as shown in Equation (9)[21].

$$B_{max} = \frac{V_{rms}}{4 * N * A_{core} * f} \tag{9}$$

The number of turns and the area of the core are indirectly proportional to the magnetic flux density of the transformer whereas the same two parameters are directly proportional to the magnetizing inductance. The number of turns and area of the core must therefore carefully be considered as they are key to balancing transformer operation versus resonant converter operation. Because the term is squared, the number of turns has significantly more impact on the magnetizing inductance than the area of the core. Therefore, attention was first put onto the transformer core area. However, before the transformer core area can be determined, a core material which is appropriate for the transformer operation should be identified. The target resonant frequency for the iPEBB's SST is 500 kHz and as previously described, the switching frequency target is at least just below the resonant frequency for maximum efficiency thought not set at the time of core material selection.

Magnetic Cores in Transformers

Before a core material is selected, it is important to understand the basic principles of what defines magnetic materials and how they are classified so the right core material may be chosen based on the application. There are two types of magnetic materials: hard magnetics and soft magnetics [19]. Hard magnetic materials or permanent magnetics resist demagnetization meaning that even if they were connected to an ac source, the output would be a constant magnetic field. Further, because of their low permeability value, they are not able to support a magnetic flux. This makes sense considering permeability is an amplifying parameter and how magnetic flux density is related to the magnetic field strength. These qualities make them undesirable for transformer design. Soft magnetics, however, can be magnetized and demagnetized by an ac source, as well as have a higher permeability enough to support magnetic flux. Being able to support flux is key for transformer core material selection considering the primary role of the magnetic transformer core

as opposed to an air/non-magnetic core is to provide a reliable magnetic path for the flow of flux and a place where the magnetic field can concentrate so that flux linkage between the windings can prosper. Some of the most prominent soft magnetic materials for transformer cores are laminated iron alloys, power iron, amorphous alloys, nanocrystalline, and ferrite[19][21].

Laminated Iron Cores

Generally, iron cores exhibit high permeability and high conductivity compared to other core magnetic materials. This contributes to their lower hysteresis loss, a type of core loss, as their magnetic state is easy to change. However, their high conductivity can lead to increased eddy currents resulting in losses if not treated. For this reason, iron cores are typically laminated which is a process where the core is sliced and assembled to impede the eddy current paths, decreasing the conductivity of the core without making material changes. In addition to the technique of lamination, iron may be mixed with other alloys like silicon or nickel to alter specific magnetic parameters and behaviors depending on the needs of the application. Laminated iron cores are generally favored for their high curie temperature, threshold to maintain magnetic properties, and high saturation flux density which are both attributed to their atomic compositions. However, these cores are typically only considered for low and medium frequency applications because at higher frequencies, they face significant core losses due to hysteresis which is intrinsically directly related to increase in frequency and additional eddy current losses due to the introduction of high frequency specific phenomena like skin effect [21].

Powdered Cores

Powdered cores are created using a mixture of powdered metal alloys like iron and insulating materials like resin. The magnetic characteristics and behaviors of these kinds of cores can be easily altered through intentional selections regarding particle dimensions and composition percentages. Powdered cores typically have a low effective relative permeability because these particles and insulating materials intrinsically have gaps between them. These gaps act like distributed gaps in solid transformers in that they contribute to the magnetic path, increasing reluctance, and improve thermal dissipation by providing more opportunity for heat distribution. This characteristic is leveraged for applications where the core must avoid saturation under high dc currents. Particle sizing can also be used to avoid eddy current losses compared to laminated iron cores while having a similar, high magnetic flux saturation point. As a result, powdered cores are favored in medium to high frequency (< 200 kHz) applications which benefit from the effects of additional gaps [21].

Amorphous Cores

Amorphous cores are composed of a combination of ferromagnetic and metallic alloys with the goal of lowering their melting point during the manufacturing process to create their non-crystalline structure. Because of their metallic glass structure, amorphous cores can have high magnetic flux saturation, relative permeability, and Curie temperature while maintaining low core losses. Their low losses can be attributed to the lamination process and their low coercivity which allows them to not be as susceptible to magnetic lagging or hysteresis. Amorphous cores are used in various frequency ranges (< 200 kHz) depending on their material composition which may vary

its permeability and therefore flux density capabilities. This can be especially critical since non-crystalline materials are not as thermally stable as their crystalline counterparts so variation in flux density performance is likely [21].

Nanocrystalline Cores

Nanocrystalline cores are like amorphous cores in that they are composed of a ferromagnetic material, iron, and metallic alloys but their resulting atomic structure is described as crystalline at the nano-particle level. The nano-sized layers of the core combined with the lamination technique increase the resistivity of the core and mitigate losses due to eddy currents as a result. Nanocrystalline cores can attribute their atomic structure to their high permeability and thermal stability, resulting in a high flux density saturation point with comparatively low core losses[21].

Ferrite Cores

Ferrite cores are typically composed of iron oxide and other metals depending on the desired electromagnetic properties for the application. For example, the two most common variations of ferrite are manganese-zinc (Mn-Zn) and nickel-zinc (Ni-Zn) which are favored for opposite frequency ranges due to their opposing magnetic characteristics. Starting with the latter, Ni-Zn is favored for frequencies in the mega-hertz range because their high electrical resistivity mitigates eddy current losses which are usually amplified by higher frequency in previously mentioned core materials. Ni-Zn has a high Curie temperature (> 300 C) and exhibits great magnetic anisotropy; however, its lower permeability limits its flux density saturation point compared to other ferrites and magnetic materials in general. On the other hand, Mn-Zn has a comparatively higher

permeability which facilities its higher flux density saturation. It is however limited to applications at frequencies < 1MHz due to its comparatively lower Curie temperature range (< 300 C, 100 C on average) and resulting core losses due to this thermal instability if realized. While Ni-Zn, which is more thermally stable, can also be used at lower frequencies, Mn-Zn is typically still favored from a cost perspective as the use of the nickel alloy makes Ni-Zn significantly more expensive than Mn-Zn [21][19].

HFT Material Selection

For HFTs in the 300 - 500 kHz range, Mn-Zn ferrite is a common choice for its high performance to cost ratio. Its high permeability enables the maximum saturation flux density for ferrites and its intrinsic atomic properties which enable its comparatively lower core losses at such operating points. Three different soft ferrite manufacturers were researched for this transformer prototype and two high frequency materials were chosen for analysis based on manufacturer recommendation. First, the magnetic characteristics and operation of core material candidates were analyzed. Table III shows each material considered with their magnetic characteristics.

Table III: High Frequency Ferrite Materials Evaluated.

Material	Permeability, μ_i	Curie Temp, T_c	Frequency, f	Saturation Flux, B_{sat}
ML95S	1100	280	>500 kHz	430 mT
N49	1500	240	>300 kHz	400 mT
3F36	1600	230	>300 kHz	420 mT

To understand and compare material behaviors, each material's core loss per volume was plotted at two different flux density values (50 mT and 100 mT) across a reasonable operational temperature range. Figure 12 shows a temperature versus core loss per volume plot of high

frequency soft ferrite materials from Ferroxcube, TDK EPCOS, and Proterial (formerly Hitachi)[22]–[24].

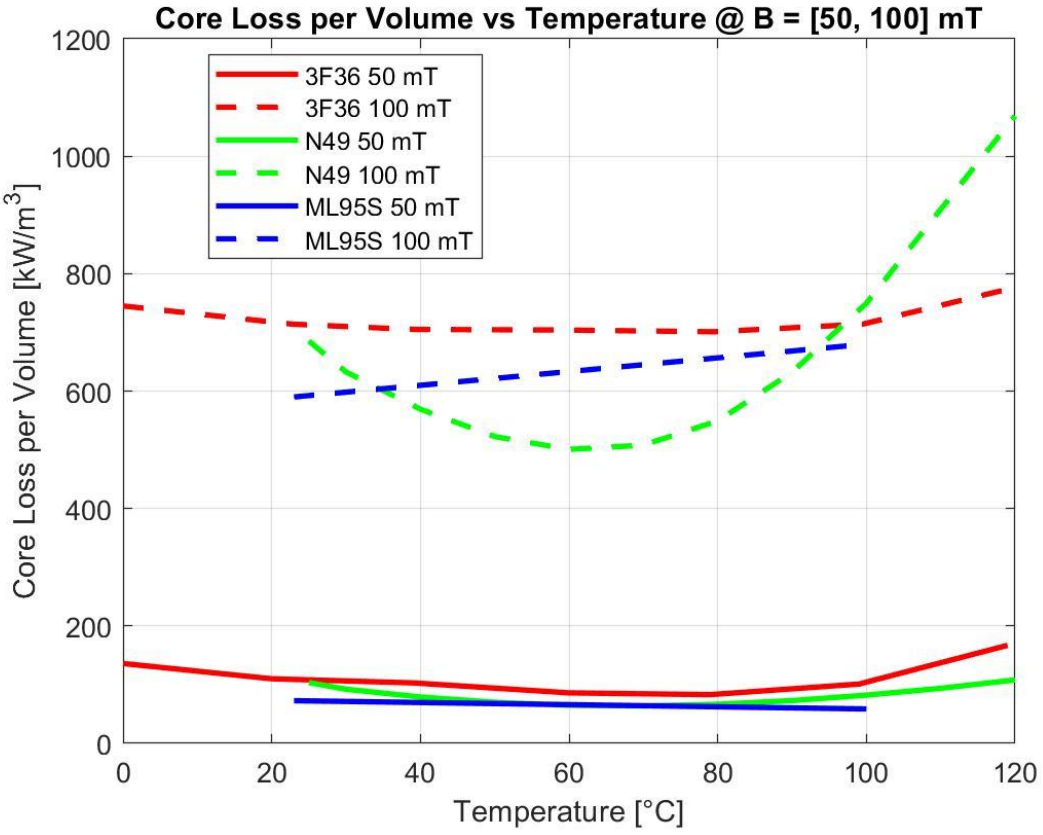


Figure 12: Temperature versus core loss per volume plot of three different high frequency ferrite materials at two different flux densities[22]–[24]**.**

ML94S from Proterial shows the most stable and linear core loss per volume as core temperature rises. It has the lowest core losses per volume at 50 mT compared to all of the surveyed materials. However, it has higher core losses per volume at 100 mT than 3F36 at both flux density operating points, though exhibiting a linear relationship with increasing temperature. It is important that the selected material exhibits stability at higher temperatures and reasonable losses at higher flux densities. Even if the transformer is designed for a flux density of 50 mT, the flux density distribution inside the transformer core volume will not be uniform meaning that it should be

expected that there are flux density and/or temperature hot spots throughout the core. These hot spots will contribute greatly to core loss and lower the overall efficiency of the transformer. Therefore, it is important to select a material that has reasonable operation at higher flux densities and temperatures. An example of comparatively non-ideal material performance would be the N49 material shown in Figure 12. At the 50 mT operation point, the N49 material has similarly low core losses per volume to the ML94S material. However, at 100 mT, the N49 material exhibits unstable, exponential core losses per volume across the operational temperature, especially at temperatures exceeding 100 C. For high frequency transformers, reaching operational temperatures of > 90 C is an expected reality so it is not unreasonable to select a core material which has the best performance at higher temperatures. As a result, Ferroxcube's 3F36 was chosen as the core material for this transformer. [25] also provides a comparison of similar high frequency materials. Figure 13 shows a plot of the high frequency materials reviewed where similar trends between N49 and 3F36 can be seen.

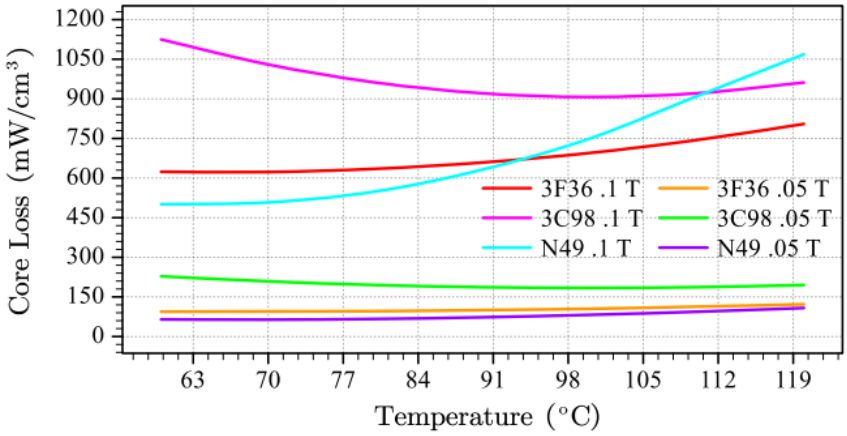


Figure 13: Shown are the core losses per volume of some high frequency materials at two different flux density operation points across temperature.

3F36 was also identified as the material which would be able to provide the most stable core losses per volume across a reasonable transformer core operational temperature range by comparing the

change in losses from 60 C to 100 C for both materials at 100 mT. N49's delta losses are almost three times higher than 3F36's. In addition to flux density and temperature, the operating frequency of the transformer also impacts the magnetic material behavior. This analysis primarily focused on the behavior of the materials at 500 kHz. [14] presents a discussion of the impact of the transformer operational frequency on transformer design by analyzing the core losses per volume for different high frequency materials at varying high frequencies with the purpose of achieving the smallest transformer core dimensions. Their analysis concluded that the best reduction in transformer volume can be achieved using Ferroxcube's 3C98 from 200 kHz to 300 kHz, Ferroxcube's 3F36 for > 400 kHz, and Proterials' ML95S for >500 kHz. This aligns with the approximately 500 kHz material analysis presented in Figure 12 which resulted in the usage of 3F36 for this >400 kHz transformer prototype.

Core Dimensions Considerations and Analysis

In an effort to improve the manufacturability of the transformer prototype and the overall iPEBB, a standard U core shape was targeted. The U core shape allows for the redesigned transformer prototype to maintain the key design elements of the previous design like the split-core and planar, parallel windings. Preliminary calculations using Equation (9) were completed to determine if any readily available U cores could be used, however, at the time of transformer prototyping, the options were too small to accommodate planar windings. Therefore, a custom U core was designed for the realization of this transformer prototype. Because the core still maintains a standard shape, manufacturability is still improved compared to the previous transformer prototype which cut core blocks and individual legs out of larger core block pieces. To use a custom core, the transformer core design process was limited to maximum size restrictions instilled by the manufacturer. The

maximum U core which could be developed is U110/110/35. With the understanding from the previous design that the number of turns would at <=5, the transformer window needed to be at least 50 by 50 mm to accommodate the parallel, planar windings. This window size limited the length of the core legs to 30 mm each. Based on preliminary calculations with Equation (9), it was apparent that a reasonable operational flux density could not be achieved with a core area, specifically core depth of 35 mm. To overcome the restrictions from the manufacturer, the transformer core was designed with the understanding that separate U core pieces would be placed adjacently to increase the overall core area while maintaining the core window dimensions.

To work in parallel with the resonant converter design, an ideal switching frequency range (400 – 460 kHz) for SST operation was provided. Using Equation (9), core depths were calculated assuming a fixed core leg length of 30 mm, the ideal switching frequency range, and an ideal flux density range (50 mT to 80 mT). This flux density range is supported by the previous magnetic material behavior discussion regarding the operating flux densities impact on core losses. Table IV shows the result of this parameter sweep.

Table IV: Parameter sweep of frequency and core depth.

	U Core Depth [mm]			
F_{sw} [kHz]	**B = 50 mT**	**B = 60 mT**	**B = 70 mT**	**B = 80 mT**
400	104.1	86.8	74.4	65.1
410	101.6	84.6	72.5	63.5
420	99.2	82.6	70.8	62
430	96.8	80.7	69.2	60.5
440	94.6	78.9	67.6	59.1
450	92.5	77.1	66.1	57.8
460	90.5	75.4	64.7	56.6

The purpose of this core depth analysis is identifying a range of reasonably achievable core dimensions from a manufacturing and transformer operation perspective. The design process was limited to a maximum of two adjacent cores so to not negatively contribute to the wire length of

each winding turn. Figure 14 shows the four transformer core pairs that were chosen for further analysis.

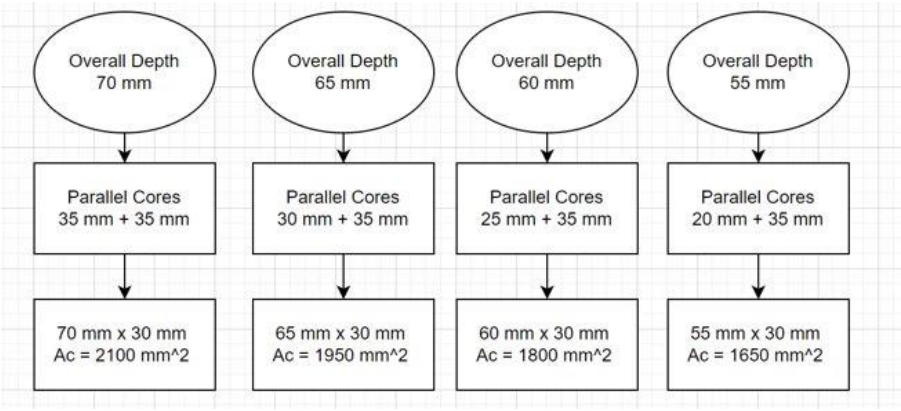


Figure 14: Shown are the pairs of different U cores which achieve may achieve reasonable transformer operation.

Equation (9) was used to re-calculate the flux densities in the desired frequency range for these specific transformer depths to determine whether the transformer would be operating under reasonable conditions. This is necessary because as we consider decreasing the switching frequency, the operational flux density will increase per their inverse relationship highlighted in Equation (9). Switching frequency and transformer core pair combinations which greatly exceeded a flux density of 80 mT were eliminated from design considerations. The remaining combinations, along with the resulting magnetizing inductance calculated using Equation (4),were used to re-simulate CLLC resonant converter operation to create a design space of operational points where ZVS is achieved. Table V details the initial picks for a 1000 V/100 A HFT based on balancing resonant converter operation and transformer operation. Figure 15 presents a simplified illustration of the cores, sectioned into their four parts.

Table V: Transformer Prototype Design Options

Design #	F_s	L_m	B	Core Area	Core Volume	Core Loss
(1)	430 kHz	8.1 uH	80.75 mT	1800 mm^2	576,000 mm^3	134.41 W
(2)	405 kHz	8.7 uH	79.13 mT	1950 mm^2	624,000 mm^3	125.07 W

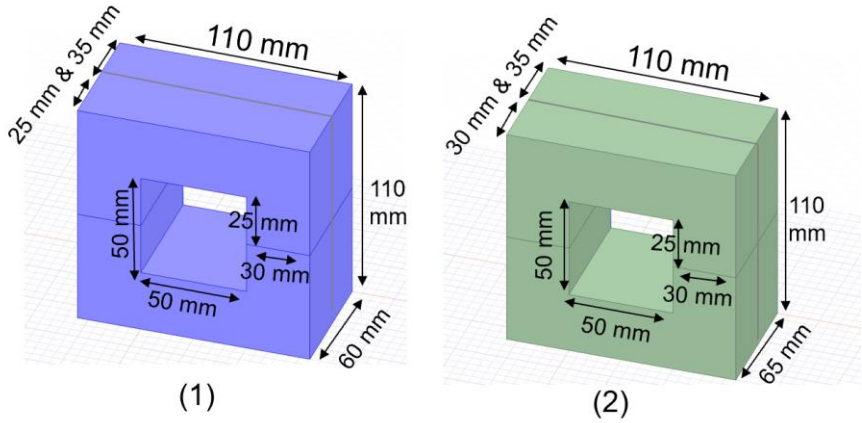


Figure 15: 3D transformer cores in four parts where (1) corresponds to a 430 kHz design and (2) corresponds to a 405 kHz design.

The core loss of each design was estimated analytically using the recommended variation of the Steinmetz equation by the manufacturer via the material data sheet, along with the provided empirically determined Steinmetz coefficients. [26] introduced what is now referred to as the Original Steinmetz equation (OSE) where core loss due to hysteresis and eddy currents are estimated through empirically measured coefficients during sinusoidal operation of the magnetic material, frequency, and magnetic flux density. The 3F36 Ferroxcube date sheet presents an empirical fit formula based on the Original Steinmetz equation to include operational temperature coefficients, shown in Equation (10)[24].

$$P_v = C_m f^x B^y (Ct_2 T^2 - Ct_1 T + Ct) \left[\frac{mW}{Cm^3}\right] \tag{10}$$

Despite being recommended by the manufacturer, core loss calculated using the OSE and empirical coefficients is an approximation at best with many disqualifying factors or error due to assumptions. This is because the empirically defined coefficients are generated from sinusoidally excited test cores. Therefore, the OSE is not valid for core loss estimation for transformers which

are exited with non-sinusoidal waveforms which is typical for most power electronics and converters. Furthermore, the Steinmetz parameters do not scale accurately with frequency and do not take harmonics into account [25], [27], [28]. Researchers have proposed alternative analytical equations for core loss based on the OSE to address concerns about accuracy and to account for non-sinusoidal excitations. The theory behind Modified Steinmetz Equation (MSE) is based on domain wall motion and losses incurred as a result. This phenomenon can be described using the change in flux density over time. The goal of the MSE is to provide a way to calculate core loss for non-sinusoidal waveforms. However, the MSE's accuracy is limited to instances where the coefficient alpha, the power of frequency, is approximately 2, meaning that it cannot be used as a one fits all for all waveforms[29] . The Generalized Steinmetz Equation (GSE) describes core loss as the instantaneous power loss depending only on flux density and change in flux density, however, it is not consistently better than the MSE, so it was further adopted into the Improved Generalized Steinmetz Equation (iGSE) [30], [31]. The iGSE states that losses are dependent on the whole magnetism cycle or waveform, rather than just time varying magnetic flux. The major improvement between the GSE and the iGSE involves addressing major and minor hysteresis loops. Usually, hysteresis is represented using one B-H loop of the core material under testing. However, when pursuing an accurate analytical calculation of the losses due to core loss, hysteresis must be broken down into its major and minor loop. The major hysteresis loop is the magnetic curve which is typically represented in material data sheets which shows the flux density versus the magnetic field from both polarities of saturation. This plot usually fails to show the minor hysteresis loop which takes note of magnetic behavior only before saturation [26], [32], [33]. The Natural Steinmetz Equation (NSE) is another, independently formulated, version of the iGSE. While both the iGSE and NSE incorporate major and minor loops, greatly improving their

accuracy aside from applications with small duty cycles, they completely fail to address the impact that DC bias has on the magnetization of the core as well as the impact of waveforms which implement zero voltage instances. To address these concerns, the Improved-Improved Generalized Steinmetz Equation (i^2GSE) was developed, however, the iGSE is widely used since it covers all of the key concerns for the analytical calculation of core loss. Ultimately, the analytical calculation of core loss, no matter how refined the equations are, cannot fully account for the practical application and behavior of a transformer core in a system so experimental verification of core loss is ideal for definitive transformer core magnetic performance verification [25], [27], [28]. Therefore, this work takes a simple approach to analytical core loss calculation by using Equation (10) as recommended in the core material data sheet with plans to experimentally verify the core loss of the transformer. This analytical calculation for core loss is therefore used to get a general sense of how this magnetic material and transformer prototype may compare to its predecessor as well as to perform basic thermal performance simulations.

Magnetic Simulation of Transformer

The magnetic flux density of the core was simulated in ANSYS Maxwell 2D AC Conduction Solver with an open circuited excitation circuit with a current source equivalent to the approximate magnetizing current, calculated using Equation (2). Figure 16 shows the 2D model used for the simulation of the magnetic flux density in the transformer core.

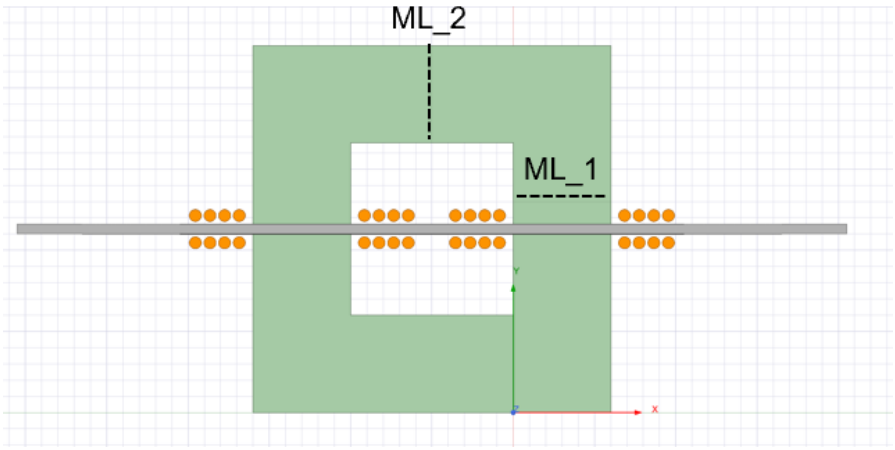


Figure 16: Shown is the 2D model of the proposed transformer with two measurement lines in the areas of interest for flux distribution.

At measurement line one (ML 1) the root mean square (RMS) magnetic flux density was 66.01 mT and at measurement line two (ML 2) the magnetic flux density RMS was 67 mT. Figure 17 shows the magnetic flux distribution in the core, insulation sheet, and surrounding air region.

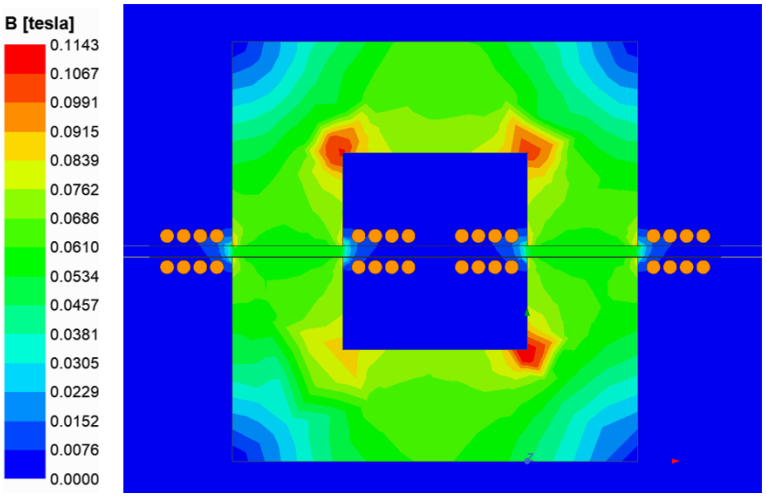


Figure 17: Shown is the magnetic flux density magnitude plot of the proposed transformer.

The flux distribution in the core ranges from near zero at the outer edges of the core to 114.3 mT at the edges of the core window. The magnetic flux distribution in a transformer core is impacted by eddy current induced in the core and the core reluctance. Magnetic flux tends to crowd around

edges because it takes the path of least reluctance. Therefore, it specifically crowds around the edges of the core window and the edges of the core legs where the “air” (mica sheet) gap is employed. An approximation of the magnetizing inductance of the transformer may also be extracted from this simulation set up via the calculation of the matrix. From this, the simulated magnetizing inductance of the transformer is 8.15 uH whereas the analytically calculated magnetizing inductance is 8.7 uH. This is an expected difference considering the 2D FEA simulation does not fully take into account 3D magnetic effects and the analytical calculation assumes a uniform flux distribution which is not the case for transformers of this size and operation.

High Frequency Winding Considerations

In HFT design, the windings must be selected and integrated to support reliable performance and mitigate losses. The winding losses in HFTs are due to dc resistance, known as I^2R losses and more significantly, ac high frequency phenomena like skin effect and proximity effect. Skin effect refers to the inclination of ac current through a conductor to crowd around the perimeter of said conductor. The depth by which this current penetrates the conductor is called the skin depth [19]. This effect occurs because of opposing eddy currents which negates the flow of current through the center of the conductor. By Faraday’s law, ac current traveling through a wire will induce an alternating magnetic field around said wire. This magnetic field, by Lenz’s law, will induce opposing eddy currents with an orientation and direction that opposes the flow of current at the center of the wire while supporting the flow of current at the edges of the wire[19]. The skin effect may be overcome if the skin depth of the wire greatly exceeds the wire thickness. Skin depth is

directly proportional to the resistivity of the wire material and indirectly proportional to the operational frequency and permeability as shown in Equation (11)[19].

$$\delta = \sqrt{\frac{\rho}{\pi * f * \mu}} \tag{11}$$

As frequency increases, the depth at which current can penetrate a single conductor decreases significantly. Therefore, skin effect is more severe in wires operating at high frequencies and must be specifically considered in HFT winding selection. Similarly, proximity effect is another high frequency phenomenon that contributes to current crowding; however, it is due to externally induced eddy currents from nearby conductors. The proximity effect also scales with frequency since the magnitude of the induced eddy currents are directly proportional to the frequency of the ac source. These phenomena which limit the flow of current in a conductor increase the resistance of the conductor thereby increasing the ac winding losses.

Overview of Transformer Windings

The type of wire which can be reasonably used in HFTs is limited by these high frequency effects and the anticipated operational temperatures of the transformer. [25] provides an overview of commonly used winding materials for transformers considering these conditions. Helical flat wires are not appropriate for HFT which aim to operate at > 50 kHz as they are not manufactured at a thickness which can make skin effect negligible. Similarly, foil windings for > 100 kHz, high current HFTs do not result in compact transformer designs because of the wire thickness and winding configuration required to mitigate skin effect. PCB-based HFTs have been explored in great detail in SSTs for their precise manufacturability, affordability, and high voltage isolation. The dimensions and structure of PCB windings can be carefully designed to promote an overall

compact transformer design with mitigated winding loss. The main limiting factor of PCB windings for some HFTs and/or their applications is the generally poor thermal conductivity of the winding material and surrounding insulation as described in [25]. PCB-based HFTs are therefore limited in regard to achievable power density without compromising thermal performance via increased hot spots between winding and insulation layers. Recently demonstrated PCB-based HFTs with similar resonant converter SSTs which achieve >400 kHz operation does not exceed an 18-kW output, with the most recent demonstration being a 500 kW, 12 kW Electronic Embedded Transformer (EET) [34].

To achieve a > 400 kHz, high current transformer with medium voltage isolation, litz wire is selected for the transformer winding. Litz wires are a type of multistrand conductor where small strands of wire are bundled and twisted together to form one cohesive wire, insulated depending on the application [19]. Because the conductive cross-sectional area is made up of smaller conductors, if the litz wire is selected correctly it can reduce ac winding losses due to skin effect and proximity effect. Strand sizes and amount are chosen based on the resulting skin depth of the operational frequency so that when they are bundled, they combine to the total desired current by increasing the area where current can flow at said frequency. The twisting and bundling of these strands can be designed to avoid external magnetic field interactions between each strand, therefore reducing proximity effect.

Litz Wire Selection for HFTs

[14] presents the calculation of the skin depth using Equation (8) and recommended American Wire Gauge (AWG) for each operational frequency where strand diameter and skin depth share a 1 to 2 ratio. This assumption also aligns with litz wire vendor recommendations regarding

frequency and strand AWG [35]. Combining these two recommendations, 44 AWG strands are most suited for >400 kHz operation until near the MHz range. A planar winding structure was employed to support a compact transformer design. To achieve an output current of 100 A, a pair of planar coils were paralleled on each side of the transformer. This transformer uses an overall 8 AWG litz wire with 5x5x3/56/44 strand configuration. Considering the expected operational temperature of a HFT, the wire is insulated with single polyurethane-nylon and a FEP jacket giving it an overall diameter of 0.211". This wire was recommended by Cooner Wire for 50 A, 125 C operation. Aside from manufacturer recommendation, in-stock or off the shelf litz wire may be evaluated by comparing the copper cross sectional area created by the strands to a standard current rating by AWG table with consideration of +/- 20% to account for overrating and/or litz construction factors [36].

Transformer Winding Loss Calculation and Simulation

To gain a meaningful understanding of the potential performance of a HFT during the design process, the winding losses of the coils must be estimated. Transformer winding losses are important because they impact the efficiency of the transformer and overall SST as well as contribute greatly to the thermal performance of the transformer. Historically, there have been many methods for analytical calculation of transformer winding losses. [37] classifies these previous methods into three categories while proposing an additional method for winding loss calculation: precise calculation using cylindrical conductors, approximation of the former using rectangular conductors, and calculation using the first terms of the series expansions of the previous methods. Some of the drawbacks of these methods are that they are not universal to all waveforms, have limited considerations for high frequency winding effects, and most importantly, do not consider 2-D field geometry which is critical for gapped transformers. Rather, these

methods are geared towards 1-D field geometries. [37] proposes the square-field-derivative (SFD) method which can be used to calculate winding losses in litz wire HFTs where 2-D and 3-D field effects are non-negligible by combining the calculation of eddy currents based on a uniform field (analytically) and a nonuniform field (from FEA Simulation). The final equation for the winding loss, shown in Equation (12). Equation (12) is further adapted in [25] by simplifying the change in magnetic flux density over time to a constant magnetic field value. Magnetic flux density is related to the magnetic field intensity by the permeability as shown in Equation (13) [21]. This relationship along with the 1-D magnetic plane wave equation, Equation (14), can be used to replace the magnetic flux density with magnetic field intensity of a coil, shown in Equation (15).

$$P_{e,j} = \frac{\pi l_{t,j} N_j d_{c,j}^4}{64\rho_c} \overline{\left\langle \left(\frac{dB}{dT}\right)^2 \right\rangle}_J \tag{12}$$

$$B = \mu H \tag{13}$$

$$H(t) = \frac{d}{dt}\sin(\omega t + \varphi) \tag{14}$$

$$P_{e,j} = \frac{\mu^2 \pi l_{t,j} N_j d_{c,j}^4}{128\rho_c} (H_o 2\pi f)_j^2 \tag{15}$$

For a litz wire, Equation (15) refers to the ac winding loss in one strand for that specific winding turn. Therefore, the ac winding loss in a litz wire is the single strand winding loss multiplied by the number of strands in said litz wire. The total ac winding loss for a coil is the sum of the ac winding loss for each turn of said coil. As shown in Equation (15), ac winding loss is dependent on the magnetic field intensity of a particular turn and the length of said turn [25]. An ANSYS

Maxwell AC Conduction simulation was set up to extract the magnetic field intensity values of the transformer winding using a similar 2D model as shown in Figure 16. Figure 18 shows a simplified 3D rendering of the transformer prototype. This was used to estimate the mean length turns for the transformer windings.

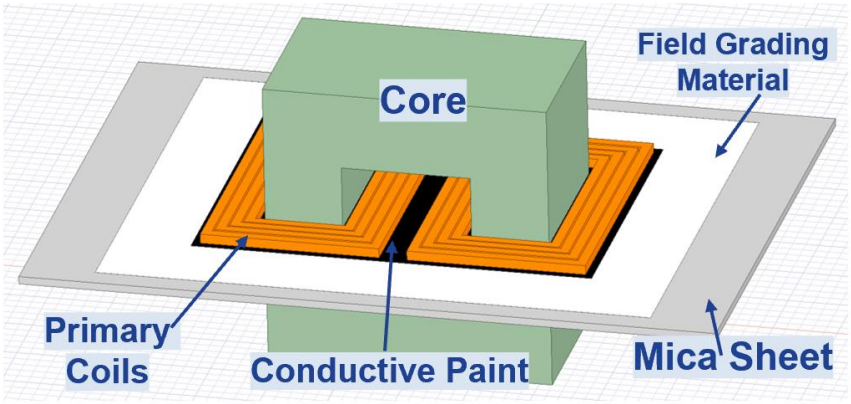


Figure 18: Shown is a simplified 3D model of the transformer prototype.

An external excitation circuit was set in ANSYS Maxwell to simulate a short circuit test where the transformer primary side is excited by the effective peak current (combination of the load current and magnetizing current) and the secondary side is shorted with an appropriately small resistor. The resulting total ac winding losses of the transformer prototype based on the extracted magnetic field intensity magnitudes is approximately 106 A. This calculation is an approximation because this method generally assumes that the magnetic field inside of the litz wire is distributed uniformly which will likely not be the case in practice. Further, the mean length turns were estimated with a simplified rectangular conductor instead of the round turns which will be realized during transformer assembly. To verify both the simulation set up and the accurate usage of this method, the winding loss of the previous transformer was calculated using this method for comparison to the known, measured winding loss. As others have reported, this method shows reasonable matching to measured losses. To compute the total winding loss of the transformer, the dc winding

loss must also be estimated. The dc winding loss is dependent of the mean length turn of the transformer winding, number of turns, the temperature coefficient of resistivity, maximum expected temperature, and the current through the winding, as shown in Equation (16) [21], [25].

$$P_{winding} = MLT * N * R_{dc} * \left(1 + \alpha_{20}(T_{max} - 20)\right) * I_{rms^2} \quad (16)$$

The dc winding loss was calculated for its worst-case temperature of 120 C, resulting in approximately 10 W bringing the total winding losses of the transformer to approximately 115.5 W. This short-circuited simulation set up can also be used to simulate the leakage inductance of the transformer windings. Figure 19 shows an adaptation of Figure 18 with one pair of primary and secondary coils.

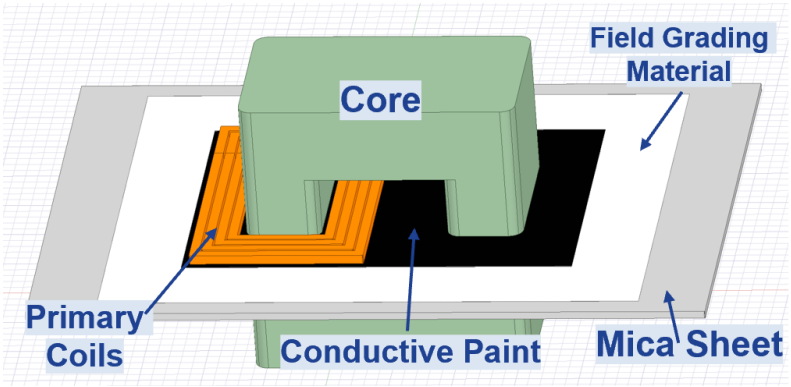


Figure 19: Shown is a simplified 3D model of the transformer with one pair of primary and secondary windings.

An estimation of the leakage inductance can be simulated in ANSYS Maxwell AC Conduction Solver with a simplified 3D model of the transformer as shown in Figure 19. One pair of coils is used to generate a 2x2 matrix where the coupling coefficient can be extracted from. This method capitalizes on the assumption that all of the transformer windings should be similar, so the resulting leakage inductance is of a pair of coils can be halved to find the total leakage inductance of two

pairs of parallel coils. The coupling coefficient is 0.94 and the resulting total leakage inductance was 0.3 uH per pair of coils. This leakage inductance can be used to estimate the size of the resonant capacitors needed to build the resonant converter. Because the transformer sides are symmetric, the resonant capacitors are approximately 0.3 uF.

Chapter 4: Insulation Design, Simulation, and Experimental Verification

History of Transformer Insulation

Transformers in industry are categorized as either oil-filled transformers or dry-type transformers [38]. These transformers employ different insulation strategies and components based on their applications and operational environments. Oil-filled transformers are valued for outdoor environments in applications that require reliable, long-term, high-power transformation. The main form of insulation for the oil-filled transformer is the oil which is cycled through the transformer, typically labeled as transformer or dielectric oil. Because the liquid can reliably cool the transformer coils, oil-filled transformers can use a wider variety of insulation components like pressboards or laminated wood rather than be limited to high temperature rated insulation materials. Oil-filled transformers are, however, greatly limited in their applications regardless of their reliability. For the oil cooling to be effective, maintenance on the quality of the liquid must be managed over time so it is free of impurities which may pose an operational and/or safety risk. Safety is a significant concern for oil-filled transformers considering how flammable they are. Finally, from a power density standpoint, while the oil-filled transformer is able to achieve high

voltage operation, it does so by significantly increasing the footprint of the overall system due to the size and weight the oil insulation enacts.

Dry-type transformers are favored for indoor applications where the use of transformer oil is not permissible due to safety. Therefore, any type of non-liquid insulated transformer is classified as a dry-type transformer [38][39]. The sub-classifications of dry-type transformers are based on the way their coils are wounded and the types of insulation materials and techniques they use. Layer-wound coils are created with alternating conductor and insulator layers (paper or glass polyester) to mitigate partial discharge between gaps in the layers. Disc-wound coils are supported structurally by glass polyester and cooling via air flow in gaps between coils. Cast-coil windings are directly insulated with resins made of polyester or epoxy which completely isolates them from the surrounding components. While these transformers are not accompanied by heavy weight liquid insulation, they still contribute greatly to the size of the overall system. Electronic power transformers which are smaller than the typical industrial dry-type transformer still use significant amounts of encapsulation, insulation tape, and large bobbins to achieve appropriate isolation and thermal performance [38]. In order for HFTs to be realized in industry, insulation designs which do not impede the isolation and thermal performance of the transformer must be developed and demonstrated.

State of the Art Transformer Insulation

In [14], a 500 kHz, 15 kW HFT is achieved with a medium-voltage insulation design. The insulation requirement was determined based on the highest input voltage level, 4160 V or 13.8 kVAC, resulting in a maximum insulation requirement of 30 kV. This was used to calculate the necessary creepage and clearance distances which must be achieved between windings [40]. The

first insulation technique employed was the encapsulation of the high voltage windings. If the high voltage windings degrade or come into contact with undesirable particles, it could lead to partial discharge and eventual system failure. This is avoided by using epoxy to create a barrier between the windings and the surrounding environment. The bobbin is the next critical part of the insulation system. The main purpose of the bobbin is to structurally support the windings, however, because it interfaces in the region around and between the high voltage and low voltage connections, it is important that the material and dimensions of the bobbin are selected to upload and support the insulation requirement. Specifically, dielectric strength and thermal conductivity are key parameters in insulation material selection as the electrical and thermal performance of the transformer must be balanced. An insulation tape is also chosen based on similar principles however it is unclear where exactly the tape was utilized in the transformer. [40] requires three insulation tests to be completed for compliance with the standard: basic lighting testing (BIL), applied voltage insulation test, and partial discharge (PD) testing. The BIL test is successful if the test waveform is smooth while the voltage is increased to the desired maximum insulation rated and during the decrease. The applied voltage insulation test checks for flash over or similar behavior while approaching the test voltage. Lastly the PD testing was completed at the multiples of the rated working voltage over approximately 210 seconds while the charge across the transformer was measured and evaluated for instances of sustained PD events. Overall, the proposed transformer adhered to [40] by demonstrating its passing of the three main insulation tests. However, there was no mention of what the thermal performance of the transformer was or what the intended cooling mechanisms would be if needed. Therefore, it is unclear if these insulation techniques serve as thermal barriers for when attempting higher operating points individually or though SST scaling.

[41] presents a 15 kW, 200 kHz HFT for a CLLC-based SST. The tradeoff between maintaining the size reduction benefit of the HFT while achieving the necessary insulation rating based on the input voltage is highlighted as a key challenge. HFT insulation systems are most concerned with failure due to overvoltage and long-term insulation damage via PD inside insulation layers and surrounding air. To address these concerns, the proposed transformer first encapsulates its high voltage windings and core window completely. This contrasts to [14] where only the primary windings were encapsulated and space between the core, bobbin, and windings was present. Instead, [41] uses a wide spread of encapsulation to distance the high voltage windings from the surrounding environment. While the encapsulation mitigates risks due to overvoltage, PD between the non-zero potential of the encapsulation layer and the grounded core is treated separately. To address this, a semiconductive shielding layer is applied around the encapsulation layer, filling the space which would exist between the core and the bulk insulation. A semiconductive material is used to avoid loss producing eddy currents which may be induced in completely conductive shielding paints. It is, however, unclear whether this is a linear or nonlinear semiconductive material and it was not discussed as to how this paint and its conductivity were selected. While the shielding layer mitigates PD from occurring between the bulk insulation and grounded core, it introduces the chance of PD occurring in the air at the terminations of the shielding layer where a triple point is created between the surrounding air, semiconductive layer, and insulation layer. At this triple point or meeting of materials with different dielectric and conductive properties, especially if a sharp corner is formed, the electric field crowds resulting in a high electric field intensity in that area [42], [43]. If this intensity exceeds the dielectric breakdown of air or the surrounding materials, then PD is likely to occur and degrade the system. To address this, a stress grading material is added at the termination of the semiconductive shielding layer. This material

grades the voltage across its length to mitigate the otherwise crowded electric field distribution at the triple point. However, it is not specified what kind of stress grading material was used and how it was selected. An overvoltage test and PD test were completed and passed at 34 kV RMS and 17.2 kV RMS, respectively. It was also concluded that silk-coated litz wires resulted in a higher partial discharge inception voltage (PDIV) because individual strands may be insulated with the encapsulant versus litz wires whose individual insulation serve as a barrier to encapsulation techniques. While a HFT was achieved with strong insulation performance, the structure is generally difficult to achieve and requires significant care during the manufacturing process. Furthermore, the thermal performance and/or thermal consequences of the insulation design was not discussed. For a HFT, it is very likely that has high power density with a compact design is achieved, the operational temperature of the transformer will be elevated. This may be especially true for transformers where the high voltage windings and core and completely encapsulated.

[44] presents an approximately 200 kHz transformer intended for MV SSTs. Like previously proposed transformers, this work aims to achieve an insulation design which may be compliant with established standards for MV SSTs like IEC-61800-5-1 which requires the proposed system to achieve an ac overvoltage of 29 kV RMS and a BIL of >95kV. Once more, insulation performance or rating must be balanced with its contribution to the transformer and overall SST footprint. It would be simple to increase the insulation thicknesses to achieve high performance, however this would counteract the compact design of the HFT as well as well as implement a thermal barrier between heat producing components and the intended air-cooling system. The first insulation technique implemented is the heavy encapsulation of the high voltage winding which serves as a barrier between the high voltage and the surrounding environment. This encapsulation

layer is then covered in a conductive shielding coating which fills the space between the secondary winding insulation and the high voltage winding encapsulation. This layer is described as both conductive and semiconductive without any material properties provided. It is also unclear how this material was made or selected for the application but assuming it is conductive enough, it is described to contain the electric field to the high voltage insulation. The addition of this layer introduces a triple point at its termination where the shielding layer ends into the surrounding air and primary insulation. Therefore, a stress grading material is introduced at the end of the shielding layer for a similar effect as described in [41]. The stress control layer is described as nonlinear and selected based on simulation, however simulation results nor the material selection process are not provided. Furthermore, there is no information provided on the composition nor behavior of this nonlinear material. BIL testing was successful up to 110 kV, however, PD testing was not completed so it is unclear whether sustained PD events either in the surrounding region or inside the bulk insulation would have an impact on the lifetime and performance of the transformer insulation. Thermal results for the transformer windings were also presented, identifying the peak winding temperature to be 106 C and 60 C across the high voltage insulation. The core temperature was not reported nor were thermal images of the transformer provided.

[8] presents a 500 kHz, 250 kVA transformer for an SST-based PEBB, previously introduced in Chapter 2 as the transformer this thesis is building off of. Unlike the previously proposed HFTs, this transformer insulation system proposes very minimal epoxy, if any, on the high voltage windings. The main insulation of this transformer is a 3 mm mica sheet which separates the primary and secondary sides of the transformer. The mica sheet is rated for >20 kV/mm and is responsible for providing isolation to the transformer and greater SST. To avoid PD in small spaces which may exist between the transformer windings, core, and mica sheet, a conductive paint, MG

Chemicals 838AR, is used to electrically tie these components and potential gaps. This coating was selected after surveying several conductive paints (nickel, static dissipative spray) and choosing the material which had the best application and did not contribute to losses via induced eddy currents. Like the effects that the addition of a shielding layer had in previously proposed transformers, the addition of this conductive layer creates a triple point in the surrounding region where the conductive layer terminates to the insulation layer and air environment. A semiconductive coating is introduced in this critical region to enable resistive field grading. However, information on the material composition nor behavior of this semiconductive coating is provided. Because the windings nor the transformer core are being encapsulated, they are completely exposed to air, so PD testing is integral to evaluating the performance of this insulation design. Further information and analysis of the insulation design of this transformer prototype is provided in [45], a precursor publication to the work that this chapter will focus and expand on.

Insulation Theory for MV/HV Applications

The key components in a high voltage system's insulation are the electrodes, insulators, and dielectrics. The electrodes are the charge carrying, conductive system components. The insulators provide isolation by not allowing any charge to transfer through the material. Dielectrics are similar to insulators in that they are non-conductors, but they do allow for conduction and displacement currents depending on the thermal and electrical conditions. To understand how the selection, positioning, and operation of these components in an insulation system affect its performance and rating, a strong understanding of the electric fields in those systems (and generally) must be established [43], [46]. The electric field describes the force that a charge exerts in space. At a defined point from the charge, the electric field intensity is estimated based on the

distance between the charge and the point. In the context of insulation systems and dielectrics, the electric field intensity, if the point is located in a dielectric, would be considered the electric stress or electric strength. This electric strength is used to classify the electrical properties of dielectric materials, typically labeled as dielectric strength in material technical sheets. The behavior of the electric field depends on the dielectric material properties, material geometry, and the environment which it is operating in.

For high voltage insulation systems, the main purpose of the insulation is to provide protection to the sensitive components in the system, support a long system life span, and provide isolation within or between systems. To fulfill this role, careful consideration must be given to avoid events or phenomena which may lead to the deterioration or complete breakdown of the insulation system. The breakdown of an insulation system can be categorized as either global or local breakdown. A global breakdown is the complete failure of the insulation to provide isolation and is typically accompanied by irreversible component or system level damage. A local breakdown refers to the occurrence of localized material degradation within an insulator or dielectric, typically referred to as partial discharge (PD). There are three types of PDs: corona, internal, and surface or 'tracking'[46]. Corona and surface PD both occur in gaseous dielectrics but surface breakdown, as the name indicates, occurs onto the surface of a solid or liquid in the gaseous environment. The likelihood of a dielectric experiencing any of these breakdowns is related to the nonuniformity of the electric field. Crowding electric field lines due to nonuniform electric field distributions is critical for insulation systems. The electric field intensity will be much larger in that region compared to the average electric field intensity across the entire system. High electric field intensities at points in the insulation are prime locations for partial discharge on the surface and within the insulation. Internal partial discharge occurs due to voids or other unintended, lower

dielectric constant particles inside the insulation layer(s). Dielectric constant is a material parameter of dielectrics and insulators which describes their ability to store energy. Inside of an insulation layer, if there is a void or particle present, typically it will have a lower dielectric constant than the surrounding material. For example, consider an air void in the encapsulation layer of a high voltage winding, a very likely scenario if the encapsulation is not properly vacuumed. The dielectric constant of air will be significantly lower than any encapsulation used for high voltage windings. The ability of the air to handle the energy or charge present is minimal, resulting in an intensified electric field in that region. The electric field may also be intensified due to the shape of a conductive or semiconductive material. Regardless of exact material classification, if a material is conductive enough, it will manipulate the electric field around its perimeter a voltage is applied. Specifically, if this material or layer has sharp edges or corners, then electric field lines will crowd in those areas. Electric field lines are perpendicular to the surface of their source. Therefore, in sharp, irregular regions, the electric field distribution will be nonuniform and crowded, resulting in an intensified electric field compared to the greater insulation region. These two concepts, dielectric gradients and corners/edges are frequently coupled in high voltage insulation systems. [42] discusses the presence of critical electric field regions in power modules caused by triple points (TPs) and how they may be accurately simulated with FEA tools for electric field mitigation solutions. A triple point is a region where two or more materials of varying dielectric constants met, typically at an electrode edge or layer termination. Because of the material properties and geometry of the region, the insulation system will typically see its highest, most critical field in these regions. The elimination or mitigation of these critical TPs are key to unlocking higher insulation ratings and better performance.

To reduce critical electric fields in an insulation system, steps should be taken to promote a uniform electric field distribution. The distribution of the electric field is closely related to and can be alternatively described by the potential gradient as shown in Equation (17) [46].

$$E = -\Delta V \tag{17}$$

If the potential across an insulation layer grades irregularly, then the resulting electric field calculated from the changing potential will be intensified in regions where the change in voltage is not constant. Most voltage grading techniques can be classified as either capacitive or resistive [47]. Capacitive field grading can be broken up into the following subcategories: geometric, refractive, and condenser. Geometric field grading is achieved through altering the shape of the conductor where the voltage is applied. For example, rounding the corners of copper pads in a module to reduce the electric field crowding at the otherwise sharp edges [48] . Another form of geometric field grading is conductive shielding where conductive materials are applied to critical areas for containment. Refractive field grading is achieved via manipulation of the gradient of permittivity's across the insulation layers. Permittivity is closely related the dielectric constant or relative permittivity of a material except it compares a material energy storage capability to a vacuum. A 'control', high permittivity material is introduced to the insulation design to redistribute the electric field stress between and across the layers. The usage of this method in ac systems is limited due to dielectric losses from the alternating, continuous polarization of charge(s) which scales with frequency [49] . Resistive field grading refers to the usage of resistive materials to control how the voltage grades in an insulation system therefore controlling the electric field intensity in critical regions. Resistive materials across an insulation layer can be modeled as a set of small, series resistors whereas the insulation layer can be represented as a capacitor. The voltage

grading in an insulation system can then be modeled as the voltage drops across these resistors. If a material is too resistive then the electric field lines will crowd in a different location, with minimal reduction. If the material is too conductive then no resistive field grading will occur. If the selection and implementation of the resistive material is optimized, then the tradeoff between field mitigation and unavoidable ohmic losses can be achieved. As of late, researchers have been investigating nonlinear resistive field grading techniques as an alternative to resistive field grading with a constant resistivity. Ohmic loss cannot be completely eliminated so long as a resistive material is being added to the system, however, the ohmic losses can be mitigated if the duration of the materials resistivity is optimized. Nonlinear resistive field grading features materials where conductivity is represented as a function of the electric field intensity. These materials are designed to have a baseline conductivity that changes in response to the electric field intensity at the area of application. The material is also designed for a particular switching field intensity when if realized in the area of application, the conductivity of the material changes to a value which is the bare minimum needed to achieve electric field grading. [47] provides a generalized function for describing the behavior of nonlinear resistive field grading materials (NLRMs). [50] builds upon this theoretical function and presents a breakdown on how a NLRM's properties may be selected to target a specific application or module and the impact of each parameter. The conductivity as a function of the electric field intensity is related to said electric field intensity (E), low-field conductivity (σ_o), switching field intensity (E_b), and the nonlinear coefficient (α), as shown in Equation (18).

$$\sigma_N(E) = \sigma_o\left(1 + \left(\frac{E}{E_b}\right)^{\alpha}\right) \tag{18}$$

Initial Prototype Insulation Evaluation

The initial transformer prototype which this thesis builds off of produced three iterations of transformer insulation sheets. Figure 20 shows the primary and secondary sides of each sheet iteration for the initial transformer prototype. Figure 21 shows the intended build sequence and incorporation of the insulation sheet into the transformer prototype.

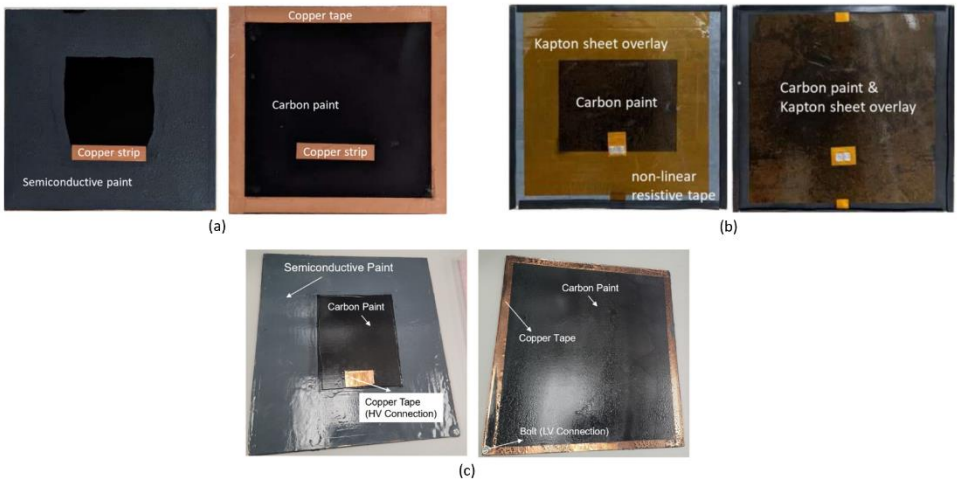


Figure 20: Shown are the transformer insulation sheet prototypes where (a) the first sheet using a semiconductive paint as the field grading agent (b) nonlinear resistive tape as the field grading agent and (c) a remake of (a) with improved building techniques

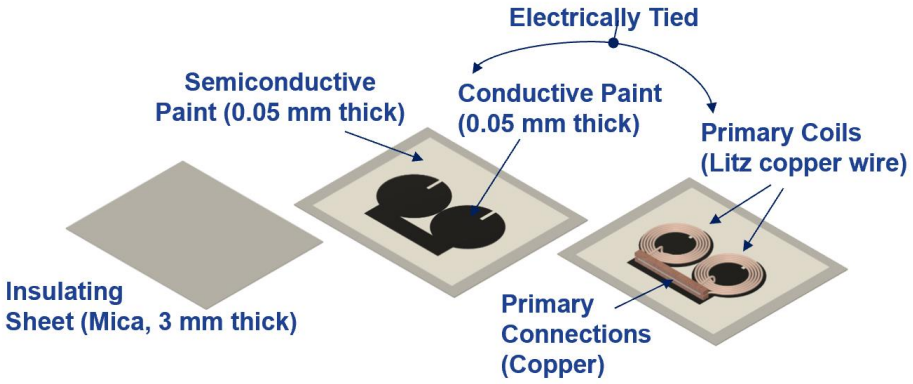


Figure 21: Build of the insulation sheet without the transformer core showing the coil shaped application of the conductive paint [8].

Previously, a hi-pot test was conducted at 30 kVAC for >1 min in compliance with the testing criteria for 15 kVAC class equipment. Figure 22 shows the initial sheet and transformer prototype which the first hi-pot test was conducted on.

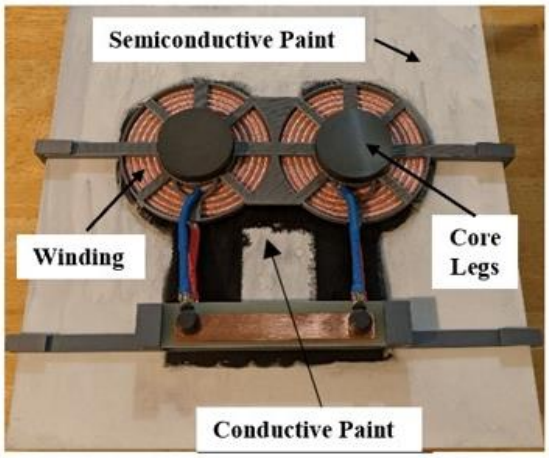


Figure 22: Top view of the previous transformer prototype with the windings and insulation sheet exposed mirroring Figure 21 [45]**.**

In this sheet, the mica sheet provided isolation between the high and low voltage sides of the transformer and the conductive and semiconductive paints lessened the airgap between the insulation sheet and the coils as well as facilitated the grading of the voltage across the insulation sheet. Figure 20 (a) and (b) were made based on the performance of the previously proposed insulation sheet. Figure 20 (a) features a conductive carbon paint in the coil region surrounded by a nonlinear resistive or semiconductive paint on the primary side. The secondary side of the sheet is completely covered with conductive paint with copper tape at the terminations of said paint. The edges of the semiconductive paint are grounded due to a connection to the secondary side copper tape edge via contact by nickel paint under, between the semiconductive paint and the secondary side copper tape edge. The conductive paint areas were covered with silicone conformal coating for protection. Figure 20 (b) features similar application of the conductive paint under the primary side coils but with a nonlinear resistive tape as the field grading medium. The sheet is generally

overlayed with Kapton tape for additional protection. The secondary side of Figure 20 (b) is comparable to Figure 20 (a). Both samples were hi-pot tested at 15 kVAC which is an adequate testing point for a 13.8 kVAC system that will have an 8 kVAC phase-ground operating voltage. Specifically, Figure 20 (a) completed over 100 hours at 15 kVAC. It was reported that there was some audible PD but there was no visible damage to the sheet. Figure 20 (a) and (b) were then tested for partial discharge (PD) verify and expand on the results of the discussed hi-pot tests as well as determine what the partial discharge inception voltage (PDIV) of the insulation sheets are. Figure 23 shows the general PD test set up used to measure the PDIV of the transformer insulation sheets.

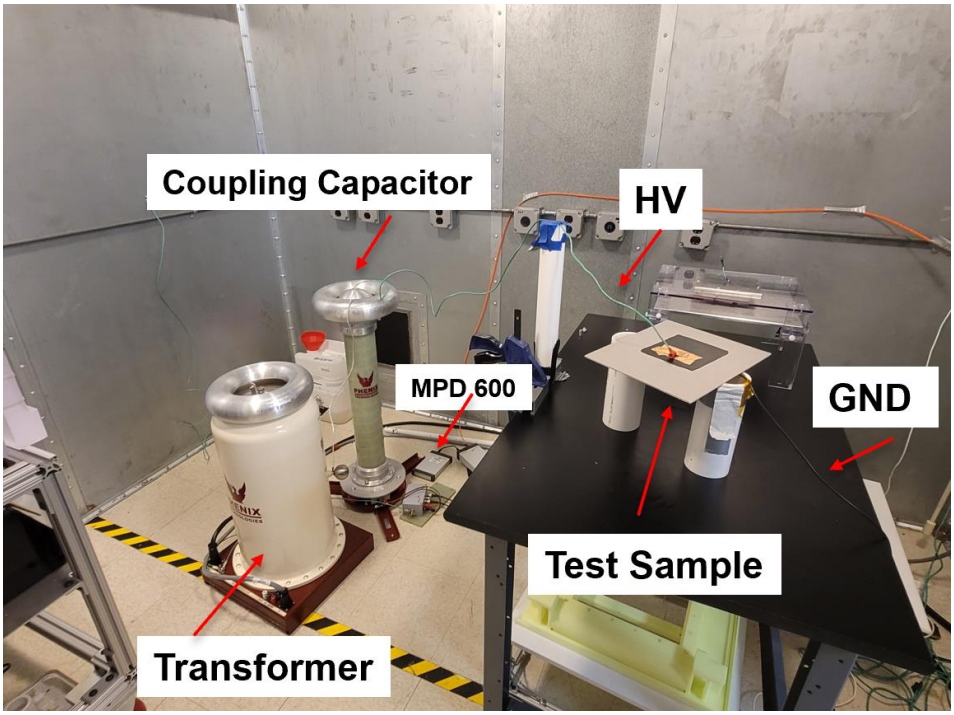


Figure 23: EMI chamber set up for PD testing of transformer insulation sheets.

The PD testing was performed in the air to measure the PDIV of the insulation sheets in an environment which is similar to its intended operation in the transformer. The OMICRON MPD 600 Partial Discharge Measuring System was used to perform the PDIV measurements. This

system utilizes an optical cable which reduces measurement noise between the EMI chamber and an outside computer to plot the partial discharge events over time across an applied voltage. As highlighted in Figure 23, a transformer is used to generate a 60 Hz input sine wave and a coupling capacitor was connected in parallel with the insulation sheet under test or test sample. The MPD 600 detects partial discharge in compliance with IEC 60270 by comparing the charge in the coupling capacitor to the known applied charge (10 pC) across the test sample. Figure 24 and Figure 25 show the PD test results of Figure 20 (a) and (b), respectively. The top graph shows the distribution of detected charges against the input voltage. The bottom graph shows (red) the voltage step up applied during testing and (green) the overall measured charge. At 4.1 kVrms there is PD detected in Figure 20 (a), but it is not sustained so the voltage was stepped up further. Figure 20 (b) experiences PD almost immediately. The PDIV of Figure 20 (a) was 4.5 kV_{rms} and 800 V_{rms} for Figure 20 (b). The significantly lower PDIV of Figure 20 (b) was expected due to difficulty with the application of the nonlinear resistive tape as well as gaps created by the Kapton tape. The PDIV of Figure 20 (a), however, was lower than expected considering the previous hi-pot test conducted. Upon examination of Figure 20 (a), it was concluded that inconsistencies in paint thickness and gaps/chipping may have contributed to the lower PDIV.

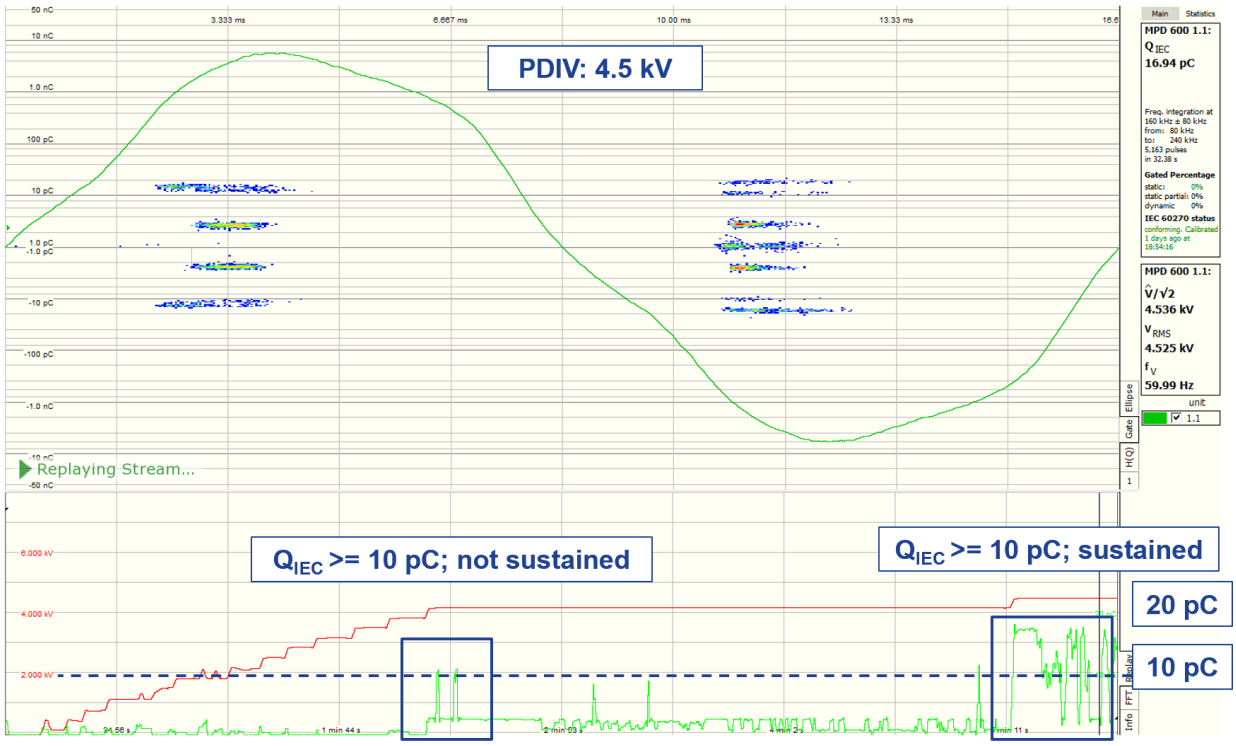


Figure 24: PD plot for Figure 20 (a) which utilizes a semiconductive paint for nonlinear field grading and conformal coating for paint protection.

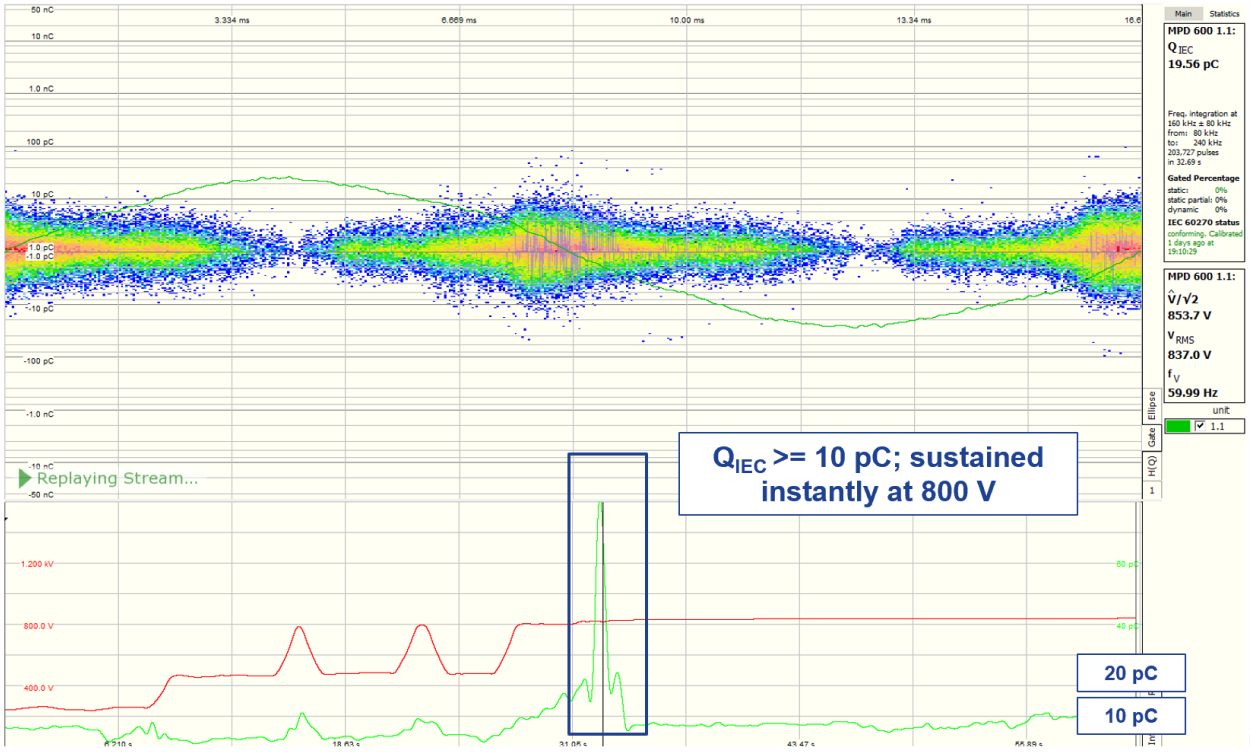


Figure 25: PD plot for Figure 20 (b) which utilizes a semiconductive tape for nonlinear field grading and Kapton for paint protection.

Figure 20 (c) was created based on the inferences drawn from the PDIV results of the previous sheets. This rendition of the semiconductive insulation sheet version had the most consistent application of the paints and easier access to the secondary side via a bolt screwed through the insulation. The primary side of this bolt was covered in an insulating gel to not skew the measurement and the secondary side of the bolt was connected to ground. Figure 26 shows the PD results of Figure 20 (c). The PDIV of Figure 20 (c) was 3.2 kV_{rms} , performing worse than the sample it was made to be an improvement of. Because there were no glaring reasons as to why the PDIV was significantly lower than expected, a layer-by-layer electric field study was completed to further access where the critical fields are and how they can be mitigated.

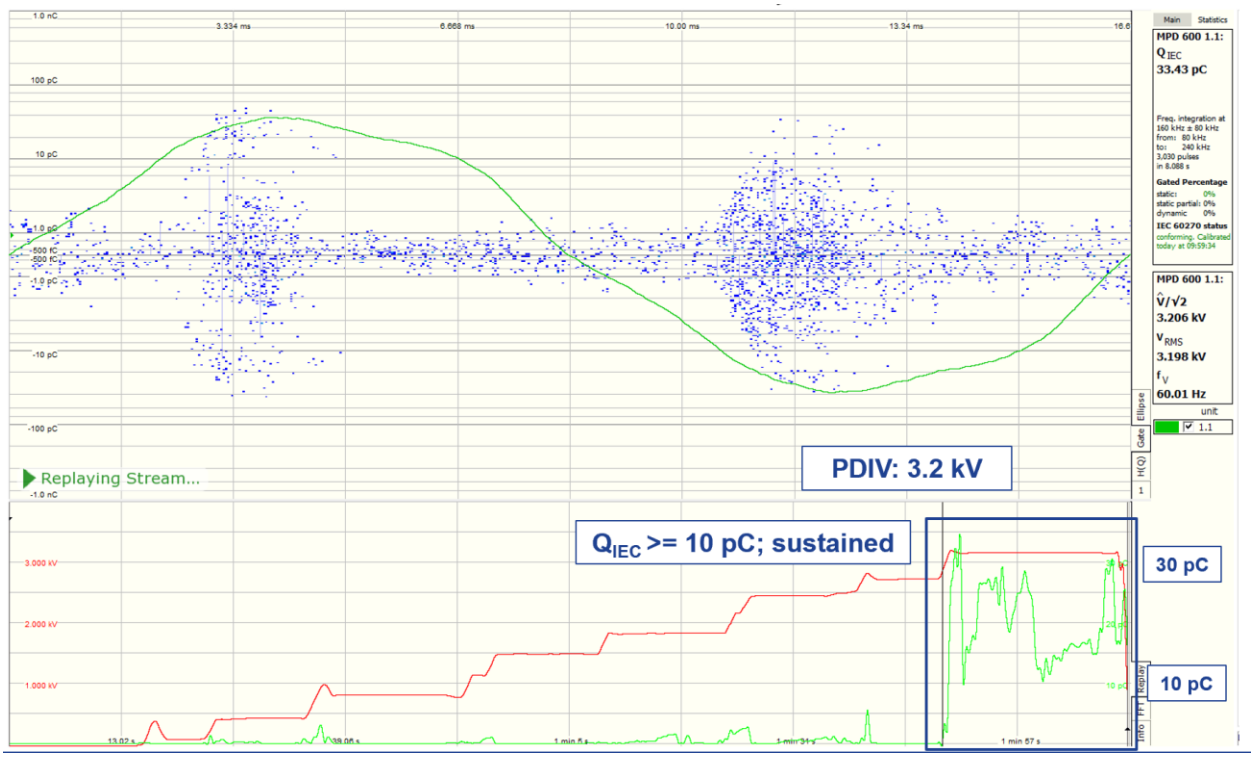


Figure 26: PD plot for Figure 20 (c) which utilizes a semiconductive paint for nonlinear field grading and conformal coating for paint protection.

Electric Field Study of Insulation Sheets

At the time of the conclusion of this work, there are no FEA tools to simulate PD nor PDIV. However, based on the previously discussed theory regarding high voltage insulation and electric fields, educated inferences can be made about where PD is most likely to occur and how the PDIV of different sheet configurations may compare. This study was prompted by the insights gained from the insulation testing and design of the Fastwatt insulation sheets. However, because the specific material properties of the paints used to create those sheets are unknown, this study is not a direct simulation of those exact sheets. Using ANSYS Maxwell, 2D AC Conduction simulations of voltage and electric field distributions can be solved for a 2D model of the transformer including the insulation sheet. Figure 27 shows the 3D transformer model where the 2D model was cut from. Figure 28 shows half of the 2D model with the critical points highlighted and Figure 29 zooms in

on these critical points on the primary side. Because the transformer is symmetric by both axes, the measurements extracted from one side will be identical to the other side. This allows for the model to be simplified, number of measurements to be minimized, and generally reduces the computational time and complexity of the simulation.

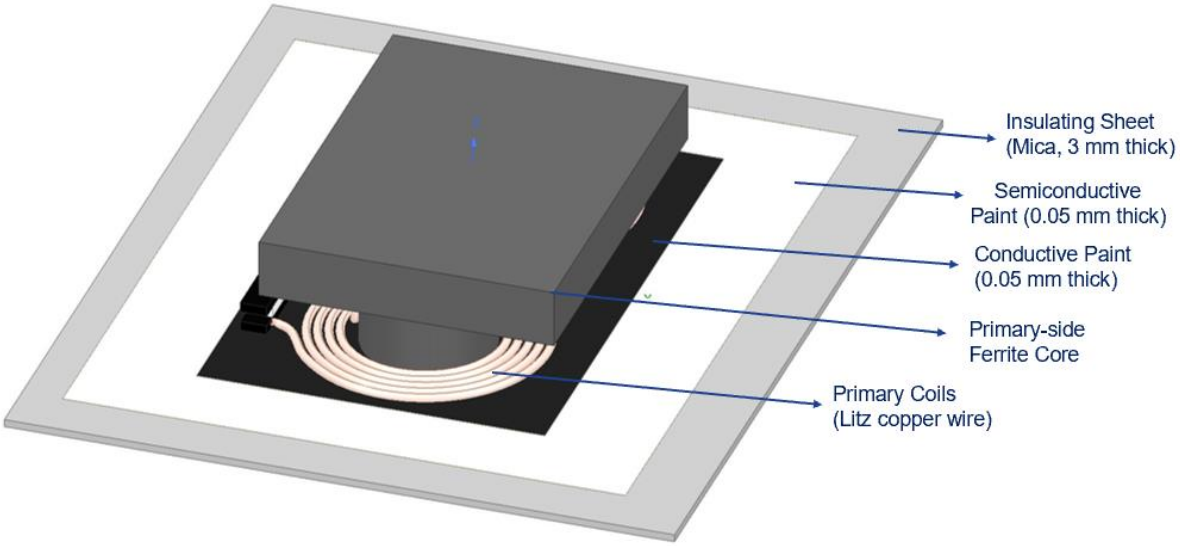


Figure 27: 3D model of the previous transformer prototype used for electric field simulation analysis.

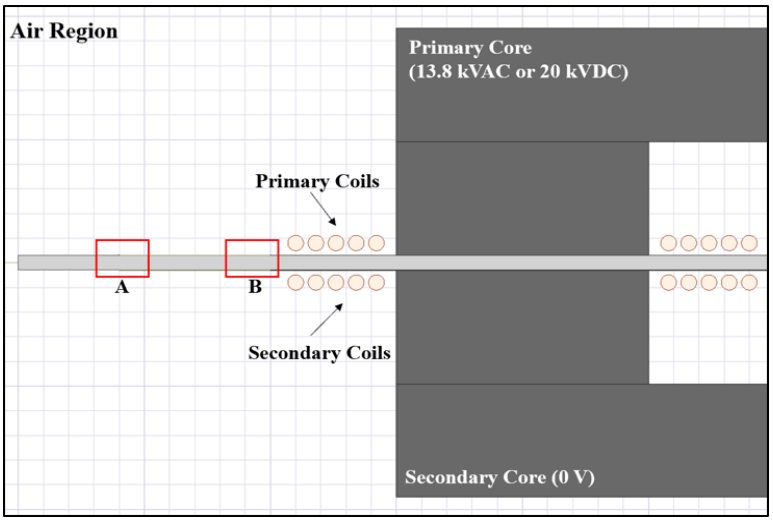


Figure 28: Half of the 2D model of the previous transformer prototype with the two expected critical points of the electric field identified [45].



Figure 29: Enhanced view of the expected critical points of the electric field where the (x) marks the triple point and the (.) represents the actual measurement point [45].

Similar to the previously discussed HFT insulation systems, a triple point is created at the termination of the conductive paint. To mitigate the expected intensified electric field, a linear, semiconductive paint is added to the termination of the conductive paint to first explore the behavior of linear, resistive field grading. Overall, based on the geometry and material properties of the insulation layers, two areas of interest or triple points are identified (Figure 29). Figure 29 (a) is expected to have intensified electric fields because the semiconductive sheet terminates at a corner into air (low dielectric constant) and the insulating mica sheet. Similarly, Figure 29 (b) is expected to have a less critical, but still intensified electric field because of the dielectric constant differences between the semiconductive and conductive paints compared to the surrounding air region [45]. The iPEBB and therefore the transformer is intended for use in both ac and dc distribution systems. Preliminary dc simulations with a voltage excitation of 20 kVDC applied to the primary coils and conductive sheet were completed but overall, the electric field analysis was focused on the simulation of ac operation. Ac simulations were completed in the ac conduction solver which assumes a sinusoidal excitation, set to 60 Hz with an applied voltage of 13.8 kVAC. The conductivities shown in Figure 29 for the paints are calculated using Equation (19) which is derived from the resistivity of the material [51]

$$\sigma = \frac{1}{R_{sheet} * thickness} \tag{19}$$

Using Equation (3), the conductivity of the conductive sheet was set to be approximately 179 S/m while the conductivity of a linear, semiconductive sheet was set to be approximately 2 S/m. To account for the smaller conductivities, the default insulator threshold value was decreased 1 pS/m so the low conductivity of the semiconductive sheet can be considered accurately in the solution [45]. Figure 29 also highlights how the electric field measurements are taken for the 2D simulations. [42] describes how simulation mesh and measurement points can be set up to obtain mesh-independent electric field results. The quality of a FEA simulation is critical for the observation of meaningful results. A mesh which captures the model and physical phenomena under the test will be independent of the results being extracted and provide a high-resolution output. This is especially important when generating voltage and electric field plots because the in addition to the specific magnitudes recorded at measurement points, the distribution of these parameters across the transformer will also be used for interpretation. Triple points typically occur at sharp edges or corners of power modules and models in general. Generally, when performing calculations at an edge or point with a small radius, the solution, if any, is considered a singularity which typically refers to an undefined point or limit. In FEA simulation tools, when solving fields at singularities, the simulation results become completely dependent on the simulation mesh settings rather than representing any physical phenomena occurring. If computationally possible, as the mesh of a simulation is further refined, the resulting solution will also vary. For some FEA tools, a result of zero may also be reported if taken directly at the triple point. To avoid this, [42] suggest taking electric field measurements at least 20 μm away from the triple point based on mesh parameter and distance from TP versus electric field sweeps conducted. To validate this method for the 2D transformer model considering the original application was for smaller power modules,

a sweep of the triple point shown in Figure 29 (a) was performed. Figure 30 shows the electric field across the measurement line shown in Figure 29(a) where 50 μm is identified as a safe distance where the electric field result is completely independent of the mesh.

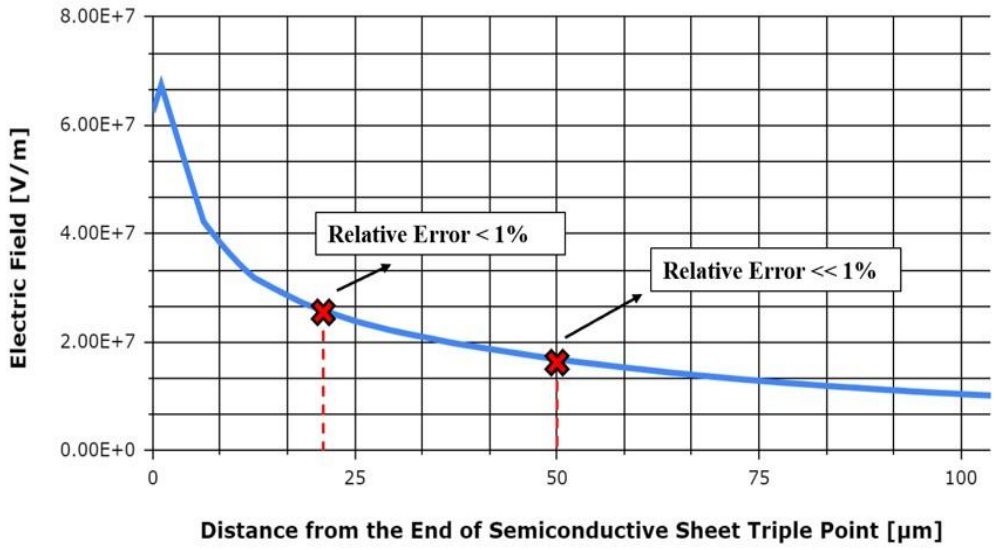


Figure 30: Electric field versus the distance across the measurement line in Fig. 10(a) starting from the triple point location [45].

The 2D transformer model was first simulated with only the 3 mm mica sheet. Figure 31 shows the resulting voltage plot and Figure 32 shows the resulting electric field plot. The voltage plot shows irregular voltage distribution created by the small spaces between the coils, mica sheet, and transformer core. The irregular or nonuniform voltage distribution gives way to intensified electric fields across the coils and transformer core edges, shown in Figure 32. The peak electric field is approximately 12 MV/m with most of the electric field intensity hovering at the 8 MV/m spectrum.

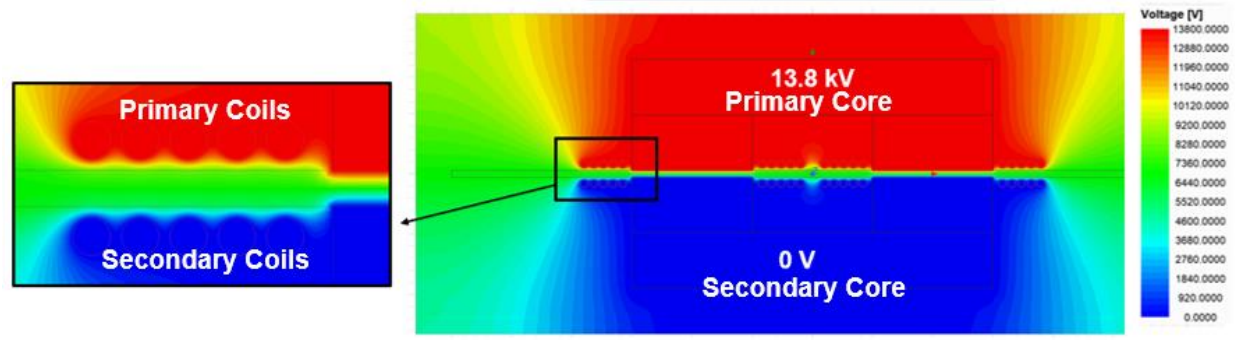


Figure 31: Voltage plot of the 2D transformer with only an insulating mica sheet.

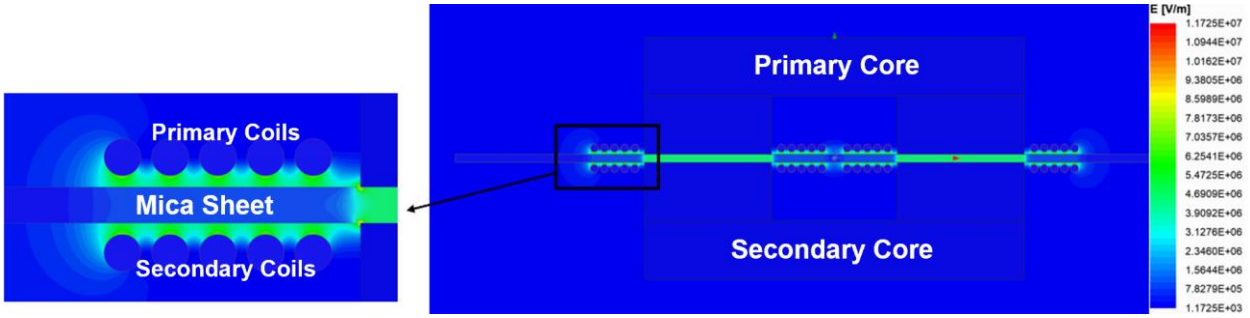


Figure 32: Electric field plot of the 2D transformer with only an insulating mica sheet with an enhanced view of the irregular field distribution around the core and coils.

The conductive paint was then added across the mica sheet, under the parallel coils and transformer on both the primary and secondary sides. Figure 33 shows the voltage plot with the conductive paint electrically tied to the coils via similar excitation assignments. Compared to Figure 31, the voltage distribution is much more uniform across the transformer. Its voltage gradient instead occurs only at the ends of the conductive paint. Figure 34 shows the resulting electric field plot influenced by the addition of the conductive paint. Because the voltage gradients within the transformer were made to be uniform, there are no visible electric field intensities across the transformer. As expected, based on the voltage plot, the intensified electric fields are concentrated at the ends of the conductive paint. The peak electric field was recorded at the end on the conductive paint as 16.7 MV/m. Despite the increased electric field magnitude, the conductive

paint facilitates the consolidation of critical areas into one main point. This allows for the focus to be on solutions for reduction in concentrated regions.

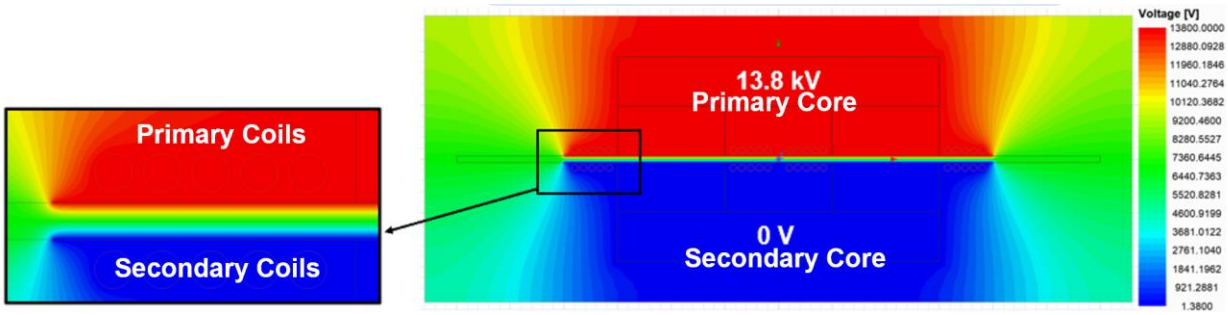


Figure 33: Voltage plot of the 2D transformer with the conductive paint applied.

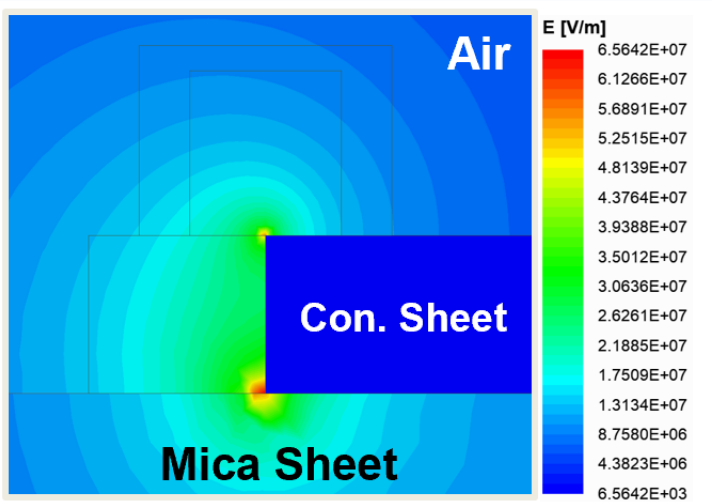


Figure 34: Electric field plot of the triple point shown in Figure 29(b) highlighting the end of the conductive sheet which was added to concentrate the peak electric field to one, treatable spot. [Note: Figure 29(a) is not applicable here because there is no semiconductive or field grading material applied in this simulation yet so the peak field is at the end of the conductive sheet].

These simulations conclude that the addition of the conductive paint is valuable to the insulation design, but further solutions must be realized for treating the TPs at the four corners of the transformer (two on the primary sides and two on the secondary sides). Two 2D transformer models were created to extract and analyze reasoning as to why the PDIV of the created transformer insulation sheets discussed previously were lower than anticipated. Figure 35 shows

the voltage plot of the insulation sheet configuration shown in Figure 28 with the ~2 S/m semiconductive paint applied to the terminations of the conductive paint. Rather than grading the voltage across its length, the semiconductive sheet serves as a medium for the electric field enhancement to shift across without any field mitigation. Figure 36 shows the resulting electric field plot due to the symmetric application of the semiconductive paint at the TPs of the 2D transformer model. The peak electric field as a result of the lack of voltage grading across the semiconductive paint is still 16.7 MV/m.

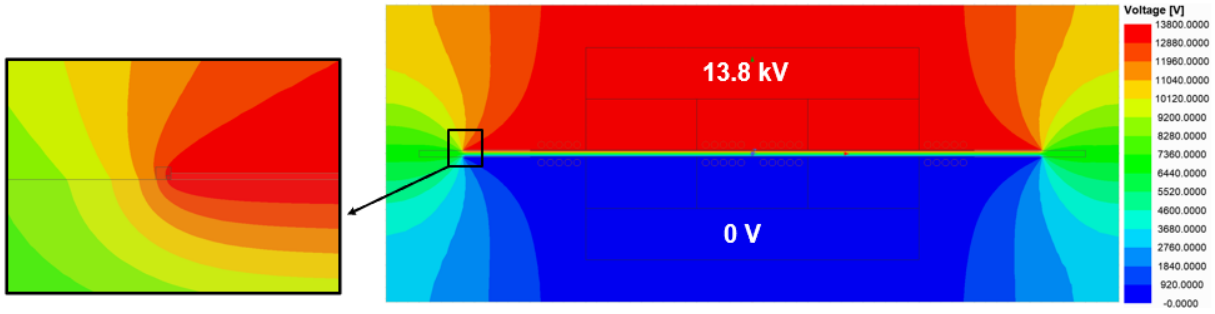


Figure 35: Voltage plot of the 2D transformer model with symmetric application of the semiconductive paint.

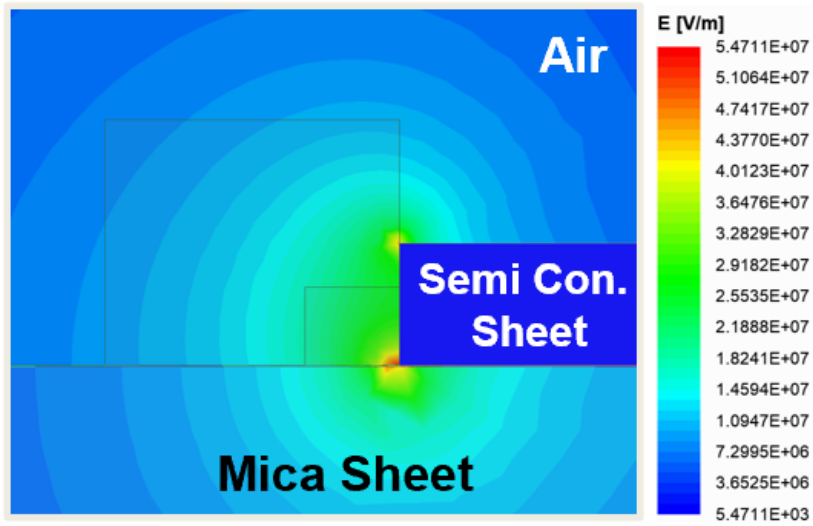


Figure 36: Enhanced electric field plot of the 2D transformer with symmetric application of the semiconductive paint and a focus on the peak electric field which shifted to the end of the semiconductive sheet from the end of conductive sheet previously shown in Figure 34.

The second 2D model created was strictly based on the paint configuration created for the actual sheet, Figure 20(a), along with including the copper tape to observe its influence of the voltage distribution of the terminations of the insulation sheet. Figure 37 shows the voltage plot for this model and Figure 38 shows the electric field plot with a focus on the terminations of the insulation sheet. This 2D model is different than all of the previous models because it does not feature a symmetric primary and secondary insulation design as seen in Figure 20(a). The voltage plot is mostly uniform across the transformer model; however, the voltage grading is completely pushed to the terminations of the insulation sheet. The semiconductive paint continues to not aid in the grading of the voltage across its length. However, the resulting peak electric field is reduced to 9.27 MV/m. Considering this peak electric field greatly exceeds the dielectric breakdown of air which is 3 MV/m, it is permissible that the created insulation sheets would have a low PDIV, and experience sustained partial discharges well before they even reach half of what their intended isolation rating is.

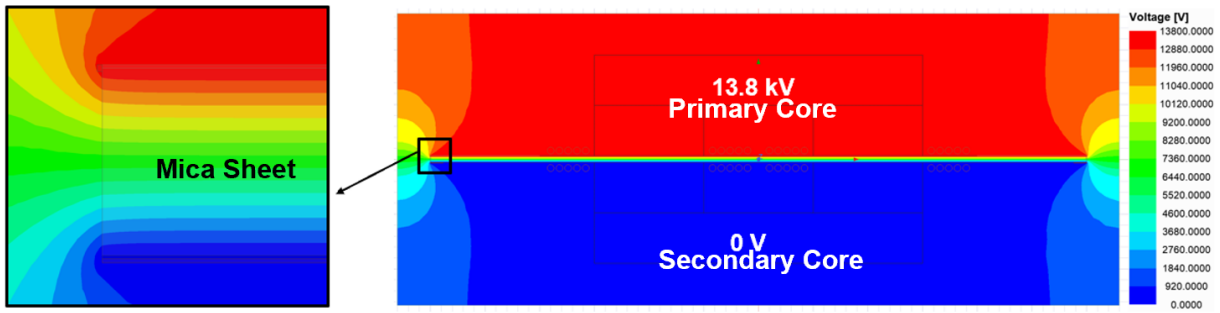


Figure 37: Voltage plot for the 2D model of the non-symmetric application of the semiconductive paint.

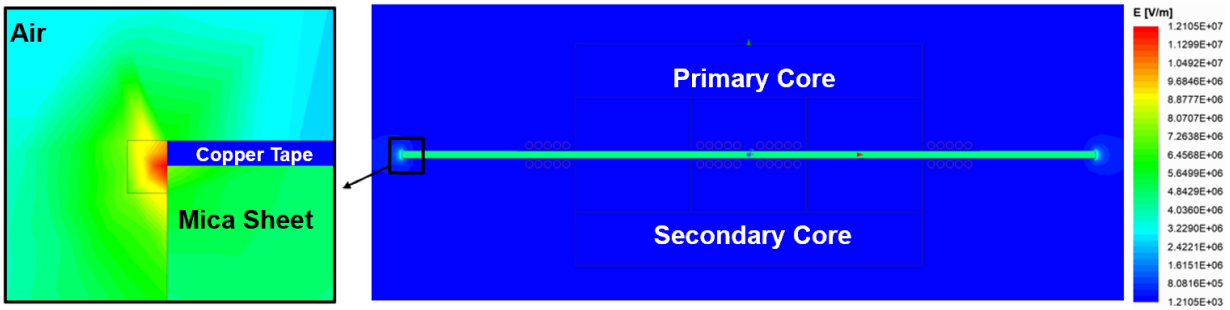


Figure 38: Electric field plot for the 2D model of the non-symmetric application of the semiconductive paint.

Overall, this layer by layer electric field study of the transformer insulation sheets indicate that (1) the conductive paint is needed to fill air gaps between the coils, core, and insulation sheet to promote a uniform voltage distribution (2) the created TPs need to be treated, otherwise field enhancements will persist (3) a linear semiconductive paint with a conductivity of approximately 2 S/m is too conductive to provide any resistive field grading, hence the field simply shifts to the termination of the semiconductive paint instead of mitigating the field. In earlier publications of this transformer sheet, one of the proposed solutions was adding a copper or highly conductive grounding frame or material which can terminate the ends of the semiconductive paint to a defined, 0 V point [45]. However, the implementation of this kind of structure is not practical for the application from an isolation standpoint as well as making such a connection at the far ends on the transformer. It was apparent that there are minimal geometric changes or adjustments which can be made to assist with field mitigation, therefore all efforts were put into identifying a material-based solution to the enhanced electric fields.

Rather than pursuing structural changes, ANSYS Maxwell 2D AC Conduction simulations were completed to identify the necessary material properties needed to mitigate the field enhancements at the TPs. It was previously concluded that the semiconductive paint used by Fastwatt is too

conductive to facilitate voltage grading across its length based on its low PDIV and the insight gained from the simulation where materials which are too conductive will not provide any field mitigation. A conductivity sweep was conducted for the semiconductive paint to determine how low the conductivity of the paint would need to be to mitigate the enhanced electric fields via resistive field grading. Figure 39 shows the sweep of the conductivity of the semiconductive paint versus the electric field at the end of said paint.

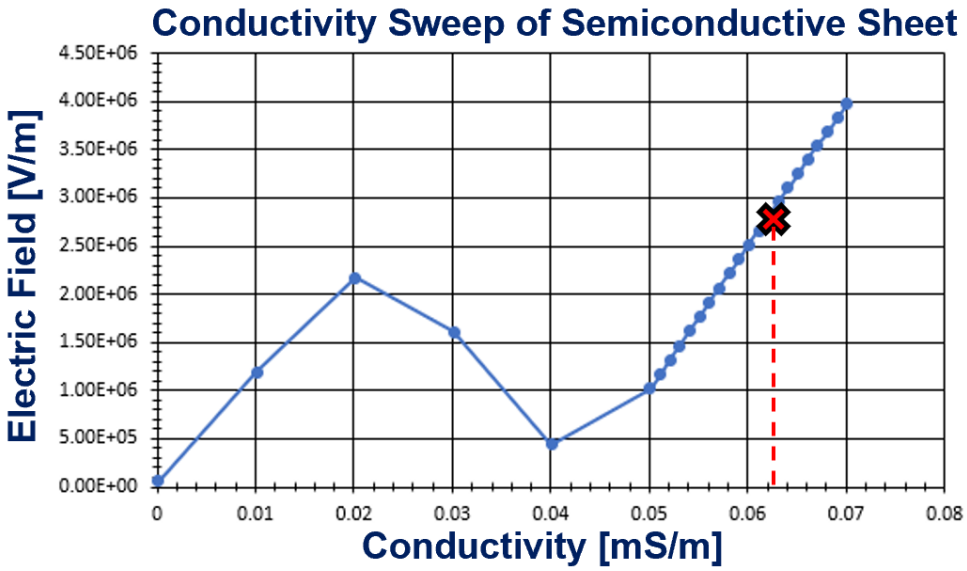


Figure 39: Conductivity sweep of semiconductive paint versus the electric field intensity.

In the conductivity range between 44 µS/m and approximately 65 µS/m, the electric field at the end of the semiconductive paint is mitigated. It is important to note that this is essentially the only viable conductivity range for significant field reduction as values lower than 44 µS/m begin to shift the field back to the termination of the conductive sheet and values higher than 65 µS/m exceed the dielectric breakdown of air. The performance of a hypothetically perfect material was simulated where Figure 40 shows the voltage plot with 44 µS/m and Figure 41 shows the electric field plot with 44 µS/m. Unlike in previous simulation voltage plots, the voltage grading across the semiconductive paint can be seen across its length. The result of this uniform and graded

voltage plot can be seen in the electric field plot where there are no longer enhanced electric fields in air. The electric field is confined to the mica sheet and still sits within a permissible range in regard to the dielectric strength of the mica sheet. For comparison purposes, the electric field at the previously enhanced TP at the termination of the semiconductive paint is now 0.16 MV/m.

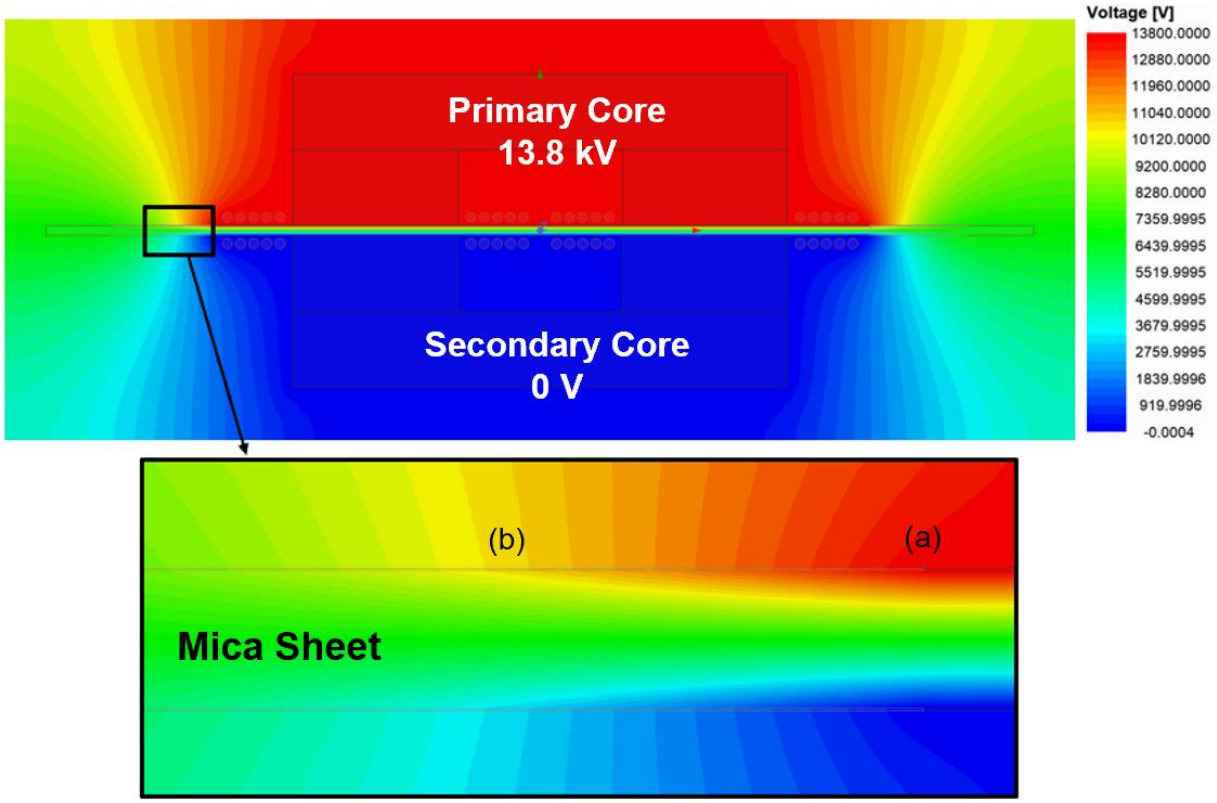


Figure 40: Voltage plot of a minimum conductivity semiconductive paint where (a) is the approximate location of the intersection of the conductive and semiconductive paint and (b) is the approximate location of the termination of the semiconductive paint.

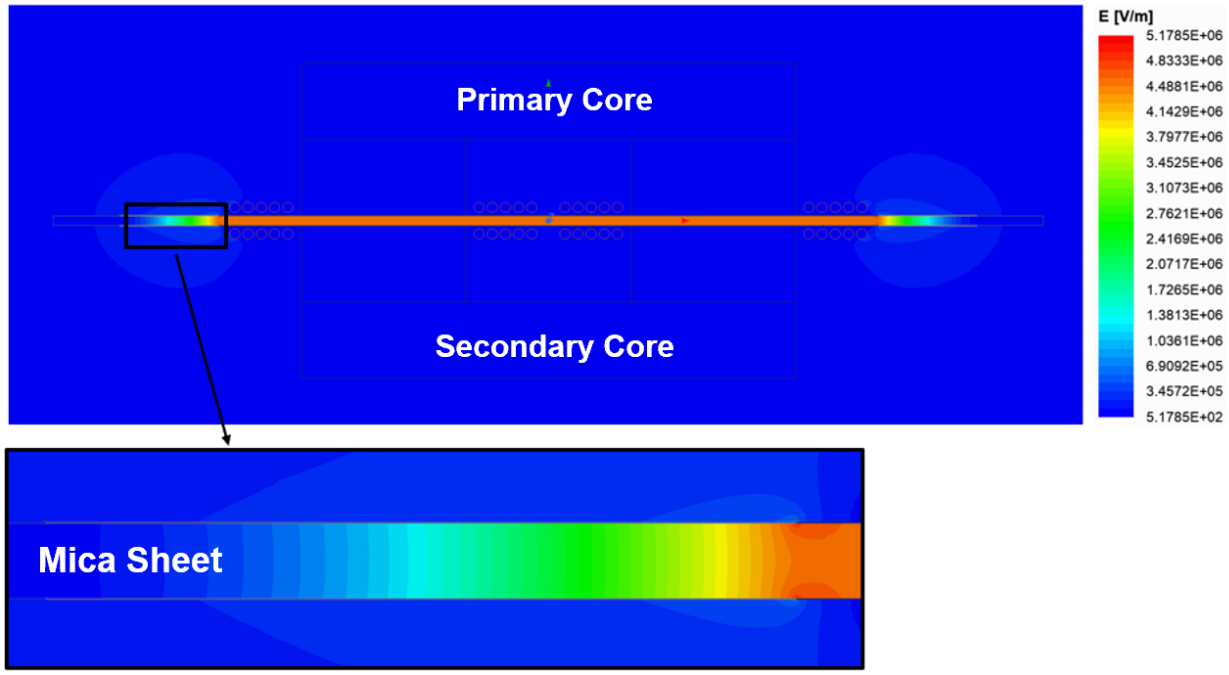


Figure 41: Electric field plot of a minimum conductivity semiconductive paint.

While an attainable insulation sheet design was simulated, the follow up challenge this work faces is identifying a material which has these ideal properties. To achieve conductivity within the identified field mitigating range, the sheet resistance of the material would need to be significantly large. Materials generally fall into four main categories from most resistive to most conductive: insulative, anti-static, static dissipative, and conductive. The mica sheet is an example of an insulative material where are the conductive, carbon paint is an example of a conductive material (specifically a shielding composite etc.). Upon surveying materials which are intended to be highly resistive, the concept of electrostatic discharge (ESD) coatings was identified [52]. ESD refers to sudden releases of static electricity build up caused by collision or interaction between objects of different changes. The consequences of ESD are similar to PD meaning if ESD is left untreated, systems at a minimum will experience individual component damage, performance decline, and at a maximum, full system failure. ESD coatings and sprays from MG Chemicals, Techspray, and

Shielding Solutions were considered for the transformer insulation sheet with Techspray's Licron Crystal ESD Safe Coating being selected for concept testing. This coating was selected because generally, most ESD coatings operate in the range of mega to giga resistivity, but the Techspray ESD coating had a simple application and curing process, was within the acceptable range, and was reasonably affordable and attainable. While looking into MG Chemicals for ESD coating, high voltage insulation varnishes with applications for transformers/transformer coils were identified. These insulation varnishes are dielectric materials which can be classified as refractive field grading [47], [49], [50]. While this method was initially not considered due to its loss producing nature, because these specific varnishes are intended for transformers and high voltage systems, there was merit in determining if refractive field grading is a technique which is viable for transformer insulation considering the initial source was referring to smaller, power electronics modules. A brief nonlinear, resistive field grading study was also conducted due to the use of nonlinear paints and tapes in the initial Fastwatt samples. As previously stated, these samples could not be exactly simulated because the bare minimum material properties needed for the simulation of these nonlinear paints and tapes is not available. However, using the design method demonstrated in [50], the effects of nonlinear resistive field grading are explored for the transformer insulation sheets. As previously demonstrated in Equation (18), the key parameter which can be used to describe a nonlinear resistive field grading material are electric field intensity (E), low-field conductivity (σ_o), switching field intensity (E_b), and the nonlinear coefficient (α). The electric field intensity is the magnitude of the electric field at a given point. The low-field conductivity is the lowest conductivity which may be applied to the material before the critical field shifts to another location. An example of this can be seen in the impact of the semiconductive sheet in Figure 36 where the critical field moved from the end of the conductive sheet to the end

of the semiconductive sheet. If the conductivity of the semiconductive sheet is set to be too low, then the critical electric field will move back to the end of the conductive sheet and no field mitigation will have occurred. The low-field conductivity must be set so that this does not occur. The switching field intensity is typically set to the average field intensity of the model and the nonlinear coefficient which is a measure of how nonlinear a material is, varies from 6 to 10. Using the techniques demonstrated in [50] each of these parameters was set based on the intended operation of the transformer and its insulation sheet. Figure 42 shows the electric field at the two critical points of the transformer insulation sheet with an ideal nonlinear resistive material used as the semiconductive material. This resulted in a peak field of 1.56 MV/m at the end of the semiconductive sheet and a 2.16 MV/m peak field at the intersection of the semiconductive and conductive sheet. It is possible that further reduction could be simulated by varying the nonlinear coefficient of the material, however, this was not done because this parameter is difficult to set and control in practice regardless. Nevertheless, the implementation of this ideal nonlinear resistive field grading showed a significant, > 90 % reduction in the peak electric field at both regions of interest. However, in an effort to explore materials which exist and have already been used, the PNC coating demonstrated in [53] was simulated. Figure 43 shows the electric field simulation results of the peak electric field experienced due to the application of the PNC coating. Nonlinear resistive materials are generally made to target a specific application, especially regarding switching field and low field conductivity. Therefore, it is expected that a coating which was made for a specific model would not be completely effective at mitigating the electric field in these transformer insulation sheets. Regardless, the PNC coating did at least show a 50% reduction in the peak electric field, which is worth noting. The adjustment or creation of a nonlinear restive field grading material is outside of the scope of this work and therefore was not further pursued.

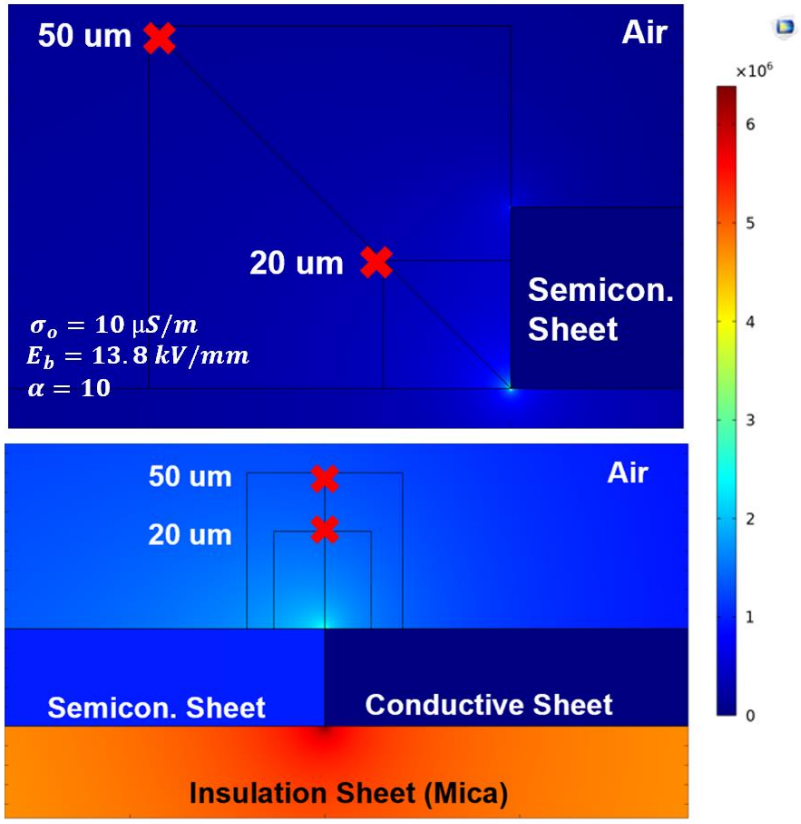


Figure 42: COMSOL simulation of the electric field (1.56 MV/m) at the end of the semiconductive sheet and at the intersection of the semiconductive and conductive sheets (2.16 MV/m).

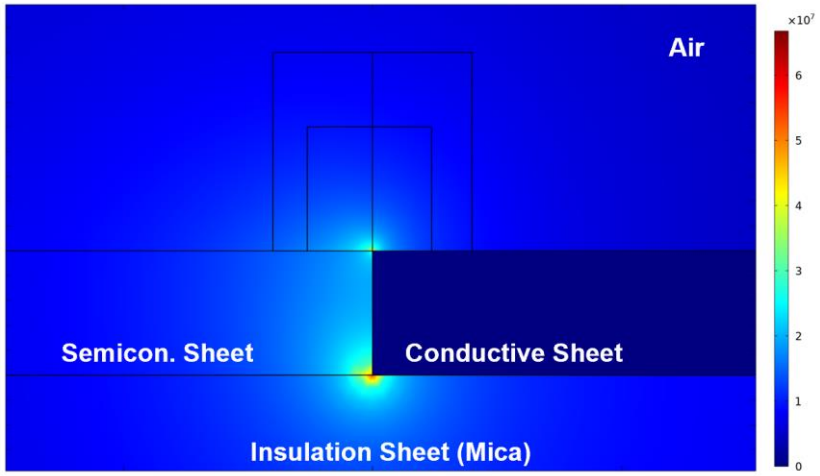


Figure 43: COMSOL simulation of the peak electric field (9.65 MV/m) across the insulating sheet when using the PNC coating [53]**as the nonlinear resistive field grading material (semiconductive sheet).**

Creation of New Sheets and PD Testing

Table VI shows a breakdown of all of the materials used to create new transformer insulation sheets along with the key, differentiating material properties between the sheets. Figure 44 shows the build process of the insulation sheets and the different combinations. Figure 44 (a) is the initial mica sheet which the paints were built upon. Figure 44 (b) features the conductive paint, applied symmetrically to both sides of the sheet. This version aims to serve as a baseline for what PDIV the rest of the samples should work to improve, similar to the simulation of only the conductive paint in the ANSYS Maxwell. Figure 44 (c) is an example of one of the two insulation varnishes applied to the perimeter of the conductive paint. Figure 44 (d) uses the static dissipative spray to coat the perimeter of the conductive sheet. A common concern regarding conductive paints in medium and high voltage applications is their ability to facilitate eddy currents and therefore eddy current losses. However, this conductive paint is significantly more resistive than other conductive materials which are common suspects for eddy currents. Despite its name and material description, it is not actually conductive enough to produce any additional losses for the insulation sheet or overall transformer.

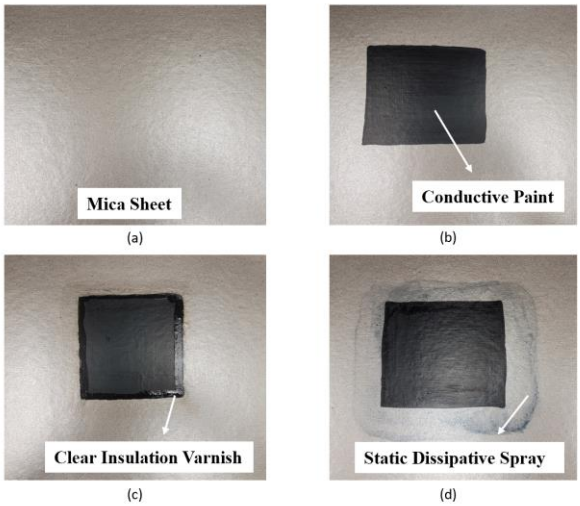


Figure 44: Transformer insulation sheets created with newly identified materials.

It is important to note that the thickness of the conductive paint only sample is greater than the thickness of the rest of the samples with conductive paint. This may result in the conductive paints across the sample having slightly different conductivities. However, the main goal of this set of sheet creations and later PD testing is to compare resistive and refractive field grading as well as to narrow down which materials should be considered and developed further for future sheet iterations.

Table VI Summary of Insulation Materials and Key Material Parameters

Material	Description
Insulation Sheet – Ax-Therm Muscovite	κ Strength: 25 kV/mm
Conductive Paint – 838AR Carbon	Surface Ω : 100 Ω /sq.
Insulation Varnish – 4226A Clear Insulating Varnish	κ Strength: 3 kV/mil, Breakdown: 5.5 kV
Static Dissipative Spray – Licron ESD Safe Coating	Surface Ω: 10^6 to 10^9 Ω
Insulation Varnish – 4226 Super Dope Corona	κ Strength: 4.1 kV/mil

The PD testing and PDIV measurement of these new sheets were completed in a similar fashion to the previously described PD testing. Table VII provides a summary of the PD testing results of the new sheets.

Some of the post-testing questions which future work will aim to address are:

- Figure 45 shows the PD plot results of the conductive paint sample. What impact did the difference in conductive paint thickness have on the PDIV between the first sample and the rest of the samples considering the conductive only paint sample is three times thicker than the rest of the samples. The thickness of the conductive paint is indirectly proportional to its sheet resistance meaning it as the thickness of the paint increases, so does its conductivity. Unexpected changes in the applied conductivity could cause subsequent differences in the expected or targeted electric field distribution.
- Figure 47 demonstrates the PD performance of the Super Dope Corona insulation varnish for refractive field grading. Figure 48 demonstrates the PD performance of the clear

insulating varnish. Why would the clear insulation varnish with a lower dielectric strength perform better than the super dope corona insulating varnish with the higher dielectric strength? What are the key differences between these materials which may explain this difference in behavior?

➢ Figure 46 shows the PD results of the ESD coating applied to the edges of the conductive sheet, demonstrating linear, resistive field grading. Figure 20(c) demonstrated the use of nonlinear, resistive field grading. Why do two of the samples, both which test different forms of field mitigation, have the same low PDIV of 3.2 kV RMS?

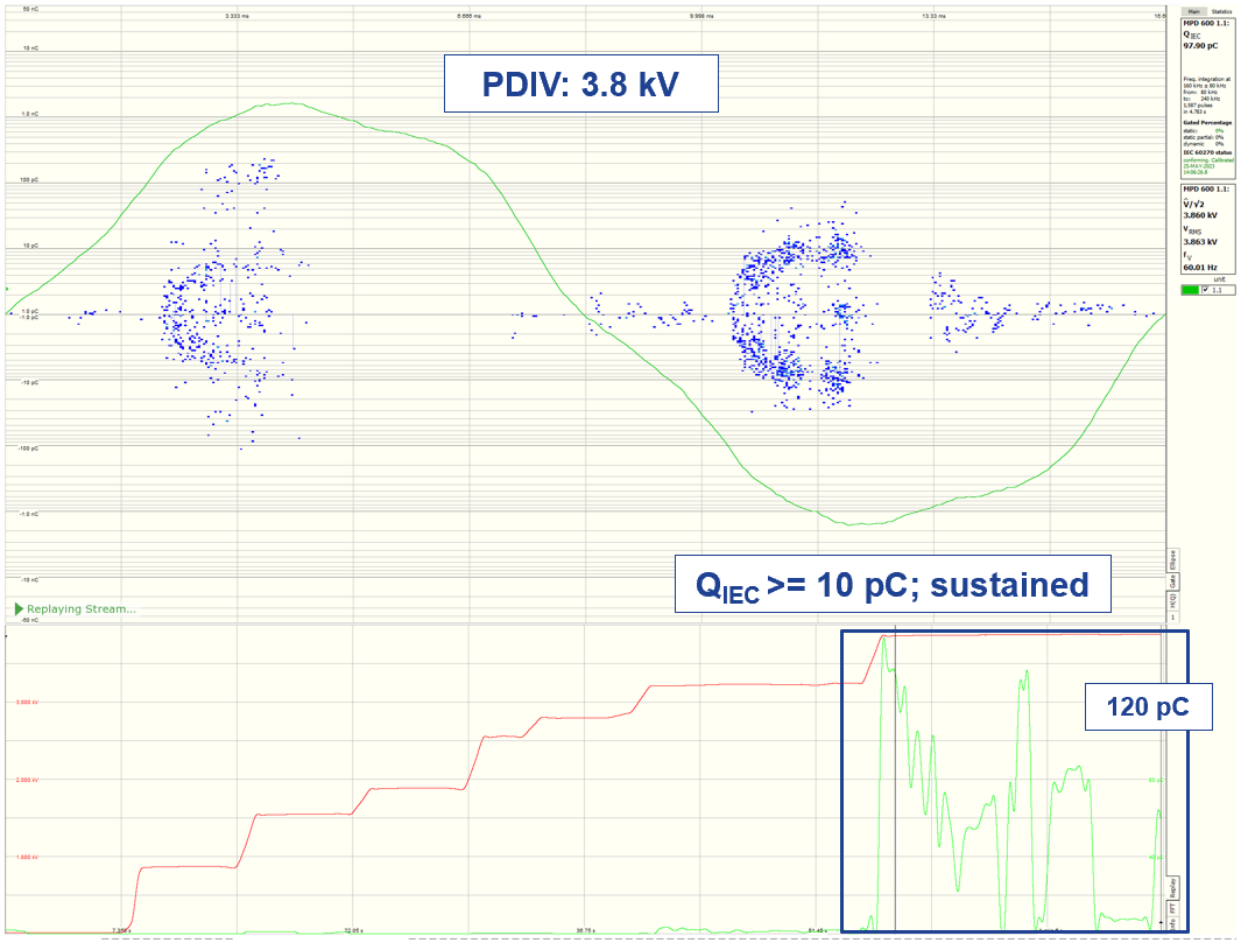


Figure 45: PD plot of the insulation sheet with only conductive paint (>= 170 S/m) at the center of the insulating mica sheet.

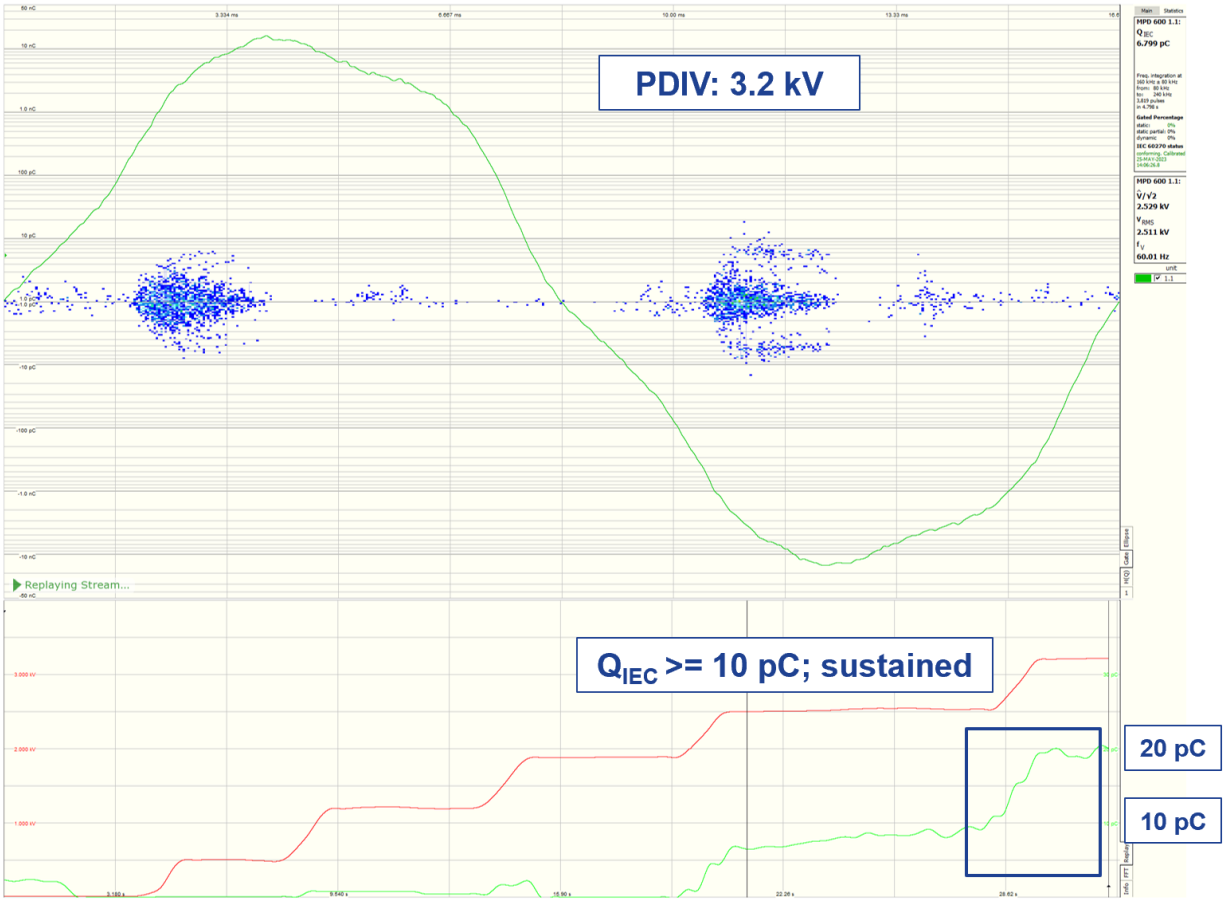


Figure 46: PD results of the sample with the conductive paint and ESD spray coating around the perimeter of the conductive coating.

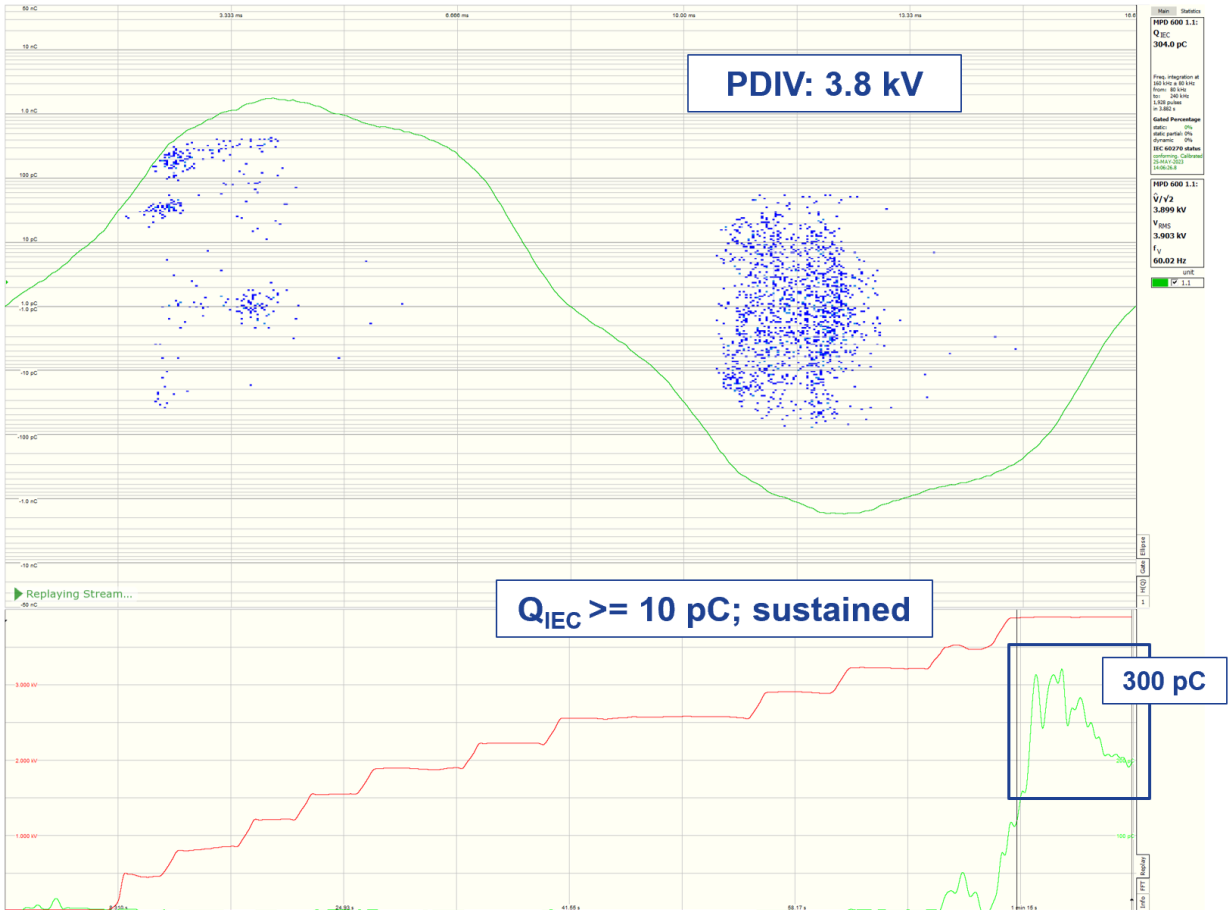


Figure 47: PD plot of insulation sheet with conductive paint and the Super Dope Corona varnish applied to its perimeter.

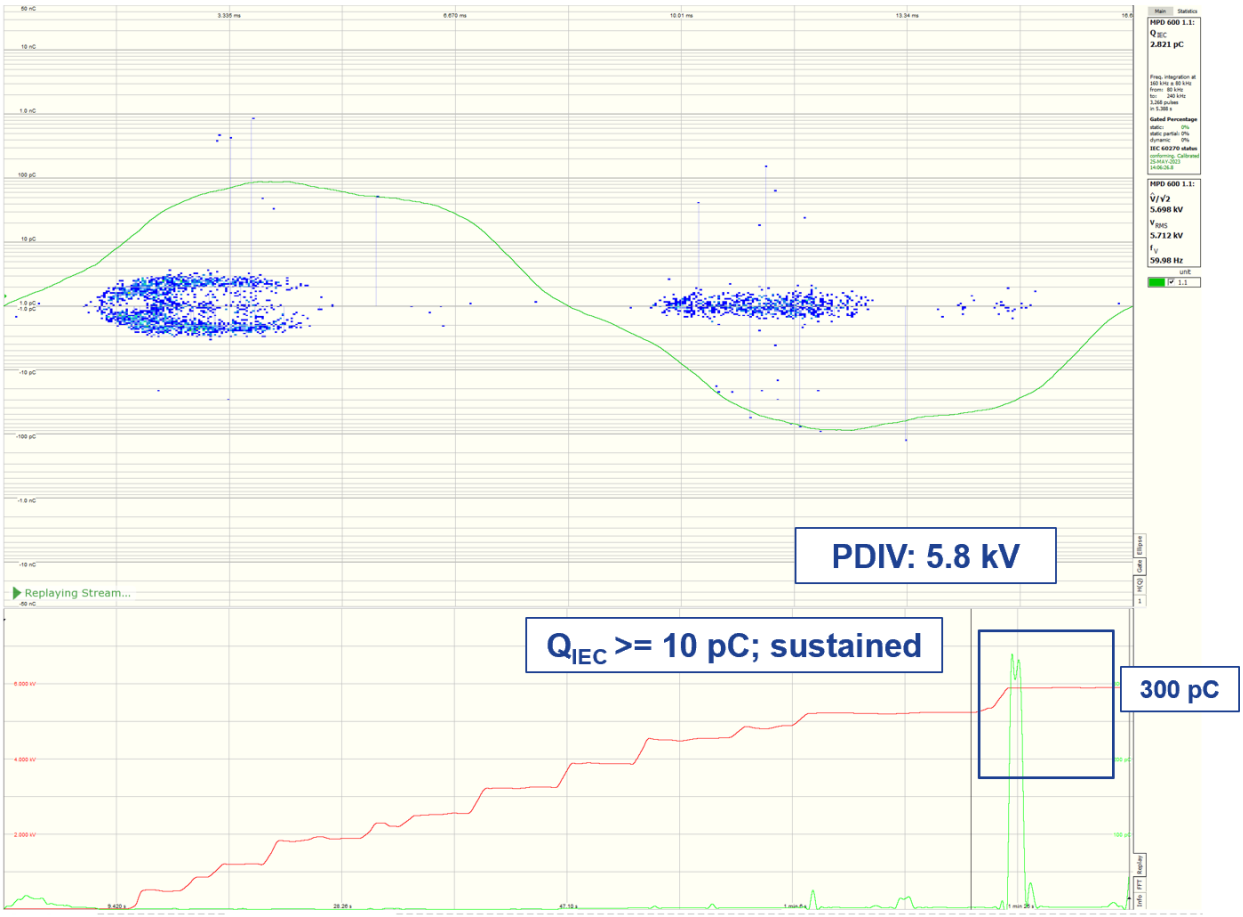


Figure 48: PD plot of the insulation sheet with the conductive paint and clear insulation varnish applied to its perimeter.

Table VII: PD Results of New Transformer Insulation Sheets

Insulation Sheet	PDIV
Conductive Paint Only	3.8 kV_{rms}
Conductive + ESD Spray	3.2 kV_{rms}
Conductive + Clear Insulation Varnish	5.5 - 5.8 kV_{rms}
Conductive + Super Dope Corona Varnish	3.8 kV_{rms}

Chapter 5: Transformer Assembly Process

To demonstrate the concept of the novel transformer design and performance which may be tested with components which are available at the time of building, the transformer was current was derated from 100 A to 50 A load overall.

Core Assembly Process

As previously described, the entire core of this transformer is a combination of 4 custom U cores where two U's are glued adjacently to increase their overall depth per transformer side (primary, secondary). To permanently secure the cores primary pair of cores and secondary pair of cores together, MASTERBOND's EP42HT-2ANLV was used. This is a two-component epoxy adhesive which, when spread thin and applied appropriately, does not hinder nor generally affect the magnetic nor thermal operation of the transformer core. This material was applied per the instructions in the technical data sheet and left to cure for over 24 hours until a secure seal was formed. Figure 49 shows the cured core pieces without the mica sheet between them.

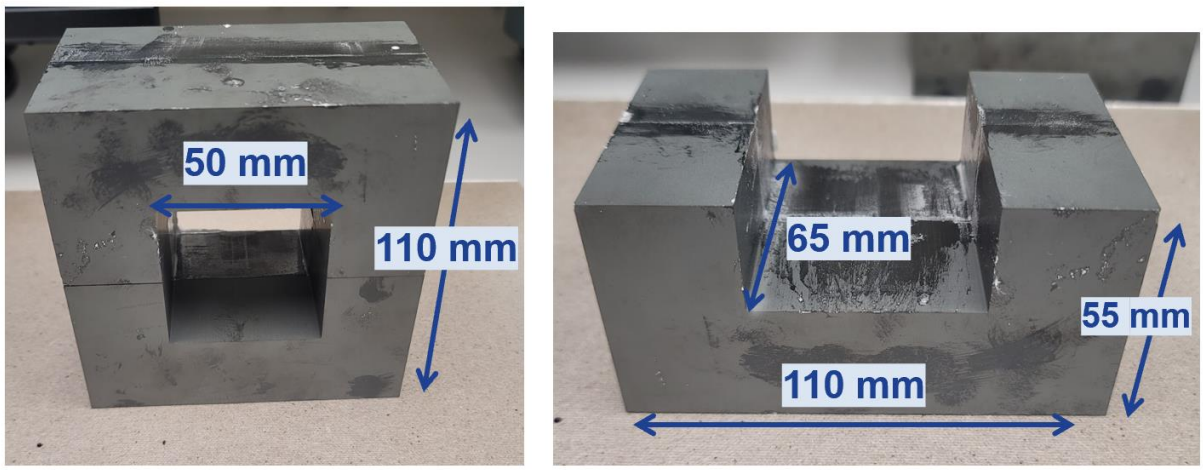


Figure 49: Transformer custom U core with area of 1950 mm^2.

Winding Assembly Process

To support the transformer windings, a bobbin was 3D printed using a PLA material with a melting point of over 100 C. Ideally in a finalized transformer assembly, ABS or similar materials with higher melting points would be used to create the winding bobbins instead. However, based on previous thermal simulations as well as considering the derated current, this PLA material should be sufficient for magnetic and insulation testing. Figure 50 shows the 3D model developed for the transformer windings and Figure 51 shows the final printed bobbin with the 25 A litz wire wound through its ridges. The terminations of the wire were created for the purpose of testing by cutting back the litz wire insulation and burning off the strand level insulation with solder. A more permanent winding assembly would use the bobbin to set the shape of the coil but secure the windings using a light spread of conductive epoxy. This will allow the bobbins to be removed but the coil shape to be maintained.

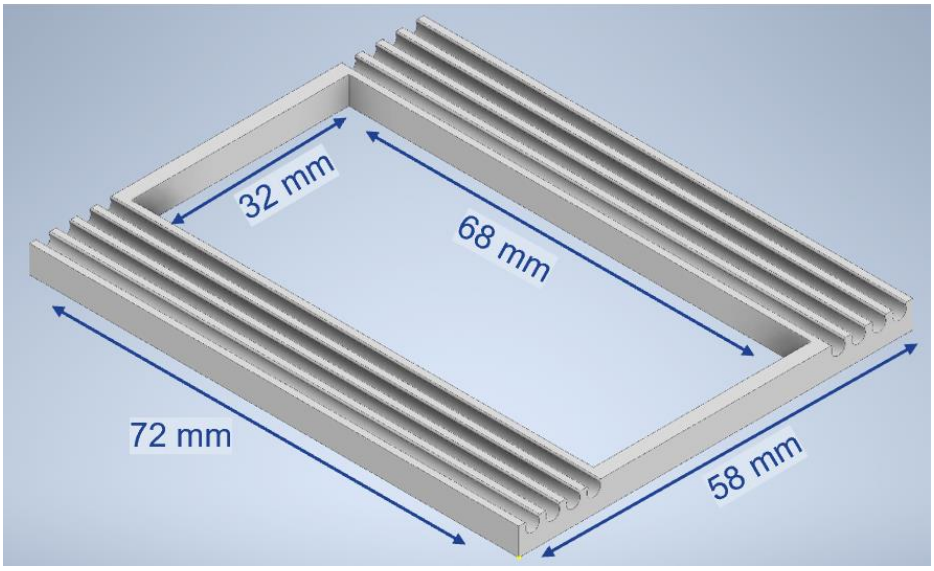


Figure 50: 3D model of bobbin for 25 A transformer coil using 44/1250 litz wire from Rubadue Wire.



Figure 51: PLA printed bobbin of model shown in Figure 50 with 44/1250 litz wire wound inside.

Transformer Build

Figure 52 shows the final assembly of the prototype. Because the purpose of this 405 kHz, 50 kW transformer is for proof of concept, it was constructed so as not be permanent. Tape is used to secure the windings with the bobbins instead of epoxy. The insulation sheet is also exchangeable so different insulation sheet configurations may be utilized. Upon assembly of the transformer, it is noticeable that there is a significant vertical gap in the transformer window. It may seem optimal to reduce this vertical gap to minimize the core volume as much as possible. However, this gap was incorporated into the design to (1) promote air cooling through the window of the transformer where, based on the magnetic flux density hot spots, there will be thermal hot spots and (2) to allow for flexible winding arrangements like stacking parallel windings of smaller wire or etc.

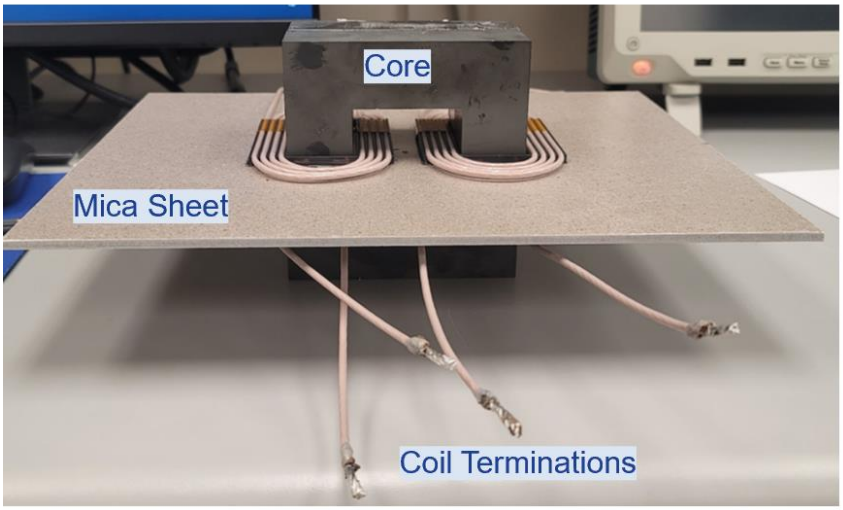


Figure 52: Fully assembled 50 kW transformer prototype featuring a custom 3F36 U core design, 3D printed bobbins with 25 A rated parallel coils and a mica insulation sheet for medium voltage isolation.

Chapter 6: Experimental Verification of Magnetic Design of Transformer

Thermal Evaluation for Testing

To perform testing on a 405 kHz, 50 kW transformer, it is important to be aware of what kind of thermal operating points might be seen in or around critical components. The transformer core has a maximum operating temperature of 110 C; however, it is common practice to avoid an overall core temperature of 100 C. Not only are core losses scaled with temperature, but also thermal runaway could cause the core to crack. As for the windings, even though the litz wire is rated for 155 C, the resistance of the copper wires will increase as temperatures which will negatively accelerate the winding losses.

ANSYS Fluent CFD simulations were conducted to answer the following questions:

- What kind of fan is needed for transformer testing?
- What kind of heat spreader is needed to ensure appropriate operating temperature for the core?

To address these concerns, first CFD simulations were completed with a recommended fan from the previous prototype. This fan had an approximate speed of 2 m/s and was 200 by 50 mm. This fan was compared to a higher power fan which has a wind speed of approximately 6 m/s and has a square configuration of 120 by 120 mm. Figure 53 (a) shows the proposed fan and Figure 53 (b) shows the previously suggested fan. A simplified, half cut of the proposed transformer prototype is used to decrease computational time by taking advantage of the symmetric structure of the transformer. The CFD simulation represents the thermal performance of the model using the user defined material assignments and those properties as well as user input loss per voltage values. Figure 54 shows the CFD simulation results of the models presented in Figure 53, respectively.

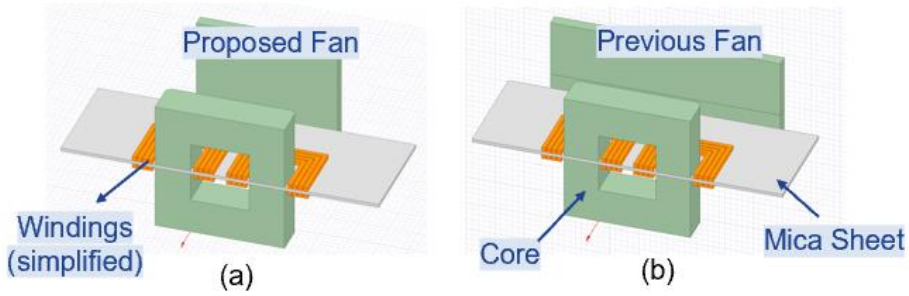


Figure 53: 3D models used for CFD simulation (a) proposed 120 x 120 mm fan (b) previously used fan.

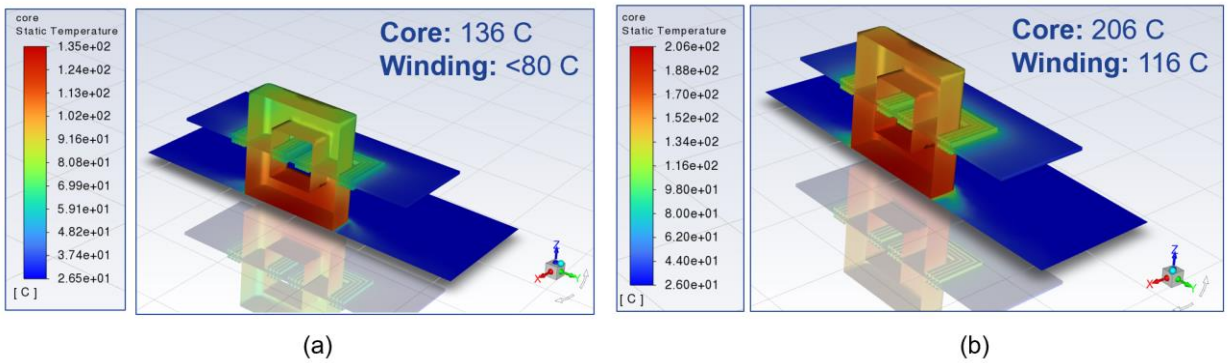


Figure 54: CFD simulation results using the models in Figure 53.

The proposed fan out performed the recommended fan by ΔT_{core} = 70 C and $\Delta T_{winding}$ = 36 C, therefore the proposed fan was purcahsed for the thermal management for transformer testing.

Despite the improved thermal performace due to air cooling, which the transformer is designed to repsond well to, the core temperature is still over 36 C higher than acceptable for safe operation. To promote better heat spreading for the transformer core, two types of heat spreaders were considered: (1) copper pin heat sink (2) liquid cold plate. The heat sink was selected based quick lead time (~2 weeks) options which had surface area of greater than or equal to the surface area of the bottom and top sides of the transformer (110 mm by 65 mm). The heat sink is an aluminum pin fin from Cool Innovations (P/N: 3-412303M). Figure 55 shows a 3D model that was generated based on the dimensions provided by the technical data sheet.

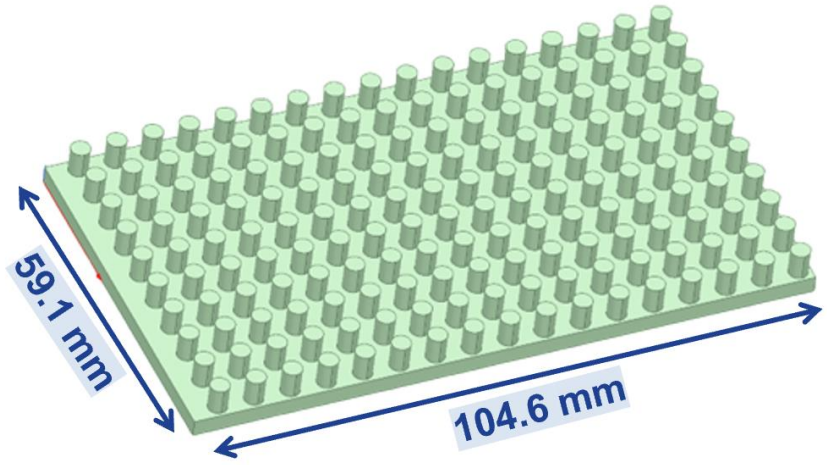


Figure 55: 3D model estimate of aluminum pin fin heatsink from Cool Innovations Advanced Heat Sinks.

To avoid adding excess weight to the overall transformer footprint, the heat sink was first explored at the table/wall facing core (secondary side) because as shown in Figure 54, there is a significant amount of heat sitting in the core piece which is interfacing with the wall boundary. Figure 56 shows the CFD simulation results from adding the proposed heat sink to the wall facing core. A thermal interfacing material (Indium) was also included in the simulation betweent heat sink and the core. The peak simulated temperature in the core is 86 C and the windings are 71 C which put both key loss producing components well below their peak temperatures.

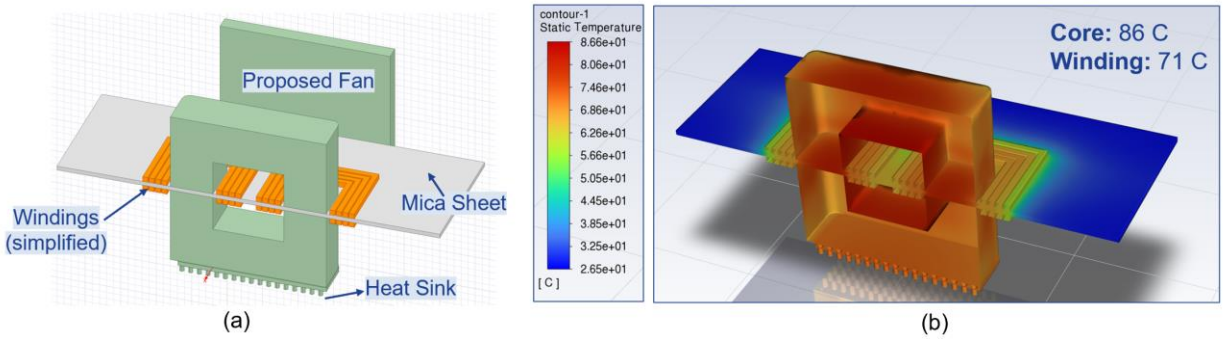


Figure 56: CFD simulation of (a) 3D model with proposed fan and identified heat sink attached with thermal interface material (indium) (b) thermal contour plot showing a peak core temperature of 86 C and peak winding temperature of 71 C.

The next heat spreader or thermal management technique that was explored was a liquid cold plate (Wakefield- Vette 12096) in place of the bottom heat sink. Figure 57 shows the thermal simulation of the transformer with liquid cooling only (no air cooling applied). A bottom core piece was used to represent the heat which would need to be dissipated by the cold plate. The peak core temperature is 97 C. While this is more than the heat sink shown in Figure 56, these results do not include forced air cooling via the selected fan. If both results are taken into consideration, the fan should be able to keep the winding temperature well-under its maximum temperature and the cold plate would be able to lead heat away from the core at the same time. If simulated, it is likely this configuration would provide the best thermal management compared to the heat sink. Furthermore, the liquid cold plate can also be used to demonstrate the transformers operational temperature in the actual iPEBB considering the bulk cooling system is rack-level liquid cooling.

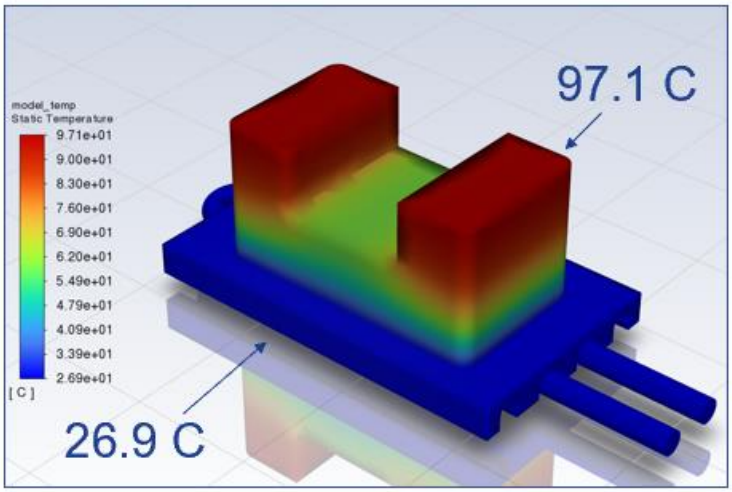


Figure 57: Liquid cooling simulation where proportional core losses are applied to the secondary core piece which mounted onto a cold plate. A peak temperature of 97.1 C is recorded at the top of the core legs.

Magnetizing Inductance and Leakage Inductance Measurements

For a CLLC-based SST, it is important to have measured values for magnetizing inductance and leakage inductance after transformer assembly. Simulated values are appropriate for the early stages of the design process, however, to know what kind of converter operation to expect, it is ideal to know what the exact inductances of the transformer are. Leakage inductance is especially important for the proper installation of the resonant capacitor(s) which will assist in achieving ZVS operation. Magnetizing inductance may be extracted during core loss testing and leakage inductance may be extracted from winding loss testing. However, before completing these tasks, especially considering the winding loss test circuit includes the resonant capacitors, inductances may be measured via an impedance analyzer. [25] describes how leakage inductance can be calculated by extracting three measurements from the transformer using an impedance analyzer based on a two-port transformer inductance model. L_{11} should be measured with the primary coils connected to the analyzer and the secondary coils open. L_{22} should be measured with the secondary coils connected to the analyzer and the primary coils open. Finally, a term, $L_{11} = M^2 / L_{22,}$ needed to calculate mutual inductance (M) can be extracted by connecting the primary side to the analyzer

and shorting the secondary side coils. Mutual inductance can be used to calculate the coupling coefficient, $k = M/\sqrt{(L_{11}L_{22})}$ [25]. Table VIII shows the measurements and calculated values based on said measurements which characterize the transformer.

Table VIII: Transformer Characterization via Impedance Analyzer

Transformer Characterization Summary	
L_{11}	7.36 uH
L_{22}	7.4 uH
$L_{11} - M^2/L_{22}$	1.35 uH
M	6.67 uH
k	0.9
L_{kp} and L_{ks}	0.71 uH and 0.714 uH
n (turns)	0.997
L_m	6.65 uH

Core Loss Testing

As previously stated, analytical calculations of core loss are typically accompanied by error producing assumptions or oversimplifications. Loss producing electromagnetic effects are typically left out of these calculations and great manipulation of the provided Steinmetz coefficients are required to achieve a meaningful result. The best way to understand core loss is to perform a variation of the open circuit test. An open circuit test in the context of transformers and core loss refers to the application of full rated voltage across the primary windings while the secondary windings are left open-circuited. Ideally, a small magnetizing current will flow through the primary windings which supports the magnetic flux in the core. Core losses are dependent on the operational magnetic flux density, switching frequency, and temperature. At this point in the transformer evaluation process, magnetizing inductance and switching frequency are set so the only parameter which affects core loss at this point is the applied voltage. Because the open circuit test calls for the full rated voltage to be applied to the primary windings, the core loss recorded indicates the baseline for core loss at normal operation. [25] provides an overview of core loss

methods proposed in research while also proposing a novel core loss measurement method. The core loss method proposed in, [54] and the two-test method proposed in [25] are considered for the validation of this transformer prototype. In [54] a half bridge is used to provide the appropriate ac excitation to the core under test (CUT). The core loss is calculated by subtracting all of the other loss producing components from the total system power loss, demonstrated in Equation (20) [54].

$$P_{core} = V * A - P_{switch} - P_{Rds(on)} - P_{c,esr} - P_{R_{ac}} \quad (20)$$

This method could be implemented for this transformer prototype with an existing full bridge converter. The $P_{Rds(on)}$ or conduction losses of the devices in the full bridge can be measured and calculated. Similarly, $P_{c,esr}$ or power dissipation due to equivalent resistance in capacitors can also be calculated using provided values from the device data sheet or independently measured. $P_{switching}$ or switching losses can be harder to calculate but losses due to switching can either be made negligible by achieving ZVS or calculated using the provided or measured $C_{oss.}$ The biggest barrier preventing accurate core loss measurement using this method for this transformer prototype is the P_{Rac} or winding loss. As previously described, during an open circuit test, the magnetic flux is generated in the core due to the flow of magnetizing current through the primary windings. The copper losses due to the current through the winding could be negligible if the magnetizing current was very small, however, in the case of this transformer and many HFTs, the magnetizing current is large enough to prevent the accurate isolation of core losses from the total converter loss. This is because the winding resistance is extremely difficult to calculate, especially considering it changes based on the operating point or conditions of the system. [25] presents the two-test method for core loss measurement to overcome the need to perform excessive calculations and additional measurements to isolate core loss. Instead, it parallels an additional inductor with the CUT to serve

as the load for the converter to achieve ZVS. The CUT's airgap is minimized to maximize its magnetizing inductance. This results in the CUT receiving a minimal amount of magnetizing current to generate magnetic flux in the core. The minimization of the magnetizing current allows for the winding losses to now be negligible. The first test is completed with the CUT and the inductor while the second test is completed without the CUT. By subtracting the losses between the two tests and compensating for converter losses due to difference in total converter current, core loss can be calculated because the CUT is the only loss producing change as shown in Equation (21)-(23).

$$P_{core} = V_{in}\left(I_{supply_1} - I_{supply_2}\right) - P_{conduction} - P_{turn-off} \tag{21}$$

$$P_{conduction} = 2\left(i_{total_1}^2 - i_{total_2}^2\right)R_{ds(on)} \tag{22}$$

$$P_{turn-off} = f_{sw}(E_{off}\left[i_{total_{1,peak}}\right] - E_{off}[i_{total_{2,peak}}] \tag{23}$$

Not only is this method of finding core loss significantly simpler compared to previous methods but it is also more reliable. Figure 58 shows the test bed for the test 1 of the two-test core loss measurement method. Figure 59 shows thermal camera images as the voltage across the primary windings was increased from 0 V to 800 V. The test bed shown in Figure 58 can only be run up to 300 kHz due to the operational limitations of the switching devices the bridges are made of. Therefore, to achieve a comparable magnetic flux density in the core to extract meaningful core losses, the voltage was proportionally reduced to 800 V. The ratio of 800 V to 300 kHz operation produces approximately the same magnetic flux magnetic flux in the core compared to the designed operational point of 1000 V to 405 kHz. At a maximum, the overall converter losses from test 2 which excludes the CUT can be subtracted from test 1 which includes the CUT. The

difference between these two tests for the maximum possible operation point (800 V, 300 kHz) is 549 meaning that the CUT's core losses are no more than 549 W. Since the two-test method is intended to mitigate the need for extensive additional loss compensation, it is assumed that most of the reported losses are due to the core. Initial calculation of additional losses due to the switching devices was estimated to be at least 50 W, leaving 500 W to the core. Considering this experimental measurement of core loss is significantly larger than the calculated value, more work must be done to properly compensate for any additional, unexpected losses which may exist in the test bed.

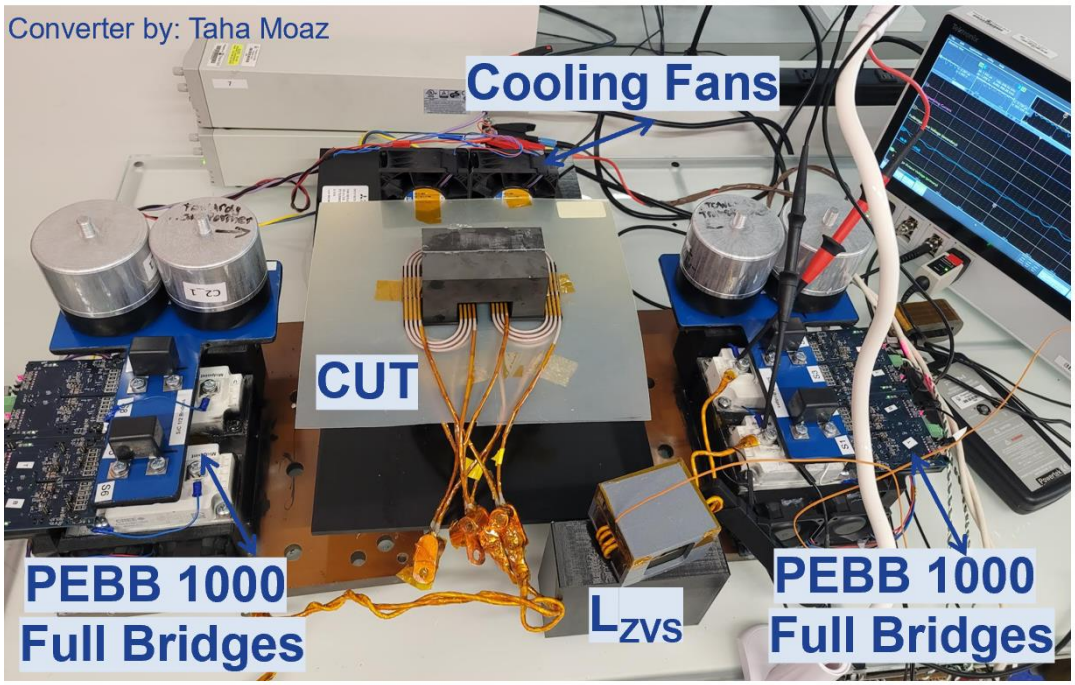


Figure 58: Testbed set up for test 1 of the two-test core loss measurement method where L_{zvs} is added in parallel with the CUT to achieve ZCS in the full bridges while the L_m of the CUT is minimized by decreasing its airgap to >>1 mm. A Rogowski coil is attached to the bridge which feeds into L_{zvs} to measure the current provided by the converter while the overall set-up losses are measured from the power supply itself.

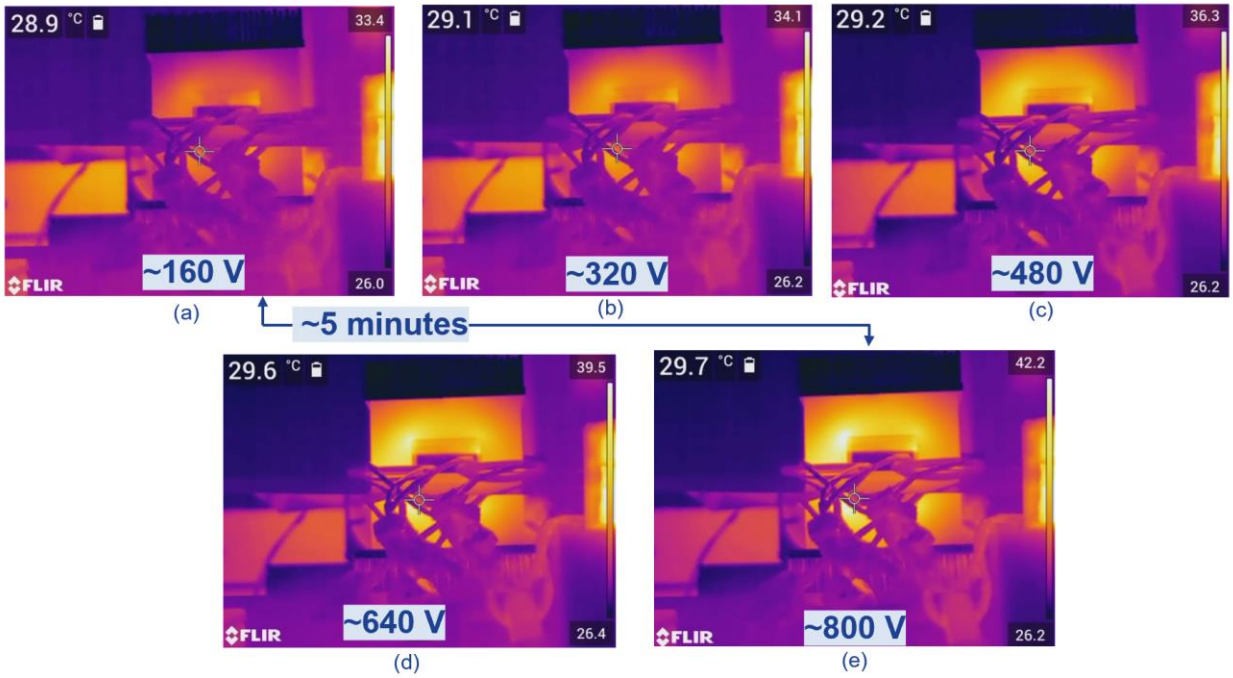


Figure 59: Thermal camera images over 5 minutes of open circuit testing with a focus on the CUT as the voltage across the primary windings was increased from 0 V to 800 V. The temperature of the core was monitored for safety purposes and not run to thermal steady state which would be needed for a comprehensive thermal performance evaluation.

Winding Loss Testing

Similar to core loss, the analytical calculation of winding loss based on extracted fields from FEA simulations possess assumptions which introduce error into the final calculation. This analytical estimation of winding loss is sufficient for additional evaluations via simulation but to gauge the efficiency of the transformer, the winding losses must be experimentally verified. The winding losses of a transformer are measured by performing a short circuit test. In a typical short circuit test, the secondary windings are short circuited, usually with the secondary side resonant capacitor for CLLC-based SSTs. The applied voltage across the primary winding is increased from 0 V until full rated current is achieved. Because of the short, the primary voltage will be >5% of the full rated voltage on average. By achieving fully rated current with such a small excitation voltage, core loss and switching losses may be ignored. Similar to core loss, non-negligible converter

component losses must be subtracted from the total converter losses to isolate the winding losses, as shown in Equation (24).

$$P_{winding} = P_{supply} - P_{R_{ds(on)}} - P_{C_{esr}} \tag{24}$$

Figure 60 shows the test bed for the short circuit test of the CUT with the resonant capacitors added. The primary current was measured using a Rogowski coil and the voltage across the windings was increased from 0 V to approximately 45 V where fully rated current was detected. The power supply detected approximately 144 W of loss and because the current through the converter was so small, 3.2 A, the compensations terms negligibly mask the winding losses. Therefore, it can be concluded that the winding losses at a maximum, 144 W.

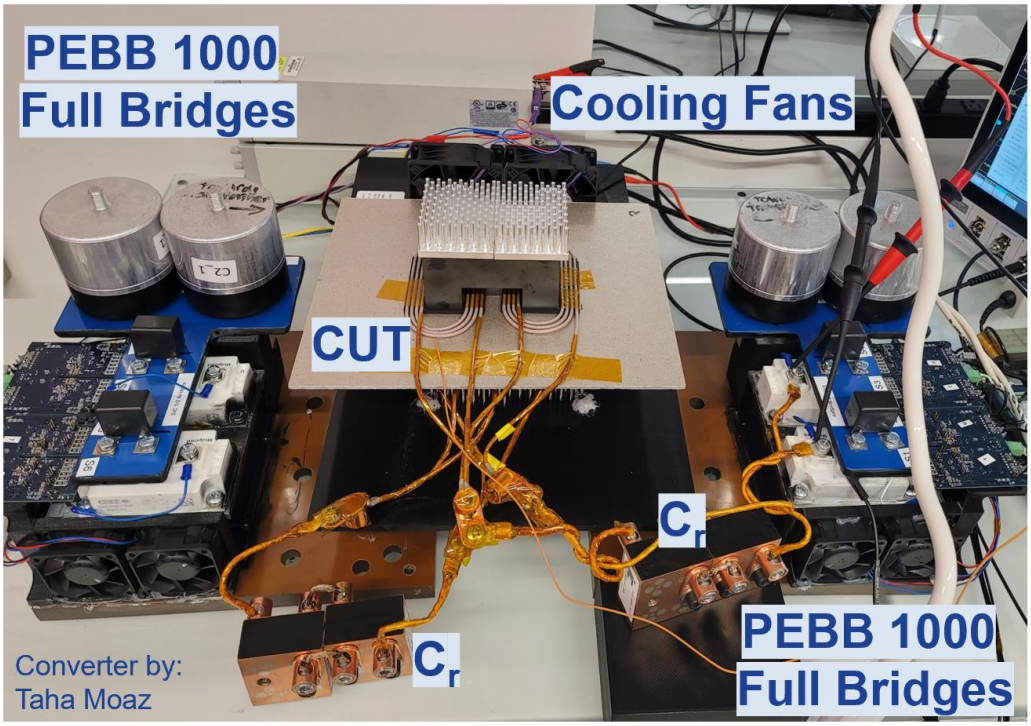


Figure 60: Test bed for short circuit test where 0.4 uF capacitor banks are added to the primary and secondary sides of the CUT. The secondary capacitor bank is used to short circuit the secondary side of the transformer.

Chapter 7: Conclusion

Design Summary

Overall, the design and analysis of a 405 kHz, 100 kW transformer was presented with a 50kW prototype built and tested for demonstration of concept and preliminary magnetic verification. Further, a survey of the behavior of the electric field in HF transformer insulation was studied and different solutions for TPs and other field enhancements were explored. Table IX provides a summary of the accomplishments of this work.

Table IX: Overview of Work

Transformer Parameter	Results
Power Rating	100 kW (designed) / 50 kW (demonstrated)
Frequency	405 kHz
Power Density	~13 kW/L
Core Loss	126 W (simulated) / < 549 W (experimental)
Winding Loss	113 W (simulated) / < 144 W (experimental)
Insulation Sheet	PDIV <= 5.8 kV_{rms}

Future Work

The immediate future work building off of this thesis would be the assembly and experimental verification of the 405 kHz, 100 kW transformer. Some further work which would benefit that initiative is the exploration of different winding structures and bobbins which can better support the large, high current rating litz wires, detailed thermal simulation and testing with a more accurate transformer model (winding arrangement, materials), and general development of the insulation system. Specifically, further PD testing is needed to verify the performance of the

introduced materials and the manufacturing process of the sheets needs to be standardized so application between samples is consistent and comparable. Additionally, when a finalized sheet design is identified, the PD testing should be repeated as more components of the final transformer are added (bobbin, coils, core) to gain a meaningful understanding of the final transformer's insulation performance. The completion of these tasks are necessary to build towards the intended goal of a PDIV of at least 10 kV.

References

[1] R. Burgess, M. Greenstone, N. Ryan, and A. Sudarshan, “Demand for electricity on the global electrification frontier,” 2023.

[2] US Congressional Budget Office, “Emissions of Carbon Dioxide in the Transportation Sector At a Glance,” 2022. [Online]. Available: www.cbo.gov/publication/58566

[3] M. Yuan, J. Z. Thellufsen, H. Lund, and Y. Liang, “The electrification of transportation in energy transition,” *Energy*, vol. 236, p. 121564, Dec. 2021, doi: 10.1016/J.ENERGY.2021.121564.

[4] F. Blaabjerg, K. Ma, and Y. Yang, “Power Electronics for Renewable Energy Systems - Status and Trends,” in *CIPS 2014; 8th International Conference on Integrated Power Electronics Systems*, 2014, pp. 1–11.

[5] H. Shadfar, M. Ghorbani Pashakolaei, and A. Akbari Foroud, “Solid-state transformers: An overview of the concept, topology, and its applications in the smart grid,” *International Transactions on Electrical Energy Systems*, vol. 31, no. 9, Sep. 2021, doi: 10.1002/2050-7038.12996.

[6] Xu She, A. Q. Huang, and R. Burgos, “Review of Solid-State Transformer Technologies and Their Application in Power Distribution Systems,” *IEEE J Emerg Sel Top Power Electron*, vol. 1, no. 3, pp. 186–198, Sep. 2013, doi: 10.1109/JESTPE.2013.2277917.

[7] T. Ericsen, N. Hingorani, and Y. Khersonsky, “PEBB - Power Electronics Building Blocks from Concept to Reality,” in *2006 Record of Conference Papers - IEEE Industry Applications Society 53rd Annual Petroleum and Chemical Industry Conference*, IEEE, Sep. 2006, pp. 1–7. doi: 10.1109/PCICON.2006.359706.

[8] N. Rajagopal, R. Raju, T. Moaz, and C. DiMarino, “Design of a High-Frequency Transformer and 1.7 kV Switching-Cells for an Integrated Power Electronics Building Block (iPEBB),” in *2021 IEEE Electric Ship Technologies Symposium (ESTS)*, IEEE, Aug. 2021, pp. 1–8. doi: 10.1109/ESTS49166.2021.9512358.

[9] D. Dong, M. Agamy, J. Z. Bebic, Q. Chen, and G. Mandrusiak, “A Modular SiC High-Frequency Solid-State Transformer for Medium-Voltage Applications: Design, Implementation, and Testing,” *IEEE J Emerg Sel Top Power Electron*, vol. 7, no. 2, pp. 768–778, Jun. 2019, doi: 10.1109/JESTPE.2019.2896046.

[10] N. Rajagopal, “Design of 1.7 kV SiC MOSFET Switching-Cells for Integrated Power Electronics Building Block (iPEBB),” Virginia Polytechnic Institute and State University, Arlington, 2021.

[11] J. Wang *et al.*, “Power electronics building block (PEBB) design based on 1.7 kV SiC MOSFET modules,” *2017 IEEE Electric Ship Technologies Symposium, ESTS 2017*, pp. 612–619, 2017, doi: 10.1109/ESTS.2017.8069345.

[12] Z. Guo *et al.*, “A Novel High Insulation 100 kW Medium Frequency Transformer,” *IEEE Trans Power Electron*, vol. 38, no. 1, pp. 112–117, Jan. 2023, doi: 10.1109/TPEL.2022.3205646.

[13] C. Zhao, Y.-H. Hsieh, F. C. Lee, and Q. Li, “Design and Analysis of a High-frequency CLLC Resonant Converter with Medium Voltage insulation for Solid-State-Transformer,” in *2021 IEEE Applied Power Electronics Conference and Exposition (APEC)*, IEEE, Jun. 2021, pp. 1638–1642. doi: 10.1109/APEC42165.2021.9487101.

[14] S. Zhao, Q. Li, F. C. Lee, and B. Li, "High-Frequency Transformer Design for Modular Power Conversion From Medium-Voltage AC to 400 VDC," *IEEE Trans Power Electron*, vol. 33, no. 9, pp. 7545–7557, Sep. 2018, doi: 10.1109/TPEL.2017.2774440.
[15] M. Ngo, Y. Cao, D. Dong, and R. Burgos, "Design of 500 kHz, 18 kW Low Leakage Inductance Intraleaved Litz Wire Transformer for Bi-directional Resonant DC-DC Converter," in *2021 IEEE Applied Power Electronics Conference and Exposition (APEC)*, IEEE, Jun. 2021, pp. 1153–1161. doi: 10.1109/APEC42165.2021.9487443.
[16] S.-Y. Yu, R. Chen, and A. Viswanathan, "Survey of Resonant Converter Topologies ," *Texas Instruments Power Supply Design Seminar*. Texas Instruments, 2018.
[17] J.-H. Jung, H.-S. Kim, M.-H. Ryu, and J.-W. Baek, "Design Methodology of Bidirectional CLLC Resonant Converter for High-Frequency Isolation of DC Distribution Systems," *IEEE Trans Power Electron*, vol. 28, no. 4, pp. 1741–1755, Apr. 2013, doi: 10.1109/TPEL.2012.2213346.
[18] Y. Cao, M. Ngo, R. Burgos, A. Ismail, and D. Dong, "Switching Transition Analysis and Optimization for Bidirectional *CLLC* Resonant DC Transformer," *IEEE Trans Power Electron*, vol. 37, no. 4, pp. 3786–3800, Apr. 2022, doi: 10.1109/TPEL.2021.3125265.
[19] M. Kazimierczuk, *High-Frequency Magnetic Components*. Wiley, 2013. doi: 10.1002/9781118717806.
[20] H. Li and Z. Jiang, "On Automatic Resonant Frequency Tracking in LLC Series Resonant Converter Based on Zero-Current Duration Time of Secondary Diode," *IEEE Trans Power Electron*, pp. 1–1, 2015, doi: 10.1109/TPEL.2015.2462086.
[21] W. G. Hurley and W. H. Wölfle, *Transformers and Inductors for Power Electronics*. Chichester, UK: John Wiley & Sons, Ltd, 2013. doi: 10.1002/9781118544648.
[22] Proterial, "Mn-Zn Soft Ferrite Cores for High Frequency Power Supplies MaDC-F." 2019.
[23] J. Vráždil, "Magnetic Design Tool," 2023.
[24] Ferroxcube, "Power Conversion Materials."
[25] M. T. H. Ngo, "Magnetic and Thermal Design for Litz-wire 500 kHz High-power Planar Transformers with Converging Cooling Duct for 'dc Transformer' Resonant Converter Applications," Virginia Polytechnic Institute and State University, Blacksburg, VA, 2021.
[26] Chas. P. Steinmetz, "On the Law of Hysteresis," *Transactions of the American Institute of Electrical Engineers*, vol. IX, no. 1, pp. 1–64, Jan. 1892, doi: 10.1109/T-AIEE.1892.5570437.
[27] M. Mu, "High Frequency Magnetic Core Loss Study," Virginia Polytechnic Institute and State University, Blacksburg, 2013.
[28] Roderick Javier Garcia Montoya, "High-Frequency Transformer Design for Solid-State Transformers in Electric Power Distribution Systems," University of Arkansas, Fayetteville, 2015.
[29] J. Reinert, A. Brockmeyer, and R. W. A. A. De Doncker, "Calculation of losses in ferro- and ferrimagnetic materials based on the modified Steinmetz equation," *IEEE Trans Ind Appl*, vol. 37, no. 4, pp. 1055–1061, 2001, doi: 10.1109/28.936396.
[30] K. Venkatachalam, C. R. Sullivan, T. Abdallah, and H. Tacca, "Accurate prediction of ferrite core loss with nonsinusoidal waveforms using only Steinmetz parameters," in *2002 IEEE Workshop on Computers in Power Electronics, 2002. Proceedings.*, IEEE, pp. 36–41. doi: 10.1109/CIPE.2002.1196712.
[31] Jieli Li, T. Abdallah, and C. R. Sullivan, "Improved calculation of core loss with nonsinusoidal waveforms," in *Conference Record of the 2001 IEEE Industry Applications*

Conference. 36th IAS Annual Meeting (Cat. No.01CH37248), IEEE, pp. 2203–2210. doi: 10.1109/IAS.2001.955931.
[32] D.-T. Quach *et al.*, "Minor hysteresis patterns with a rounded/sharpened reversing behavior in ferromagnetic multilayer," *Sci Rep*, vol. 8, no. 1, p. 4461, Mar. 2018, doi: 10.1038/s41598-018-22810-y.
[33] Y. Cao *et al.*, "Hysteresis in single and polycrystalline iron thin films: Major and minor loops, first order reversal curves, and Preisach modeling," *J Magn Magn Mater*, vol. 395, pp. 361–375, Dec. 2015, doi: 10.1016/j.jmmm.2015.06.072.
[34] Y. Cao, K. Ngo, and D. Dong, "A Scalable Electronic-Embedded Transformer (EET), a New Concept toward Ultra-high-frequency High-power Transformer in DC-DC Converters," *IEEE Trans Power Electron*, pp. 1–15, 2023, doi: 10.1109/TPEL.2023.3279259.
[35] New England Wire Technologies, "Why preformed litz wire is your best choice for high current (kHz range) magnetic devices."
[36] PowerStream, "Wire Gauge and Current Limits Including Skin Depth and Tensile Strength," Apr. 18, 2023.
[37] C. R. Sullivan, "Computationally efficient winding loss calculation with multiple windings, arbitrary waveforms, and two-dimensional or three-dimensional field geometry," *IEEE Trans Power Electron*, vol. 16, no. 1, pp. 142–150, Jan. 2001, doi: 10.1109/63.903999.
[38] The Gund Company, "Transformer Applications."
[39] T. Dragicevic, P. Wheeler, and F. Blaabjerg, Eds., *DC Distribution Systems and Microgrids*. Institution of Engineering and Technology, 2018. doi: 10.1049/PBPO115E.
[40] IEEE Standards Association, "IEEE Standard for General Requirements for Dry-Type Distribution and Power Transformers," Nov. 24, 2020.
[41] Z. Li, Y.-H. Hsieh, Q. Li, F. C. Lee, and C. Zhao, "Insulation Design on High-Frequency Transformer for Solid-State Transformer," in *2021 IEEE Energy Conversion Congress and Exposition (ECCE)*, IEEE, Oct. 2021, pp. 1149–1155. doi: 10.1109/ECCE47101.2021.9595657.
[42] C. F. Bayer, E. Baer, U. Waltrich, D. Malipaard, and A. Schletz, "Simulation of the electric field strength in the vicinity of metallization edges on dielectric substrates," *IEEE Transactions on Dielectrics and Electrical Insulation*, vol. 22, no. 1, pp. 257–265, Feb. 2015, doi: 10.1109/TDEI.2014.004285.
[43] D. Tommasini, "Dielectric insulation and high-voltage issues," in *CAS 2009 - CERN Accelerator School: Magnets, Proceedings*, 2010.
[44] Q. Chen, R. Raju, D. Dong, and M. Agamy, "High Frequency Transformer Insulation in Medium Voltage SiC enabled Air-cooled Solid-State Transformers," in *2018 IEEE Energy Conversion Congress and Exposition (ECCE)*, IEEE, Sep. 2018, pp. 2436–2443. doi: 10.1109/ECCE.2018.8557849.
[45] S. Sharfeldden, R. Raju, and C. DiMarino, "Insulation Design for a Compact, Medium-Voltage Transformer," in *2022 IEEE Energy Conversion Congress and Exposition (ECCE)*, IEEE, Oct. 2022, pp. 1–6. doi: 10.1109/ECCE50734.2022.9947979.
[46] R. Arora and W. Mosch, *High Voltage and Electrical Insulation Engineering*. Wiley, 2011. doi: 10.1002/9780470947906.

[47] T. Christen, L. Donzel, and F. Greuter, “Nonlinear resistive electric field grading part 1: Theory and simulation,” *IEEE Electrical Insulation Magazine*, vol. 26, no. 6, 2010, doi: 10.1109/MEI.2010.5599979.
[48] K. Hindelang and J. Lambrecht, “Grading of Electric Field with Silicone Based Materials,” in *Conference on Silicone Insulation*, 2022.
[49] A. Can-Ortiz, L. Laudebat, Z. Valdez-Nava, and S. Diaham, “Nonlinear Electrical Conduction in Polymer Composites for Field Grading in High-Voltage Applications: A Review,” *Polymers (Basel)*, vol. 13, no. 9, p. 1370, Apr. 2021, doi: 10.3390/polym13091370.
[50] J. Xu, Z. Zhang, K. D. T. Ngo, and G.-Q. Lu, “Desired Properties of a Nonlinear Resistive Coating for Shielding Triple Point in a Medium-Voltage Power Module,” *IEEE Transactions on Dielectrics and Electrical Insulation*, vol. 28, no. 5, pp. 1721–1728, Oct. 2021, doi: 10.1109/TDEI.2021.009507.
[51] J. Krupka, “Contactless methods of conductivity and sheet resistance measurement for semiconductors, conductors and superconductors,” *Meas Sci Technol*, vol. 24, no. 6, p. 062001, Jun. 2013, doi: 10.1088/0957-0233/24/6/062001.
[52] Production Automation Corporation PAC, “What is the Difference Between Anti-Static, Dissipative, Conductive, and Insulative?”
[53] Z. Zhang *et al.*, “Packaging of a 15-kV Silicon Carbide MOSFET With Insulation Enhanced by a Nonlinear Resistive Polymer-Nanoparticle Coating,” in *2022 IEEE Energy Conversion Congress and Exposition (ECCE)*, IEEE, Oct. 2022, pp. 1–4. doi: 10.1109/ECCE50734.2022.9947881.
[54] B. Carsten, “Why the magnetics designer should measure core loss; with a survey of loss measurement techniques and a low cost high accuracy alternative,” in *IEEE International Conference on Power Conversion*, 1995, pp. 163–180.